

**AFRL-IF-RS-TR-2002-319**  
**Final Technical Report**  
**January 2003**



# **PROTOTYPE PROTEIN-BASED THREE- DIMENSIONAL MEMORY**

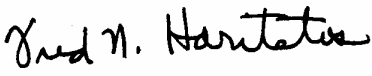
**Syracuse University**

*APPROVED FOR PUBLIC RELEASE; DISTRIBUTION UNLIMITED.*

**AIR FORCE RESEARCH LABORATORY  
INFORMATION DIRECTORATE  
ROME RESEARCH SITE  
ROME, NEW YORK**

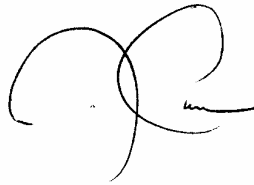
This report has been reviewed by the Air Force Research Laboratory, Information Directorate, Public Affairs Office (IFOIPA) and is releasable to the National Technical Information Service (NTIS). At NTIS it will be releasable to the general public, including foreign nations.

AFRL-IF-RS-TR-2002-319 has been reviewed and is approved for publication.

APPROVED: 

FRED N. HARITATOS  
Project Engineer

FOR THE DIRECTOR:



JOSEPH CAMERA, Chief  
Information & Intelligence Exploitation Division  
Information Directorate

<b>REPORT DOCUMENTATION PAGE</b>			<i>Form Approved</i> <b>OMB No. 074-0188</b>	
Public reporting burden for this collection of information is estimated to average 1 hour per response, including the time for reviewing instructions, searching existing data sources, gathering and maintaining the data needed, and completing and reviewing this collection of information. Send comments regarding this burden estimate or any other aspect of this collection of information, including suggestions for reducing this burden to Washington Headquarters Services, Directorate for Information Operations and Reports, 1215 Jefferson Davis Highway, Suite 1204, Arlington, VA 22202-4302, and to the Office of Management and Budget, Paperwork Reduction Project (0704-0188), Washington, DC 20503				
<b>1. AGENCY USE ONLY (Leave blank)</b>		<b>2. REPORT DATE</b> JANUARY 2003	<b>3. REPORT TYPE AND DATES COVERED</b> Final Sep 99 – Oct 01	
<b>4. TITLE AND SUBTITLE</b> PROTOTYPE PROTEIN-BASED THREE-DIMENSIONAL MEMORY			<b>5. FUNDING NUMBERS</b> C - F30602-99-1-0555 PE - 62702F PR - PMEM TA - 00 WU - 02	
<b>6. AUTHOR(S)</b> Robert Birge & Jeffrey Stuart				
<b>7. PERFORMING ORGANIZATION NAME(S) AND ADDRESS(ES)</b> Syracuse University Department of Chemistry W.M. Keck Center for Molecular Electronics Syracuse New York 13244-4100			<b>8. PERFORMING ORGANIZATION REPORT NUMBER</b>	
<b>9. SPONSORING / MONITORING AGENCY NAME(S) AND ADDRESS(ES)</b> Air Force Research Laboratory/IFEB 32 Brooks Road Rome New York 13441-4114			<b>10. SPONSORING / MONITORING AGENCY REPORT NUMBER</b>  AFRL-IF-RS-TR-2002-319	
<b>11. SUPPLEMENTARY NOTES</b>  AFRL Project Engineer: Fred N. Haritatos/IFEB/(315) 330-1638/ Fred.Haritatos@rl.af.mil				
<b>12a. DISTRIBUTION / AVAILABILITY STATEMENT</b> APPROVED FOR PUBLIC RELEASE; DISTRIBUTION UNLIMITED.				<b>12b. DISTRIBUTION CODE</b>
<b>13. ABSTRACT (Maximum 200 Words)</b> Under this effort, a bacteriorhodopsin-based, three dimensional (3-D) memory device was developed and fabricated. Advances were made in both prototype development and materials enhancement. Bacteriorhodopsin in its native form (i.e., the wild-type protein that has not been altered either genetically or chemically) is incapable of the efficient operation. This fact guided the research effort toward three major objectives: (1) Optimization of the protein with respect to operation in the 3-D optical memory, (2) Optimization of the polymer matrix that encapsulates the protein, thereby comprising the memory media, and (3) Fabrication of prototype 3-D optical memories geared toward use with not only the native protein, but also chemically and genetically manipulated forms. Directed evolution (DE) was selected as the best way to optimize the protein. This genetic engineering technique offers the opportunity to explore mutations that otherwise would be overlooked by more pragmatic approaches. Additionally, advances in polymer matrix optimization have been made with respect to long-term stability, shrinkage, and optical clarity. Lastly, a prototype device was made under this effort that represents the first true step toward a commercially viable optical memory.				
<b>14. SUBJECT TERMS</b> Three-Dimensional Optical Memory, Protein Memory, Branched Photocycle, Bacteriorhodopsin, Volumetric Memory, Prototypes, Hydroglass, Hydrogel			<b>15. NUMBER OF PAGES</b> 124	
			<b>16. PRICE CODE</b>	
<b>17. SECURITY CLASSIFICATION OF REPORT</b>  UNCLASSIFIED	<b>18. SECURITY CLASSIFICATION OF THIS PAGE</b>  UNCLASSIFIED	<b>19. SECURITY CLASSIFICATION OF ABSTRACT</b>  UNCLASSIFIED	<b>20. LIMITATION OF ABSTRACT</b>  UL	

## Table of Contents

<b>1.0. ABSTRACT .....</b>	<b>1</b>
<b>2.0 INTRODUCTION .....</b>	<b>2</b>
2.1. OVERVIEW OF BACTERIORHODOPSIN-BASED VOLUMETRIC OPTICAL MEMORY .....	4
<b>3.0. PROGRESS DETAILED BY TASK .....</b>	<b>9</b>
3.1. MATERIALS.....	9
3.1.1. <i>Optimization of the Protein</i> .....	9
3.1.1.1. Site-directed mutagenesis.....	12
3.1.1.2. Screening versus selection.....	13
3.1.1.3. Random mutagenesis.....	13
3.1.1.4. Semi-random mutagenesis .....	13
3.1.1.5. Directed evolution.....	15
3.1.1.6. Mutational Strategies.....	16
3.1.1.7. Summary .....	17
3.1.1.8. Goals for Application of Directed Evolution to Bacteriorhodopsin .....	17
3.1.1.9. Characterization of the Q-state in Wild Type Bacteriorhodopsin.....	18
3.1.1.9.1. Abstract.....	19
3.1.1.9.2. Introduction.....	20
3.1.1.9.3. Materials and Methods.....	22
3.1.1.9.4. Results and Discussion.....	24
3.1.1.9.4.1. Hydration Experiments in Glycerol .....	24
3.1.1.9.4.2. Regeneration of the P and Q states .....	25
3.1.1.9.4.3. Sustained Illumination Experiments and Calculated Spectra.....	27
3.1.1.9.4.4. Temporal Kinetic Studies and a New P State Model .....	29
3.1.1.9.4.5. Thermal denaturation experiments and chromophore analysis .....	31
3.1.1.9.4.6. Comparison with Previous Studies .....	32
3.1.1.9.5. Comments and Conclusions.....	34
3.1.1.10. Further Characterization of the Branched Photocycle.....	36
3.1.1.10.1. Results from Screening Systems .....	36
3.1.1.10.2. Description of the Standard Experiment (Exposure Curve) .....	36
3.1.1.10.3. Temperature Dependence of the Formation of the P and Q-states .....	40
3.1.2. <i>Materials Research at Carleton University</i> .....	44
3.1.2.1. Gel Aging.....	45
3.1.2.2. Summary: Light Scattering Studies.....	45
3.1.2.2.1. Characterization of Refractive-Index Matching Gel Additives.....	45
3.1.2.3. Summary: Development of a Photocurable Polymer Matrix.....	47
3.1.2.4. Development and Characterization of Polymer Hydroglass Systems:.....	50
3.2. BACTERIORHODOPSIN-BASED THREE-DIMENSIONAL MEMORY PROTOTYPES .....	54
3.2.1. <i>Critical Link Prototype</i> .....	54
3.2.1.1. General Description.....	54
3.2.1.2. Operational Basis .....	54
<b>4.0. CONCLUSIONS.....</b>	<b>61</b>
4.1. WHY SOME GOALS WERE NOT MET.....	62
4.2. FUTURE DIRECTIONS .....	64
<b>5.0. REFERENCES .....</b>	<b>65</b>
<b>6.0. APPENDIX: USER MANUAL FOR THE PROTEIN-BASED THREE-DIMENSIONAL MEMORY PROTOTYPES .....</b>	<b>70</b>
6.1. OVERVIEW FOR THE BACTERIORHODOPSIN THREE-DIMENSIONAL MEMORY USER'S MANUAL .....	72
6.2. HARDWARE SETUP FOR THE BACTERIORHODOPSIN THREE-DIMENSIONAL MEMORY .....	72
6.3. SOFTWARE SETUP FOR THE BACTERIORHODOPSIN THREE-DIMENSIONAL MEMORY .....	73

6.3.1. <i>Installing the Software</i> .....	73
6.3.2. <i>Running the Software</i> .....	73
6.5. SOFTWARE DESCRIPTION FOR THE BACTERIORHODOPSIN THREE-DIMENSIONAL MEMORY .....	74
6.5.1. <i>Executing a memory command</i> .....	74
6.5.2. <i>Timing Menu</i> .....	74
6.5.2.1. Timing Menu Commands .....	74
6.5.3. <i>Settings Menu</i> .....	76
6.5.4. <i>Controls Menu</i> .....	77
6.5.5. <i>Functions Menu</i> .....	78
6.5.6. <i>Model Menu</i> .....	79
6.5.6.1. The Model .....	79
6.5.6.2. Least Squares Fit .....	80
6.5.6.3. Software Noise Reduction .....	80
6.5.6.4. Modeling Menu Commands .....	81
6.5.7. <i>Locate Menu</i> .....	81
6.5.8. <i>Advanced Menu</i> .....	82
6.6.1. <i>Mechanical/ Optical Setup</i> .....	88
6.6.2. <i>Electrical Setup</i> .....	90
6.6.2.1. Power Supply Overview .....	90
6.6.2.2. System Overview .....	90
6.6.3. <i>Microcontroller Board</i> .....	92
6.6.3.1. Connector Schematic .....	93
6.6.4. <i>Detector Board</i> .....	94
6.6.4.1. Detector Board Schematic (Part 1) .....	94
6.6.5. <i>Interface Board</i> .....	97
6.6.6. <i>Laser Modules</i> .....	99
6.6.7. <i>3-D Motion Interface Board (3-D Memory only)</i> .....	99
6.7. <i>Communications Protocol for the Bacteriorhodopsin Three-Dimensional Memory</i> .....	102
6.7.1. <i>Advanced Write Format:</i> .....	105
6.7.2. <i>Motor Positioning issues:</i> .....	113
6.8. QUICK REFERENCE SHEET FOR COMMUNICATIONS PROTOCOL TO THE BACTERIORHODOPSIN THREE-DIMENSIONAL MEMORY .....	114

## Table of Figures

<b>Figure 2.1:</b> Structural schematic of bacteriorhodopsin .....	3
<b>Figure 2.2:</b> The Branched-Photocycle Architecture .....	4
<b>Figure 2.3:</b> Correlation of write, read, and erase operations to the BR photocycle.....	5
<b>Figure 2.4:</b> BR Memory architecture .....	6
<b>Figure 2.5:</b> Schematic representation of BR-based routine memory operations. ....	8
<b>Figure 3.1:</b> Schematic representation of BR structure & photocycle, illustrating memory architecture.....	9
<b>Figure 3.2:</b> Hypothetical mutational landscape. ....	10
<b>Figure 3.3:</b> The effect of mutations involving Glu194 and Glu204 on O state kinetics..	13
<b>Figure 3.4:</b> Semi-random mutagenesis.....	14
<b>Figure 3.5:</b> Spectrokinetic screening of semi-random mutants for branched-photocycle memory applications. ....	15
<b>Figure 3.6:</b> Schematic representations of the BR photocycle.....	20
<b>Figure 3.7:</b> Schematic of the apparatus for the sustained illumination and temporal kinetic studies.....	23
<b>Figure 3.8:</b> Absolute (a and c) and difference (b and d) spectra of P- and Q-states .....	25
<b>Figure 3.9:</b> Regeneration of the bR-state at 40°C from the Q- and P-states in 85% V/V glycerol/water .....	26
<b>Figure 3.10:</b> Time resolved difference spectra of a purple membrane 85% V/V glycerol suspension during illumination.....	27
<b>Figure 3.11:</b> Calculated spectra of the two P-states and the Q state.....	28
<b>Figure 3.12:</b> Time-resolved spectrum showing the loss of bR (560 nm) and the rise of O-state (670 nm) .....	29
<b>Figure 3.13:</b> Chart showing the initial rate of formation of P-state and loss of bR.....	30
<b>Figure 3.14:</b> Illustration of the proposed states and transitions involved in the photochemistry of the P and Q states.....	30
<b>Figure 3.15:</b> UV-visible spectra of bR in 85% glycerol heated to 70°C, then cooled back to 25°C and rehydrated.....	31
<b>Figure 3.16:</b> Comparison of the absorption spectra of P & Q states with the terrestrial solar intensity profile at noon at the water surface .....	35
<b>Figure 3.17:</b> Measurement of the O-state at 685 nm. ....	37
<b>Figure 3.18:</b> Typical saw-tooth pattern seen in screening experiments.....	38
<b>Figure 3.19:</b> Arrhenius plot for the formation of P & Q in wild-type bacteriorhodopsin. ....	40
<b>Figure 3.20:</b> pH dependence of O-state formation in wild type bacteriorhodopsin at 40°C .....	42
<b>Figure 3.21:</b> O-state integral and log(time constant) plotted as a function of pH .....	42
<b>Figure 3.22:</b> High pH response for the formation of P&Q in wild type BR.....	43
<b>Figure 3.23:</b> Ionic Strength Dependence of the Formation of the P and Q-states .....	43
<b>Figure 3.24:</b> Mutant Dependence of the Formation of the P and Q-states .....	44
<b>Figure 3.24:</b> Effects of temperature and pH on light scattering of PAm gel. ....	45
<b>Figure 3.25:</b> Light Scattering Comparison of Various Hydrogel Systems .....	46

<b>Figure 3.26:</b> Light scattering comparison novel hydroglass with previous formulations.	50
<b>Figure 3.27:</b> Surface morphology of a PAm hydrogel (top) and a hydroglass (bottom) system.	53
<b>Figure 3.28:</b> BR-Hydroglass sealed with UV cured epoxy	53
<b>Figure 3.29:</b> Block diagram concept of proposed device.	54
<b>Figure 3.30:</b> Overall Block Diagram of the device proposed by Critical Link, based upon concepts provided by the W.M. Keck Center for Molecular Electronics at Syracuse University.	55
<b>Figure:3.31</b> Schematic of the vibration-stabilized optical bench.	56
<b>Figure 3.32:</b> Optical design for the write-laser system	56
<b>Figure 3.33:</b> V-groove fiber holder	57
<b>Figure 3.34:</b> Technical illustration to scale of the final optical design	57
<b>Figure 3.35:</b> Photograph of isolated optical bench prior to insertion into casing	57
<b>Figure 3.36:</b> Individual components that comprise the cuvette base.	58
<b>Figure 3.37:</b> Micro translation stages	58
<b>Figure 3.38:</b> Technical drawing of the overall design for the prototype memory device.	58
<b>Figure 3.39:</b> Close-up of prototype memory device	59
<b>Figure 3.40:</b> Another view of the optical base and associated components	59
<b>Figure 3.41:</b> Full view of BR-based volume-tric memory prototype.	60
<b>Figure 3.42:</b> Expanded view of the optical base and associated components.	60
<b>Figure 3.43:</b> Two views of the completed prototype	61
<b>Figure 3.44:</b> Inner workings of an in-house prototype fabricated at the W. M. Keck Center for Molecular Electronics at Syracuse University	64
<b>Figure 6.1:</b> Bacteriorhodopsin-based three-dimensional memory screening devices developed at the W. M. Keck Center for Molecular Electronics at Syracuse University	70
<b>Figure 6.2.</b> Overview of Screening Apparatus	72
<b>Figure 6.3:</b> Simplified photokinetic model of the bacteriorhodopsin photocycle.	79
<b>Figure 6.4:</b> Mechanical and Optical Layout of the Screening Apparatus	89
<b>Figure 6.5:</b> Power supply module.	90
<b>Figure 6.6:</b> Prototype system diagram.	91
<b>Figure 6.7:</b> Connector Schematic	93
<b>Figure 6.8:</b> Detector Board Schematic (Part 1)	94
<b>Figure 6.9:</b> Detector Board Layout (Part 1)	95
<b>Figure 6.10:</b> Detector Board Schematic Circuit Views (Part 2).	96
<b>Figure 6.11:</b> Interface Board Schematic and Circuit View	98
<b>Figure 6.12:</b> 3-D Motion Interface Board Schematic	100
<b>Figure 6.12:</b> 3-D Motion Interface Board Circuit View	101

## List of Tables

<b>Table 1:</b> Comparison of the five methods of optimizing proteins for device applications using genetic engineering. ....	11
<b>Table 1:</b> Summary of calculated molar extinction coefficients P- and Q- state species.	28
<b>Table 2:</b> Chromophore composition of photochemical and thermal species determined	32



## 1.0. Abstract

The progress in the development of the bacteriorhodopsin-based three dimensional memory prototype from September 1999 through October 2001 of Air Force Contract No. F30602-99-1-0555 is described. During this time period advances in both prototype development and materials enhancement were achieved. The previous Air Force Sponsored effort, Protein-Based Three-Dimensional Memories, Contract No. F30202-98-C-0105, made several factors apparent, the most salient being that bacteriorhodopsin in its native form (i.e., the wild-type protein that has not been altered either genetically or chemically) is incapable of the efficiency necessary for possible commercialization. This fact forced a reevaluation of the research direction of that contract, from one of device development to one of materials optimization. Based on the results of that effort, the research effort described herein focused on three major objectives: (1) Optimization of the protein with respect to operation in the three-dimensional optical memory, (2) Optimization of the polymer matrix that encapsulates the protein, thereby comprising the memory media, and (3) Fabrication of prototype three-dimensional optical memories geared toward use with not only the native protein, but also chemically and genetically manipulated forms.

Directed evolution (DE) was selected as the best way to optimize the protein. This genetic engineering technique offers the researcher the opportunity to explore the genetic mutational landscape of a protein without any *a priori* knowledge of structure-function relationships. As such, it explores mutations that otherwise would be overlooked by more pragmatic approaches. By the end of this contract the DE effort on bacteriorhodopsin was in full operation, although only one round had been completed. The resulting BR variants are currently being analyzed with respect to efficiency and cyclicity. The previous genetic engineering effort has been described in the final report for Protein-Based Three-Dimensional Memories, and the reader is referred to Air Force publication AFRL-IF-RS-TR-2001-279 for more information. Tremendous advances in polymer matrix optimization have been made with respect to long-term stability, shrinkage, and optical clarity. The newest matrix has been made *via* subcontract by Carleton University, and consists of a high-density poly(acrylamide) gel that resists shrinkage and lowers light scattering by several orders of magnitude over previous formulations. Further optimization and evaluation of the new matrix is in progress.

Advancements in prototype fabrication were the primary focus of this effort, culminating in two new in-house designs and a sophisticated unit built with Critical Link, Inc., a local custom electronics firm. These units are capable of 2-3 KB storage in a 1 cm cube, made possible by fiber-optic coupled diode lasers and differential detection. Writing and reading efficiency have been improved by virtue of more powerful diode lasers. All functions are computer controlled *via* an RS232 interface. Although efficiency problems associated with the wild-type protein precluded many features that will in time represent key advantages for commercialization (e.g., parallel spatial light modulator mediated writing, phase & gray-scale multiplexing), these prototypes represent the first true step toward a future commercially viable optical memory architecture.

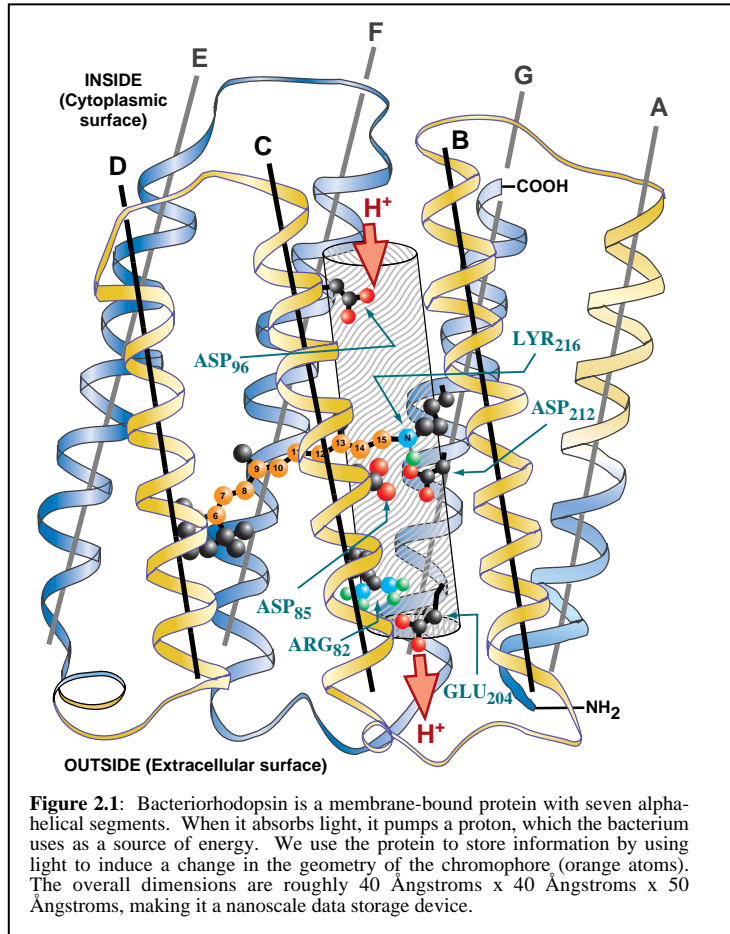
## 2.0 Introduction

The increasing demands of modern computation require innovative solutions to data storage and processing. Conventional architectures are often limited not by processor speed, but by the ability to efficiently handle large amounts of data. Optical architectures for these applications promise potential gains in speed, data throughput, and storage density. In addition, an entirely new class of materials has emerged that is expected to provide practical solutions to these demanding applications; these materials include not only conventional optical and holographic materials, but also of those of biological origin. Present computer memory architectures largely are confined to two dimensions, typically in the form of a disk. The storage density of such devices is ultimately constrained by the physical limitations of the materials, i. e., both the size of the actual bit and the ability to mechanically access that bit is limited by both the material used as a recording medium and the size of the device used to detect it. An approach to increasing storage density that holds a lot of promise is moving into three dimensions, in the form of volumetric optical molecular architectures. In their present form, conventional silicon-based technologies are incapable of making that transition. The need for new materials and architectures is becoming increasingly apparent.

Bacteriorhodopsin (BR) was among the first biological molecules to attract attention as a viable component in molecular electronics and nanotechnology. In the native organism, *Halobacterium salinarum*, the protein acts as a photosynthetic sunlight to chemical energy transducer. Through several billion years of evolution, nature has produced a protein that is remarkably rugged and responds uniquely and efficiently to light. To date, it is the only molecule of biological origin that has been incorporated into a successful commercial holographic device, Fringemaker<sup>®</sup> (Munich Innovative Biomaterials GmbH, Germany), a holographic interferometer for dynamic non-destructive testing applications. In addition, researchers at the W. M. Keck Center for Molecular Electronics at Syracuse University are currently exploring BR as the active storage element in associative holographic memory architectures

Most successful applications of bacteriorhodopsin, including those described above, do not utilize the protein in its native form. Chemical or genetic modifications are often necessary to optimize the protein for a specific application. Chemical enhancements, either in the form of additives or direct synthetic modification, are generally successful, but often at the expense of protein stability. Genetic modifications are often unpredictable, even by the most powerful supercomputers. A relatively new technique in molecular biology, directed evolution, offers a means by which genetic engineering can be used as a tool to produce highly optimized proteins for specific applications.

Bacteriorhodopsin (BR) is a 26 kD membrane-bound photosynthetic protein isolated from the bacterium *Halobacterium salinarum*, a common halophilic resident of salt marshes (**Figure 2.1**). *H. salinarum* has adapted to high salt environments (5 M or 25% NaCl) and can use BR to absorb light energy and convert it to chemical energy. The protein occurs in the membrane of the organism, arranged in a two-dimensional semi-crystalline array of trimers. When oxygen is scarce, the protein is used by the organism in a photosynthetic role, by functioning as a light to chemical energy transducer. The chromophore responsible for absorption of light by the protein is all-*trans* retinal, which is bound via a protonated Schiff base to Lys-216. Light induces an all-*trans* to 13-*cis* isomerization in the chromophore, followed by a series of thermal protein intermediates characterized by different absorption spectra, vectoral proton transport, and ultimately the reisomerization of the chromophore with consequent re-generation of the protein's resting state. The last of the thermal intermediates is the O-state, which absorbs maximally at 640 nm. Exposure of this state to 640 nm light results in a small segment of the protein population being driven into the branched portion of the photocycle, first characterized in 1993 [1], and containing two intermediates, P and its thermal product Q. The chromophore in both intermediates has a 9-*cis* configuration. The Q-state is very long-lived, and is proving to be a promising candidate for long-term data storage.



The ultimate goal of this project is the creation of a new industry based on a novel product (the bacteriorhodopsin-based volumetric optical memory); therefore, the development and refinement of all aspects of this technology is of the utmost importance. A production strategy is necessary to create a new product capable of spawning an independent industry. Additionally, the industry should have the technical foundations and merit necessary to enable continuous research, development, and refinement, thereby securing its place as a competitive technological leader. The new opportunities presented by such an effort have the potential of bringing increased industry involvement, as well

as employment. It is for these reasons that we plan to not only explore new architectures for our device, but also the different techniques necessary for the manufacture of a commercial product. In order to do this, it will be necessary to take into consideration the limitations imposed by the manufacturing process. It will therefore be necessary to explore component design and fabrication with an emphasis on mass production and the implementation of low cost solutions.

## 2.1. Overview of Bacteriorhodopsin-Based Volumetric Optical Memory.

The proposal for the original contract, Protein-based Three-dimensional Memories (No. F30602-98-C-0105) has a detailed description of both the theory behind the BR-based volumetric memory, and advantages over other volumetric optical architectures described in the literature (e.g., cyclicity, one-photon vs. two-photon issues, non-destructive writing and reading operations, etc.). The reader is referred to that document for further detail. However, a brief overview is included here for the sake of convenience.

In 1993, researchers in Germany described photoproducts that were produced upon illumination of the O-state [1]. Instead of converting to either BR or another main photocycle intermediate, a branching side reaction was found that contained two novel intermediates. These photoproducts, denoted as P and Q, were blue-shifted in absorbance with respect to most of the other photocycle intermediates, and were characterized as having a 9-*cis* chromophore. In addition, the Q-state displayed enhanced stability. The O-state acts as the entry point to the branched photocycle. Upon absorption of red light (~640 nm), an isomerization of the all-*trans* retinal chromophore occurs at the C9-C10 double bond, forming the P-state (490 nm). The resulting chromophore configuration is not stable in the binding site, presumably due to steric interactions, ultimately breaking the bond between the chromophore and the protein. Concurrent with the cleavage of this bond is the formation of the Q-state (380 nm), which has a stability on the order of years. For the purposes of the branched-photocycle architecture, the bR state is assigned as a binary unit ZERO, and the P- and Q-states are collectively assigned as a binary unit ONE

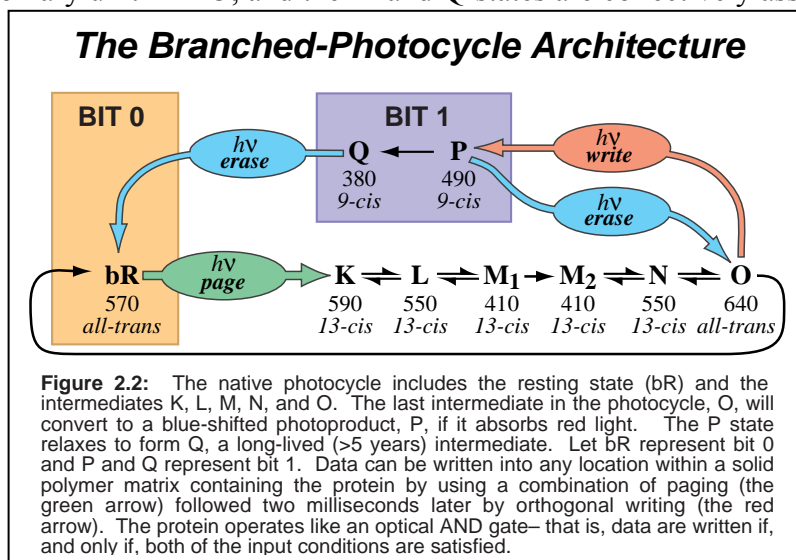
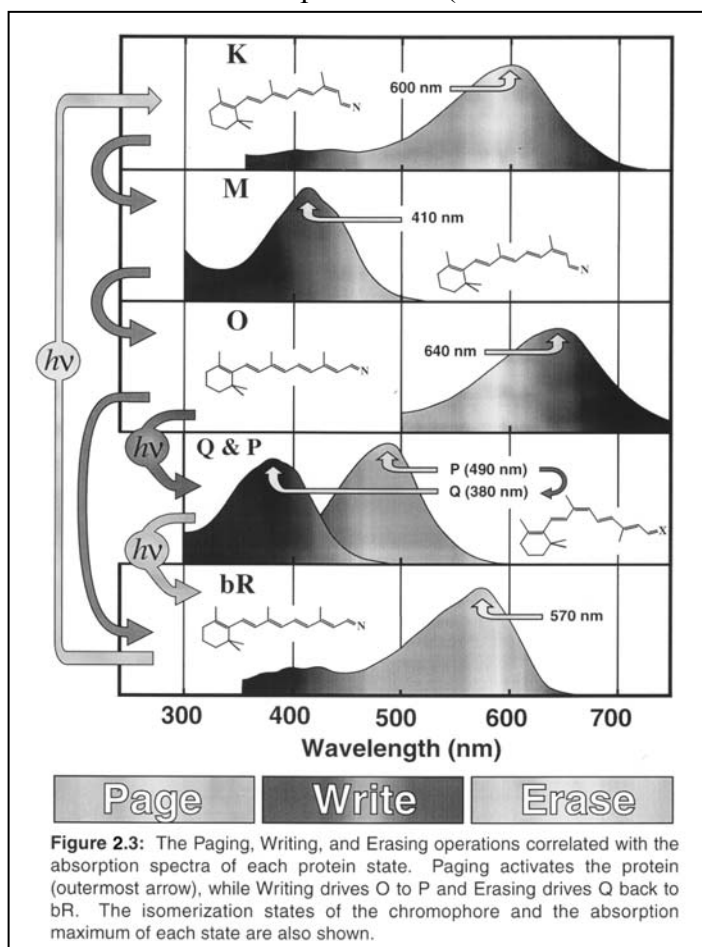


(Figure 2.2). Problems associated with previous architectures (two-photon-based systems) are easily circumvented by the unique nature of the branched-photocycle, in that it produces intermediates that are unaffected by the wavelengths of light used in write and read operations (i.e., unwanted photochemistry is

rigorously avoided). Two photons are still required to write data, but they are absorbed by the protein sequentially, rather than simultaneously as in the two photon architecture.

The basis of the sequential one-photon branched photocycle architecture is illustrated in **Figures 2.2 and 2.3**. In order to access the branched portion of the photocycle, and thereby change a binary ZERO to a binary ONE, two conditions must be fulfilled: the bR photocycle must be initiated with a photon of green light, followed by a photon of red light at the appropriate time interval to drive O to the P-state. If, and only if, these two criteria are fulfilled, will data be written in the cube. The first process is referred to as paging, and involves initiating the BR photocycle with a photon of green light. The term “paging” refers to the process of using a green laser to select a slice within the cube where the protein is activated. The protein within this page starts to cycle through the photocycle intermediates, until the majority of the protein exists within the O-state after about 2 ms. At this time, the red data laser is fired, which drives the O-state into the branched photocycle, forming the P and Q intermediates. In this way, the protein acts as an optical AND gate: if only the green paging laser is fired, photochemistry is initiated and the net effect is that the protein cycles through the intermediates and returns to its resting state, resulting in the re-writing of a binary ZERO. If only the red data laser is fired, no action is stimulated in the protein because the wavelength of the data laser is not within the bR absorption band (net result = no change). However, if the green paging

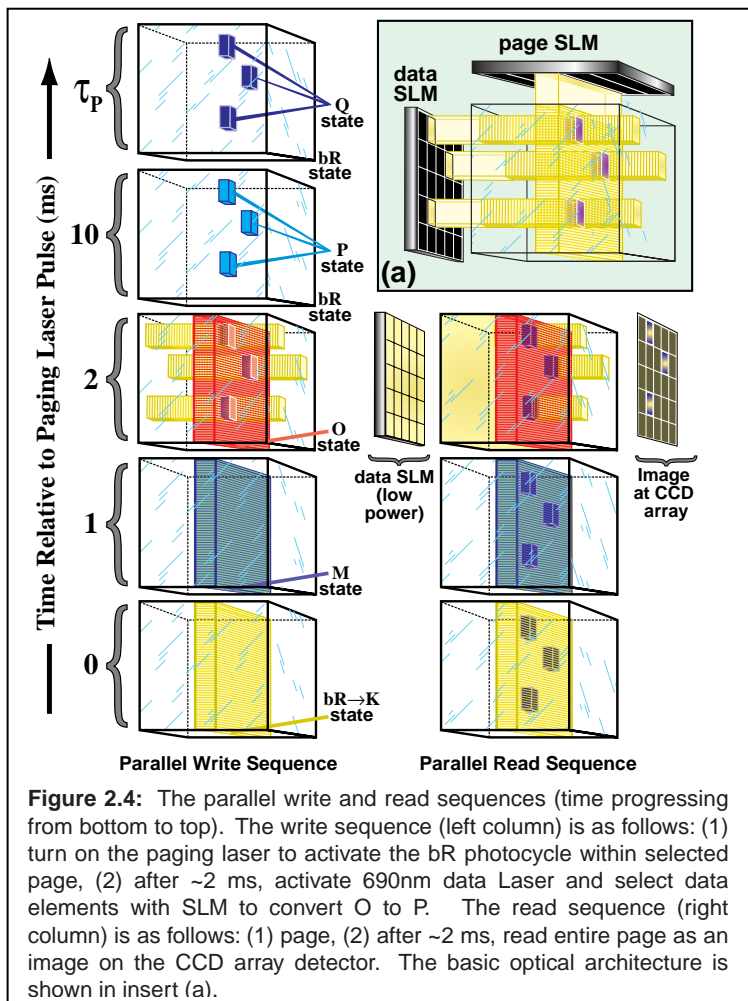
laser is fired, followed by the red data laser at the appropriate interval (after the paging laser has been turned off), protein that exists in the O-state is driven into the branched photocycle, the P-, and then Q-states are formed, and the formation of a binary ONE results. The combination of orthogonal laser excitation (enabling facile access to any volumetric element in three dimensions, as defined by the cross section of the two laser beams) and the energetically and temporally separated states of the branched photocycle, provides a realistic basis for the storage of information in three dimensions.



**Writing:** Figure 2.4 illustrates both the parallel write and read operations for the sequential one-photon branched photocycle architecture. The process of

orthogonal paging is shown in insert (a): volumetric elements within the cube are defined by the cross-sectional volume defined by the paging and data lasers. Note that these two lasers are not fired simultaneously, as illustrated in **Figure 2.4** (right- and left-hand columns). The vertical axis denotes time relative to the firing of the initial paging laser. To initiate the writing process, the paging lasers are fired to activate the protein. Photochemistry is initiated and after approximately 1 millisecond, the bulk of the protein excited during paging has cycled into the M-state. After an additional ms (2 ms relative to paging) the protein exists in the O-state, and the data laser is fired. The latter is modulated by some sort of spatial light modulator that defines exactly what volumetric elements will be irradiated in the paged region. Within these volumes, the branched photocycle is initiated photochemically by driving the O-state into the P-state. Finally, P decays to Q over several hours ( $\tau_p$ ), completing the writing process. The full writing sequence (to the P-state) is complete in roughly 10 ms, the time necessary for the protein to complete the photocycle.

**Reading:** The reading process is unique in that it only examines those elements of data that exist as binary ZEROS. The operation starts out identically to that used to write data (**Figure 2.4**, right-hand column). The paging laser is used to select the page of interest, and after a few milliseconds, the majority of the protein excited by the paging operation exist in the O-state, just as in the writing process. Once again, the data laser is fired, but this time at a much lesser intensity. The amount of light allowed through the spatial light modulator is adjusted to be absorbed completely by the protein in the selected page (0.01% of full intensity). No appreciable photochemistry



is stimulated by the low intensity laser light (the O → P transition is not very efficient), and those volumetric elements existing in the P- and/or Q-states are invisible to the wavelength used. Therefore, regions of the cube that exist as binary ones transmit the low-intensity light, because it can't be absorbed by P ( $\lambda_{\max}=480$  nm) or Q ( $\lambda_{\max}=380$  nm).

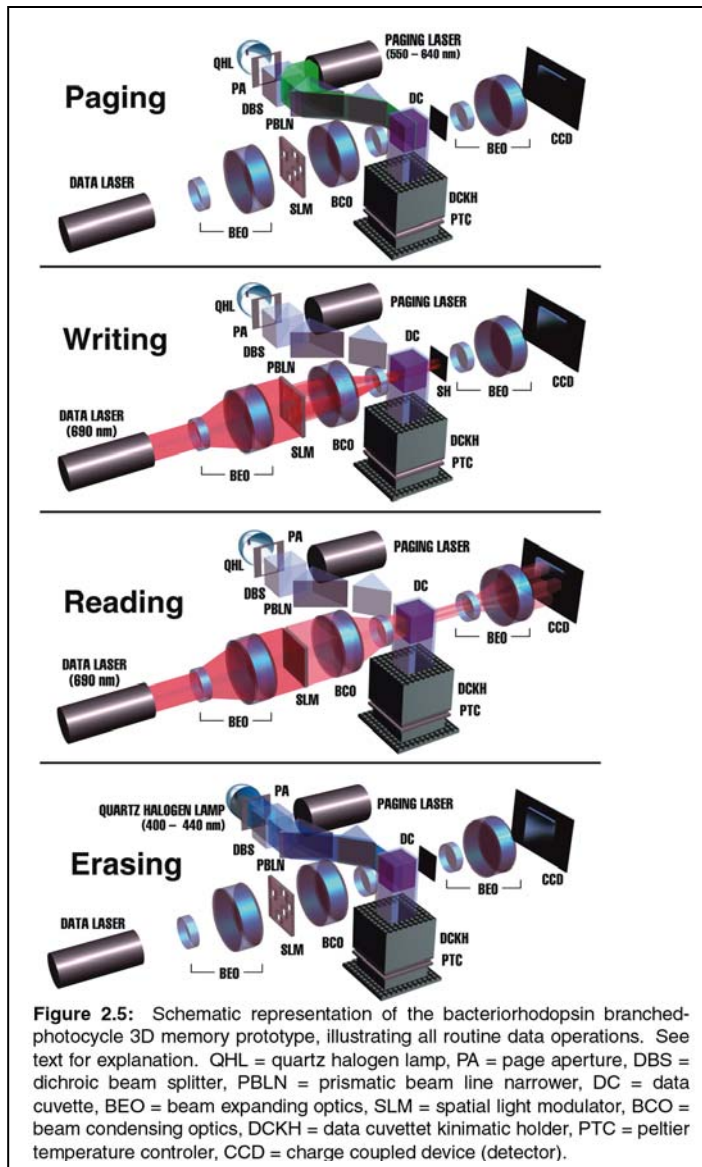
nm). The transmitted light is imaged onto a CCD or CID detector. If the page is imaged prior to, and then again during the firing of the data laser, a differential read can be done which has the added benefit of enhanced sensitivity. In this way, the read process essentially examines only the binary ZEROS, while leaving the ONES unperturbed, resulting in a reading operation that is totally nondestructive. Because the O-state has an absorptivity better than 1000 times larger than that of the remaining volume elements combined, a very weak read beam can generate a large differential signal. Erasing operations are currently implemented with a standard Xenon lamp to provide the blue light necessary to drive Q back to BR; because blue diode lasers do not yet commercially exist, at this time data can only be erased via a global operation. Figure 2.5 shows a schematic of the modular prototype developed during the first year of the project.

Before commercialization can be seriously considered, several issues must still be addressed. As will be discussed below, the most serious factor that precludes commercialization at this point is the protein itself, which has proven not to be efficient enough to be competitive with conventional technologies. The research effort described below, funded through AFRL, explored ways through genetic engineering to address these problems, especially through a relatively new technique known as Directed Evolution. This is a method in molecular biology that offers a means by which genetic engineering can be used as a tool to produce highly optimized proteins for specific applications. As part of the research effort described herein, a sizeable effort in standard molecular biology techniques, predominantly site-directed mutagenesis (SDM), was used to produce improved bacteriorhodopsin variants. Considerable progress toward an optimized material has been made, as illustrated below. The rationale in determining the direction of SDM on BR was to produce mutant proteins that exhibit enhanced yields of the O-state, the gateway to the branched photocycle architecture. More O should translate into enhanced yields of P&Q—progress described below has resulted in an improvement of the O-state yield by several orders of magnitude. The protein has also proven to be extremely sensitive to the chemical environment, with enhanced O-state formation at lower pH values and enhanced P&Q formation at higher temperatures. Results from this effort indicate despite the fact that O-state formation is favored at lower pH, formation of the P-state follows the opposite trend. Therefore a balance has to be found between the two factors—this is currently an ongoing portion of the research effort.



What follows below is the progress that has been made during the period between September 1999 through October 2001. Because there is a great deal of overlap between this effort and the previous contract between Syracuse University and Air Force Research Laboratories (Contract No. F30602-98-C-0105; Protein-Based Three-Dimensional Memories, Final Technical Report AFRL-IF-RS-TR-2001-279, concluded in September of 2000), some of that work will be included here. The interested reader is referred to that effort's final report for more detail. Progress toward the development of the bacteriorhodopsin-based three-dimensional memory, as a result of this research effort, will be described in this report. The following areas will be discussed.

- Development of polymer matrices for protein encapsulation and stabilization, exhibiting reduced light scattering and long term stability (i.e., reduced tendency to contract).



- Development of mutant proteins with enhanced ability to operate as a light activated storage media, through both Site Directed Mutagenesis and Directed Evolution.
- Kinetic evaluation of mutant proteins with respect to efficiency of O-state production, access to the branched photocycle, and photochromic efficiency.
- Characterization of the branched photocycle of bacteriorhodopsin.
- Development of an electronic interface between the computer and memory to facilitate invisible background operation of the memory device.



- Construction and demonstration of fully functional miniaturized memory prototypes.

All of these accomplishments will be described in detail below.

### 3.0. Progress Detailed by Task

In this section progress will be detailed in a format loosely based on the tasks described in the original Statement of Work.

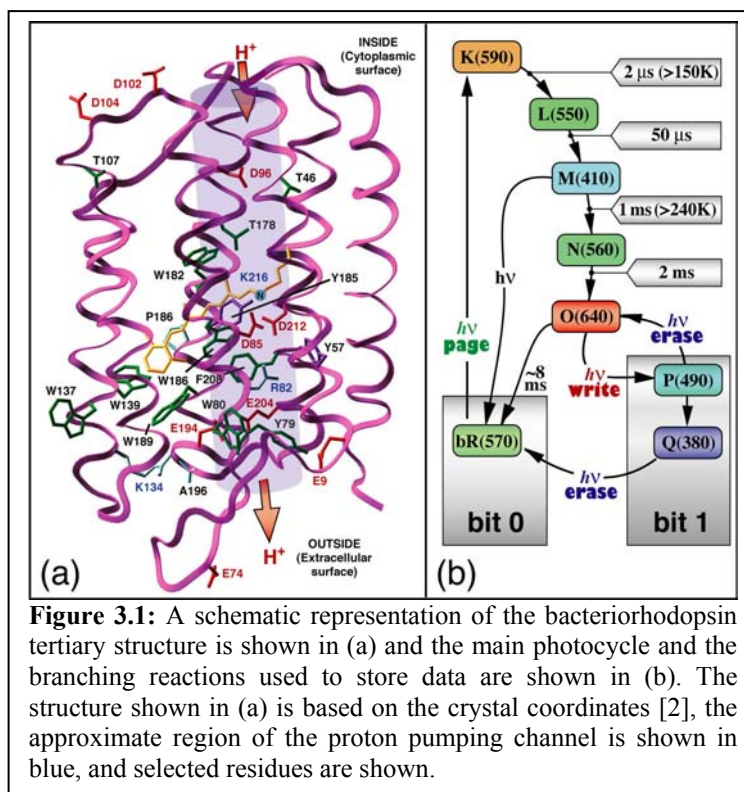
#### 3.1. Materials

The materials work performed during this contract had two basis goals: (1) Optimization of the polymer host matrix which encapsulates the protein and (2) Optimization of the protein, itself, with respect to efficiency by which the branched photocycle is accessed. The first goal was handled both in-house and under subcontract to Wayne Wang at Carleton University. Research and progress toward the second goal was performed both at Syracuse University and the University of Connecticut.

##### 3.1.1. Optimization of the Protein

Perhaps the most critical factor of materials optimization is the work done to optimize bacteriorhodopsin itself. One of the most difficult “lessons learned” about this project has been that BR failed to live up to its initial potential as a memory storage element.

The branched photocycle is real and it can be used to store information in three dimensions, as illustrated later in the report. However, the efficiency with which the branched photocycle can be accessed is extremely low; low enough that it was quickly realized that the wild-type protein would not suffice as an active element of a three-dimensional optical memory (at least not in a



commercially-viable sense).

Several approaches have been taken to remedy this problem, mainly in the form of optimization of the chemical environment (i.e., pH, salinity, chemical additives) and/or actual genetic manipulation of the protein. Both approaches have been taken during this

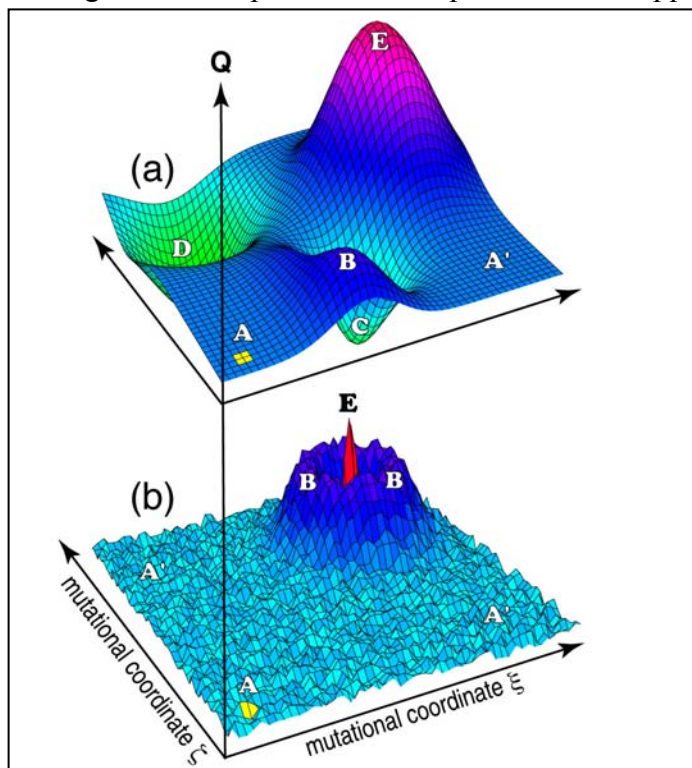


**Figure 3.2:** Hypothetical mutational landscapes for fluid traits (a) and spectrokinetic optimizations (b). The native protein is located at the central locus of the yellow squares, the mutational coordinates  $\zeta$  and  $\xi$  are arbitrary, and the vertical axis measures an arbitrary Q factor. Starting at 'A', the ultimate goal of our mutational strategies is to discover the optimal protein, represented by peak 'E'. The 'A' and 'A'' regions represent mutations that have little impact on the Qfactor, the 'B' regions are local maxima in Q and the optimal mutation is at the peak labeled 'E'. Cyclical optimization will typically find 'E' in the fluid case, but is unlikely to find 'E' in the spectrokinetic optimization without good modeling or operator intuition. For fluid characters such as temperature, less variation is expected (Fig. 3a). The overall temperature stability of the protein might decrease (troughs 'C' or 'D'), but has a comparable chance of increasing (peaks 'B' and 'E'). Figure 3b shows the mutational landscape for more complex characteristics such as spectrokinetic properties, in which most of the performance is localized in specific regions of the protein. The mutational surface is probably a rugged landscape with numerous local minima.

contract, but the latter—genetic manipulation—is by far the most powerful. The key issue for this discussion is how genetic engineering can be used to optimize the protein with respect to maximizing the efficiency of the branching reaction discussed earlier.

This section outlines some of the current methods that are being used to enhance the yield of the **O** state and the quantum efficiency of the **O**  $\rightarrow$  **P** photoreaction. Note that the **O** state and bit 0 are different entities (see Figure 3.1B). Bacteriorhodopsin can be optimized in one of two ways: chemical modification of the chromophore and genetic and/or chemical modification of the protein. To assist modification, strains of *H. salinarum* are used that are deficient in either the chromophore or the BO polypeptide, but not both. Retinal-deficient strains produce BO without incorporating a chromophore and provide an efficient method of generating analog proteins with synthetically modified chromophores [3, 4]. We also use the BO-deficient cell line L33 [5], which contains a DNA insertion within the gene encoding BO, *bop*. Production of native BR is abolished in L33,

allowing expression of mutant proteins. Strains in which the *bop* gene is deleted or replaced with a selectable marker have also been used for genetic modification of BR [6].

The principal approaches to genetic engineering of proteins for device applications are compared in Table 1. The *efficiency* of a method is a qualitative measure of how much operator effort and intervention is required to generate a successful mutation. A *highly efficient* method is one that requires little if any operator intervention during the optimization process. Type II directed evolution is the best choice in this regard. The *specificity* refers to the selectivity available with respect to modification of individual residues at specific locations within the primary structure. Highest specificity (single residue, specific replacement) is provided by site-directed mutagenesis. The *variability generated* parameter is a qualitative measure of the control one has (or perhaps loses) in going from a site-specific to a more randomized modification of the protein. Semi-random and random mutagenesis produce the highest degree of variability, but in some cases may provide too many degrees of freedom. Directed evolution methods provide no control over the amount of variability generated. The *primary use* parameter is self-explanatory, but the reader should note that this table provides only one example for each method and the entries in this row should not be viewed as mutually exclusive. Using Table 1 for comparative reference, the methods and procedures as well as the advantages and disadvantages of each of the five methods will be reviewed.

<b>Table 1. Comparison of the five methods of optimizing proteins for device applications using genetic engineering</b>					
<b>Technique methodology</b>	<b>Site-directed mutagenesis</b>	<b>Semi-random mutagenesis</b>	<b>Random mutagenesis</b>	<b>Directed evolution Type I</b>	<b>Directed evolution Type II</b>
Efficiency	∞ modeling	Medium	Medium-High	High	Highest
Specificity	Single residue	Local region	Global <i>bop</i> gene	Colony or protein	<i>Halobacterium salinarum</i> cell
Variability generated	Low	Medium	High	N/A	N/A
Primary use	Fine-tuning	Narrowing in on optimal mutant	New search	Protein/colony screening	Organism selection
Requires	Modeling, or <i>a priori</i> knowledge	Some modeling	No <i>a priori</i> knowledge	High throughput and sensitive screening	Truncation selection
<p>The efficiency of a method is a qualitative measure of how much operator effort and intervention is required to generate a successful mutation. A highly efficient method is one that requires little, if any, operator intervention during the optimization process. Type II directed evolution is the best choice in this regard. The specificity refers to the selectivity available with respect to modification of individual residues at specific locations within the primary structure. Highest specificity (single residue, specific replacement) is provided by site-directed mutagenesis. The variability generated parameter is a qualitative measure of the control one has (or perhaps loses) in going from a site-specific to a more randomized modification of the protein. Semi-random and random mutagenesis produce the highest degree of variability, but in some cases might provide too many degrees of freedom. Directed evolution methods provide no control over the amount of variability generated. The primary use parameter is self-explanatory but only one example for each method is provided and entries in this row should not be viewed as mutually exclusive.</p>					

A conceivable mutational “landscape” that the mutagenic optimization process surveys is shown in Figure 3.2. This figure depicts the potential outcomes of optimizing a protein for device applications. There are several results that are possible, depending on the characteristics being measured. Assuming that a triple mutant confers the optimal protein, a single mutation (peak B) might provide significant improvement. However, the optimal protein (peak E) might be surrounded by double mutant troughs owing to

interference effects, and these are very common when key mutations involve charged residues.

### 3.1.1.1. Site-directed mutagenesis

The ability to express BR and its site-directed mutants within the native organism, *H. salinarum*, is crucial to materials optimization [5]. The native organism provides the cellular machinery to express the protein within the purple membrane, and it is the crystalline lattice of the purple membrane that confers the high photochemical and thermal stability that characterizes this system [7].

Although site-directed mutagenesis has been the primary technique for optimizing BR for device applications, it has a fundamental flaw. This technique is rarely useful without access to a good model for the molecular process that is to be optimized. The usefulness of site-directed mutagenesis is proportional to knowledge of protein function obtained from crystal structures and modeling programs. Space limitations prevent a serious overview of BR modeling here, and the reader is referred to recent reviews for a perspective on current status [8, 9]. It is important to note that modeling can be based on theory or experiment, and is at its best when operating in synergy. A good example was the development of the D96N mutant, which was optimized for holographic applications [10, 11].

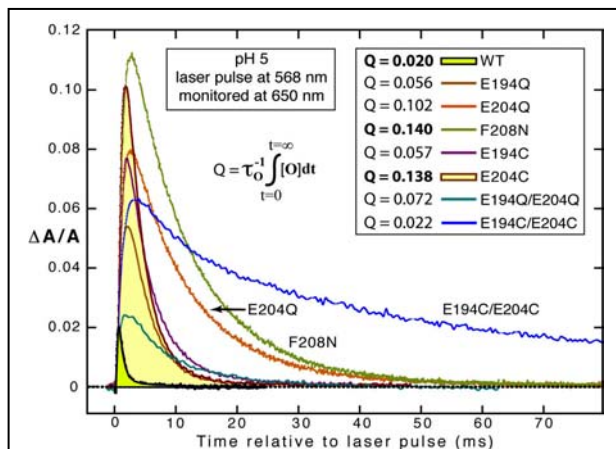


**Figure 3.3:** The effect of mutations involving Glu194 and Glu204 on O state kinetics, measured at pH 5.0. Wild-type (WT) protein is shaded in green and has the smallest Q value of all proteins studied. The O state lifetime in WT is 6–8 ms. The O state lifetimes of E194Q and E204Q are 70 ms and 125 ms, respectively. The double mutant E194C/E204C has the longest O state lifetime reported yet, with a lifetime of ~1 s. This represents more than a 100-fold increase in the O state decay time. However, E204Q has the largest Q value.

The application explored here requires mutations that optimize five variables simultaneously: the formation time of O state (minimize), the decay of O state (optimize), the quantum efficiency of the O → P photochemical transformation (maximize), the efficiency of the P → Q hydrolysis (maximize) and the lifetime of the Q state (maximize). It is virtually impossible to predict which single or double mutations will accomplish these tasks simultaneously. Complex systems such as the memory proposed here have too many variables to limit optimization to site-directed mutations. Nevertheless, one variable of importance to the memory was optimized based on modeling. A series of mutations were constructed in house involving Glu194 and Glu204, both of which have been shown to be important participants in the



photocycle.  $\mathbf{O}$  state lifetimes and  $Q$  values for a sample of mutants are shown in Figure 3.3.

#### **3.1.1.2. Screening versus selection**

All mutational strategies used to create protein variants rely on a screening or a selection process to achieve the goals. Screening involves inspection of a population for a given characteristic (usually a phenotype of interest), but places no limits on the viability of the organisms that do (or more importantly do not) possess that given characteristic. A simple example of screening would be picking all quarters out of a mixed assortment of coins. The population is being screened for quarters, yet all other phenotypes still exist (i.e. dimes, nickels, pennies). In selection, there is a predetermined mechanism that allows only a certain population to survive. An example of selection can be found in construction of site-directed mutants. Only those organisms that possess the plasmid that confers novobiocin resistance will live and persist in the population. To follow the same example used earlier, if one uses a coin sifter to allow all the other coins except quarters to fall through, leaving only quarters, one has selected for quarters. It should be evident from this discussion that selection is the more efficient (and technically more difficult) of the two processes. The main advantage of selection is that smaller sample sizes need to be screened to detect an optimization.

#### **3.1.1.3. Random mutagenesis**

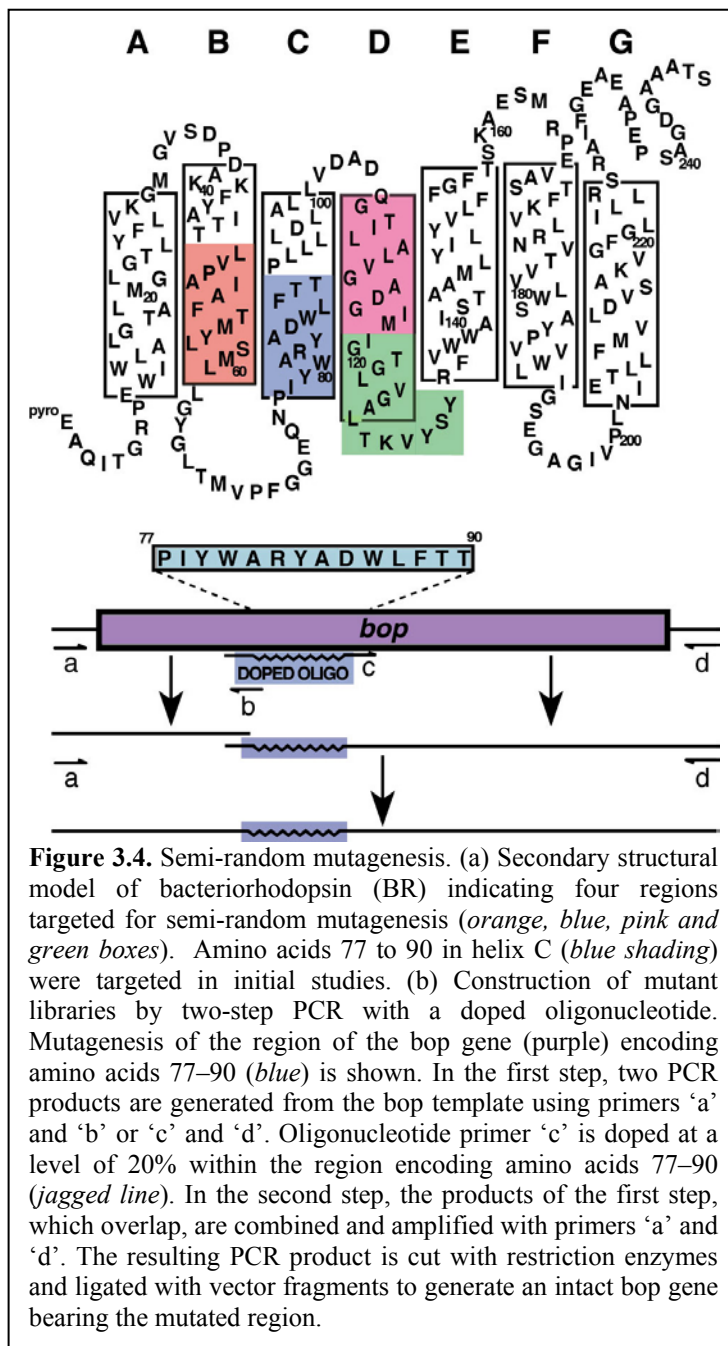
The next step in the genetic optimization process is to create random mutations and observe the impact of these mutations on the desired properties. This process requires screening of the mutations to determine which should be used as templates for further exploration. If one is very lucky, a single random-mutation cycle can yield a significantly improved protein. More commonly, four or more cycles are required to achieve a significant improvement. Random mutations are as likely to be destructive (or more so) or neutral as they are constructive. The total number of unique mutations for a protein the size of BR (248 residues) is 4712 single mutations and 11,056,708 double mutations. It is clear that a single mutagenesis cycle might well produce nothing of value. In the next section methods of restricting the location of random mutations to improve the probability of success will be examined.

There are many available methods to randomly mutate BR (for examples see [12-14]). The net result is a population of mutant proteins with no *a priori* bias of location in the sequence. A combination of methods can be used to generate controlled numbers of randomly distributed mutations.

#### **3.1.1.4. Semi-random mutagenesis**

Semi-random mutagenesis essentially combines site-directed and random mutagenesis to achieve high mutagenesis efficiencies over a limited region. The approach was pioneered by Sauer and co-workers in structure-function studies of soluble

proteins [15], and has been used by others to examine membrane protein folding and function [16]. Krebs and coworkers have adopted semi-random mutagenesis to determine the structural features that guide BR biogenesis in *H. salinarum*. But this method also has significant advantages for bioelectronic optimizations, as described here. In this technique, the complete *bop* sequence is divided into 17 segments of ~15 targeted amino acids that are mutated at a high rate without disturbing the surrounding sequence. Mutations are created by PCR using a “doped” primer that is synthesized with a mixture containing 80% of the wild-type nucleotide and 6.6% of each non-wild-type nucleotide at each position within the targeted region. At this doping level, roughly five amino acid substitutions are predicted per mutant based on Monte Carlo calculations [16] (Krebs, *et al.*, unpublished results). As shown in Figure 3.4, the doped oligonucleotide is combined with additional primers in a two-step PCR reaction. The resulting mutant *bop* fragment is

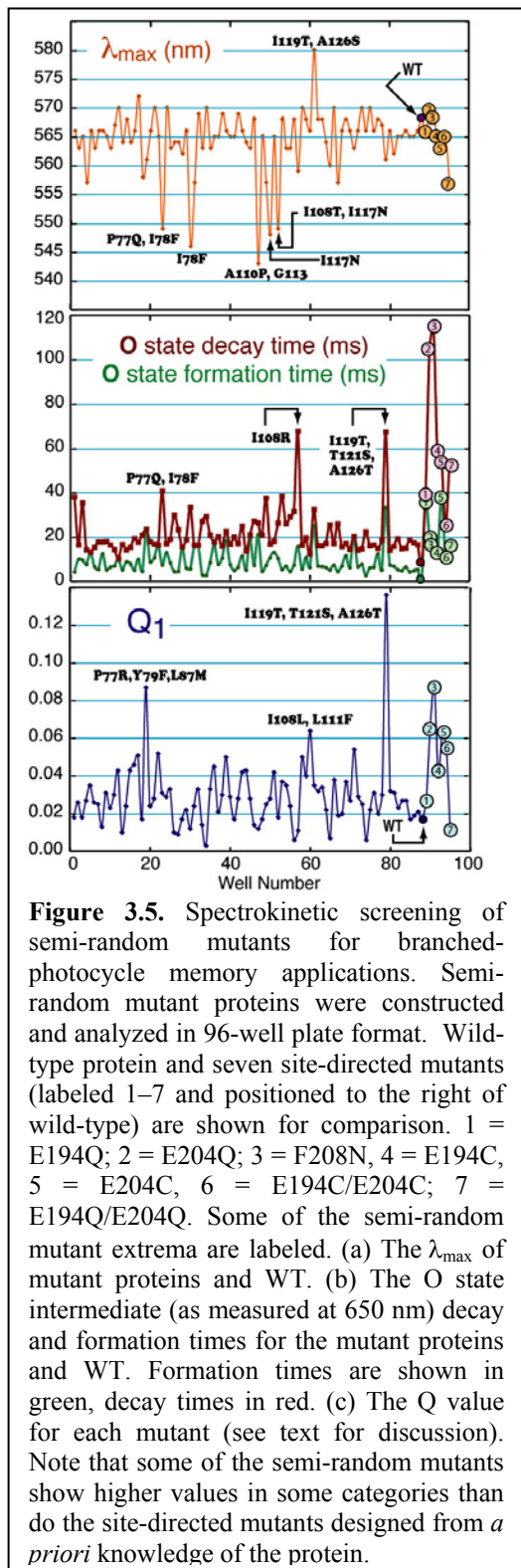


digested with restriction enzymes and ligated with plasmid fragments to generate a plasmid library of at least 3000 mutant *bop* genes in *E. coli*. The pooled library is transformed into an *H. salinarum* strain developed specifically for high-efficiency *bop* mutagenesis [6], and recombinant colonies containing a single copy of the mutant *bop* genes are isolated by homologous gene replacement [6, 17].

Because the mutations within the targeted region are random, the recombinant colonies exhibit a range of colors, reflecting a variation in BR spectral properties and expression levels among the mutants. The current analysis is limited to purple colonies. More than one hundred purple mutants in four regions of BR have been isolated (Figure 3.3) and sequenced at the nucleotide level. An average of 1.2 amino acid substitutions is observed among purple mutants. This value is lower than the expected value of five

substitutions per mutant, presumably because a higher number of substitutions interferes with formation of native bR.

To identify variants with potentially improved photonic properties, the purple



membrane from semi-random mutants was partially purified in 96-well format by repeated ultracentrifugation. The BR in these samples was then screened for variation in spectral characteristics and photocycle intermediate lifetimes, particularly that of the **O** intermediate (Figure 3.5). UV-visible spectra, **O** state formation, and **O** decay times were collected for each mutant, and the  $Q$  value was calculated (see Figure 3.3). Despite the fact that these mutants were not developed *a priori*, some of them show  $Q$  values higher than those for site-directed mutants designed using modeling methods and structural information. The triple mutant I119T/T121S/A126T shows a  $Q$  value which is ~50% higher than the largest  $Q$  value for any site-directed mutant. Site-directed mutagenesis is currently being used to dissect the contribution of particular residues within this multiple mutant.

### 3.1.1.5. Directed evolution

One of the most interesting developments in materials research is the recent use of directed evolution and combinatorial methods to optimize materials [18-21]. One starts with the premise that nature has already produced some very sophisticated materials through evolution. The challenge in using directed evolution for materials optimization is establishing a selection method that focuses on the desired properties of the material generated by the host.

The use of directed evolution cannot guarantee the creation of the ultimate material, because the number of possible mutations and the time it would take to explore all the possibilities is well beyond that available in

any grant cycle or even scientific career. But directed evolution does provide a method of exploring a large number of possible mutations in a systematic way which yields the highest probability of improving the properties of a biological material.

Directed evolution can be divided into types I and II, neither of which are discrete but rather represent a continuum of procedures that start with screening and end with selection. The major difference between Type I and Type II directed evolution is the level at which the screening/selection is implemented. Type I includes protein screening at the colony/protein level, whereas Type II includes screening/selection of BR in individual cells. Both methods entail identifying proteins with the highest  $Q$  values, and using these mutants in the next round of screening.

Type I directed evolution involves high-throughput level screening of large numbers of colonies or purified proteins in 96-well plates. Because *H. salinarum* cells burst when placed in water, colonies can be placed in small aliquots of water and screened in the same 96-well plate format as would be done with isolated protein. Direct screening on colonies of *H. salinarum* avoids the need for protein isolation, but at the cost of introducing more scattering to the sample.

Type II directed evolution deals with detection of optimized forms at the microscopic organismal level, and represents the most powerful technique. Screening and selection are used in tandem. A population of *H. salinarum* cells passes through an automated screening device consisting of laser diodes and a CCD detector array. This device is essentially identical to the write process in the memory. Those cells that show the most conversion to **P** and **Q** states, (as monitored by a concomitant loss of **O** state), are separated from other cells and shunted to a collection vessel. The *bop* gene sequence from these cells is obtained using *in vivo* PCR, and favorable mutations are used for the next round of optimization.

Type II directed evolution is much more efficient than Type I but is more difficult to implement. Because individual organisms are being monitored, cell to cell variation might be problematic. In Type I directed evolution this variation is accounted for by looking at thousands of organisms or protein patches simultaneously. However, the rewards for Type II directed evolution are superior; this method provides the greatest possibility for high throughput detection of the mutant that is best optimized for device applications.

#### **3.1.1.6. Mutational Strategies**

The extent to which the variation in a population increases is dictated by the choice of mutagenesis method. Site-directed mutagenesis is used to explore small changes by changing one residue, and is used to fine-tune a particular mutant. For example, existing site-directed mutants can be combined with mutants found in Type I and Type II screening and selection. Current efforts include incorporation of the Glu-194 and Glu-204 mutants with the triple mutant I119T/T121S/A126T in an attempt to combine favorable properties from different sources.



Some techniques are designed to explore a greater area of the mutational landscape for a given protein than others. For semi-random mutagenesis, the mutational space explored is greater compared to site-directed mutagenesis. A new optimum might be reached instead of continuing to improve an original optimization. Random mutagenesis presents simultaneous advantages and disadvantages: it can be used to find new regions in the protein for optimization, but at the cost of neglecting the original optimization. Strategies for optimizing photochemical properties must take into account the localized nature of the mutational landscape (e.g. Fig 3b). Once the key regions are discovered, semi-random mutagenesis may represent the most productive approach.

### **3.1.1.7. Summary**

Although evolution has optimized proteins for many characteristics relevant to device application, further optimization is usually desirable. In this review, five different genetic engineering approaches have been examined, ranging from single residue replacement through randomized replacement to directed evolution. Our discussion centered on the current problem of optimizing bacteriorhodopsin for a three-dimensional memory system, and this problem is challenging because the performance of the protein in this environment requires the simultaneous optimization of three variables. Modeling does not describe photochemical processes at a high enough level to permit the use of site-directed methods as the sole approach. Site-directed and semi-random mutagenesis have created successful mutations, and to date a 700-fold improvement in the performance of the protein in the three-dimensional memory has been realized. Directed evolution offers the best potential, although the difficulty of *in vivo* measurement of the protein photochemical properties remains problematic and leads to inefficient screening. A major emphasis of our current research is to optimize the speed and accuracy of *in vivo* screening. Although the discussion has concentrated on bacteriorhodopsin, the methods described herein are relevant to the optimization of any protein for device application. A key requirement is to determine the nature of the mutational landscape and choose a technique that is optimal for exploring a global or localized function. We anticipate that rapid improvements in the methods, procedures and equipment available for genetic manipulation and screening will lead to significant advances in bioelectronic materials during the next decade.

### **3.1.1.8. Goals for Application of Directed Evolution to Bacteriorhodopsin**

As applied to bacteriorhodopsin, SDM has proven over the last decade to be an extremely powerful tool for determining structure-function relationships. Indeed the state-of-the-art has arrived at a point where the functions of many of the amino acids involved in the proton pump mechanism are thought to be fairly well understood. For example, mutations at D85 (aspartic acid residue no. 85 in the primary amino acid sequence of BR) are known to influence the nature and lifetime of the M-state. Likewise, mutations at E194 and E204 (E=glutamic acid) are known to affect the O-state. The latter class of mutations, i.e., those that influence the O-state, are of considerable interest to the development of the branched-photocycle memory due to the fact that the O-state

serves as the gateway to the P- & Q-states. As detailed previously, the transition from O to P is fairly weak, with quantum yield determinations ranging from  $10^{-4}$  to  $10^{-2}$ . The most likely explanation for this weak transition is the formation of a 9-*cis* chromophore in a binding site that has evolved to accommodate either an all-*trans* or 13-*cis* chromophore. Indeed, once the 9-*cis* chromophore has been formed (P-state), it is unstable enough in the binding site that the Schiff base bond to the protein is hydrolyzed so that the chromophore can re-adjust into a more favorable orientation.

The obvious goal for genetic engineering of bacteriorhodopsin from the perspective of the branched photocycle is to target amino acids that affect the O-state in a way that will either enhance the formation of the P-state by increasing the quantum yield for its formation, or by increasing the amount of O-state available to be driven into the branched photocycle. Either way, the net result is an increased efficiency with which information can be written. The unfortunate aspect of genetic engineering as a general technique is that the effects of a specific mutation or set of mutations can be extremely hard to predict. A good example of this is the mutant F208N, where the phenylalanine (F) at position 208 is replaced by an arginine. F208 has never been reported to have a well-defined role in bacteriorhodopsin as part of the proton pump, yet by introducing the mutation, a protein results with a highly extended O-state and enhanced writing efficiency in the branched-photocycle memory architecture.

The thrust of Directed Evolution is to introduce a random mutagenic factor that will produce a number of genetically unique bacteriorhodopsin variants. The one with the most desirable properties can then be used as a parent to produce another round of genetically-engineered progeny. The new strains are then screened for whatever target property is of interest, and the process can start all over again with the best candidate. Key to any successful implementation of directed evolution is the ability to screen for selected properties. For simple properties such as thermal stability or enzymatic activity, the screening process is trivial. For a complex transition such as the generation of P & Q, screening becomes considerably more difficult. In conjunction with experimental *in vivo* screening techniques, directed evolution is currently being used to hone in on highly customized mutants for memory applications. Although we have yet to find a mutant optimized enough to result in a commercially competitive memory device, some of the results detailed below show promise. It must be noted, however, that the results reflect a mixture of both SDM and Directed Evolution techniques, as the latter effort is still in its infancy and will not demonstrate its full potential for at least a year. The reader is referred to report no. AFRL-IF-RS-TR-2001-279 for detail on making mutations in bacteriorhodopsin.

#### **3.1.1.9. Characterization of the Q-state in Wild Type Bacteriorhodopsin**

One of the foremost conclusions of this research effort is that wild-type bacteriorhodopsin is not commercially viable as the active element of the branched-photocycle volumetric optical memory. Although the protein is fully capable of operation as a memory element in three dimensions, low efficiencies result in prolonged

writing cycles. For this reason it is necessary to fully understand the nature of the branched photocycle and the P & Q-states.

To date, the branched photocycle has only been discussed in two publications external to those from the W.M. Keck Center of Molecular Electronics at Syracuse University; Andreas Popp, *et al.* first described the branched photocycle in 1993 [1], and more recently, researchers in Hungary obtained results by continuous illumination of BR gels (gels similar to those produced for the branched photocycle memory) that could be interpreted in terms of the P and Q states [22, 23]. In an effort to reproduce the latter results, spectra containing a yellow photoproduct were obtained by irradiating a polyacrylamide gel of bacteriorhodopsin with light at a wavelength greater than 620 nm at a pH of 8.0 and a temperature of 35 to 40°C. The maximum absorbance of this yellow species was found, via spectral analysis, to be 394 nm. This yellow species could be fully regenerated with an ultraviolet lamp at 365 nm (ambient conditions) to render a species that was spectrally equivalent to native bacteriorhodopsin. This is directly comparable to the results obtained by Dancsházy [22, 23].

The report shown below has recently been submitted to the Journal of Physical Chemistry (as of June 2002), and is expected to be published (in the form shown below) with the title: **Characterization of the branched-photocycle intermediates P and Q of bacteriorhodopsin**, authored by: Nathan B. Gillespie<sup>#</sup>, Kevin J. Wise<sup>#</sup>, Jeffrey A. Stuart<sup>†</sup>, Duane L. Marcy<sup>†</sup>, Qun Li<sup>†</sup>, Lavoisier Ramos<sup>#</sup>, Kevin Jordan<sup>#</sup>, Lei Ren<sup>#</sup>, Sean Fyvie<sup>#</sup> and Robert R. Birge<sup>##</sup>

### 3.1.1.9.1. Abstract

The bacteriorhodopsin branched-photocycle intermediates **P** and **Q** are studied with respect to chromophore isomeric content, photochemical origin, kinetic heterogeneity, and photoreversibility. These blue-shifted species are compared and contrasted to products with similar spectroscopic properties generated *via* thermal denaturation. In contrast to some published studies, we conclude that the thermal and photochemical species differ in both isomeric content and protein environment. Sequential two-photon activation of glycerol suspensions of bacteriorhodopsin containing low concentrations of water (<15% V/V water/glycerol) form high yields of **P** state. This observation is attributed to the role that water plays in the hydrolysis reaction that converts the **P** state to **Q**. Relatively large photo-stationary state populations of both intermediates can be generated in both 85% V/V glycerol suspensions and polyacrylamide gels. At ambient temperature, both intermediates can be fully converted back to **bR** with blue light. Chromophore extraction and HPLC analysis reveal that **P**, **Q**, and the spectrally similar thermal products contain predominantly the 9-*cis* retinal chromophore. The thermal products are also found to contain small amounts of the 7-*cis* isomer. Time-resolved spectroscopy reveals that the **P** state is actually comprised of two components with maximum absorptivities at 445 and 525 nm. The molar absorptivities of the chromophore band maxima of the **P** and **Q** states in an 85% V/V glycerol/water suspension at pH 7 are  $\epsilon(\mathbf{P}_{445}) = 47,000 \text{ M}^{-1}\text{cm}^{-1}$ ,  $\epsilon(\mathbf{P}_{525}) = 39,000 \text{ M}^{-1}\text{cm}^{-1}$ , and  $\epsilon(\mathbf{Q}) = 33,000 \text{ M}^{-1}\text{cm}^{-1}$ . Our kinetic analyses support previous studies indicating that the **P** state

is formed predominantly from the **O** state, which is consistent with the branched-photocycle model. However, other paths to the **P** state are possible, including direct excitation of the small population of blue membrane present in solution. We examine the possibility that the branched-photocycle evolved as a photochromic sunscreen for UVA and UVB protection during times of high sun intensity.

### 3.1.1.9.2. Introduction

Bacteriorhodopsin is the primary light-transducing protein in the purple membrane of the archae *Halobacterium salinarum* (a.k.a *Halobacterium halobium* or *Halobacterium salinarium*). Archae are informally called *archaeobacteria*, but they are not bacteria. Based on physiology, the archae are organized into three types: methanogens (prokaryotes that produce methane); extreme halophiles (prokaryotes that live at very high concentrations of salt); and extreme (hyper) thermophiles (prokaryotes that live at high temperatures). In addition to the unifying archaeal features that distinguish them from bacteria (e.g. no murein in the cell wall, ester-linked membrane lipids), these prokaryotes exhibit unique biochemical attributes as well as complex structural properties which adapt the organisms to their extreme habitats. *H. salinarum* is an extreme halophile that lives in natural environments such as the Dead Sea, the Great Salt Lake, or salt flats where the salt concentration is above that found in the oceans (as high as 5 molar or 25 percent NaCl). *H. salinarum* requires salt for growth and for cell wall, ribosome, and enzyme stability. *H. salinarum* adapts to the low oxygen content inherent in a hot, salt marsh environment by growing the purple membrane and using photosynthetic energy production. Bacteriorhodopsin, the protein in the purple membrane, converts light into a proton gradient which is subsequently used to synthesize ATP. This process is the only example in nature of non-photosynthetic photophosphorylation. But *H. salinarum* is a heterotroph that preferentially respire by

aerobic means, and does not rely on the purple membrane for energy when the concentration of oxygen is sufficient to sustain respiration. This capability is important from a bioengineering standpoint, because it allows genetic manipulation of the protein to produce useful materials that are inefficient or inactive proton pumps. This observation may also provide a perspective on the potential biological relevance of this branching reaction, which we will examine at the end of this article.

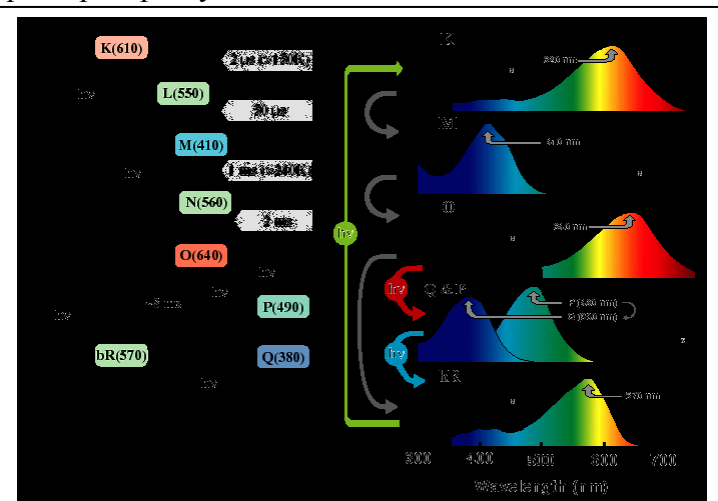


**Figure 3.6:** (a, left) Schematic representation of the BR photocycle. (b, right) Photocycle intermediate absorption spectra, including that of the branched photocycle intermediates P & Q. The retinal chromophore configuration at each stage is also indicated.

The proton pumping process of bacteriorhodopsin is initiated when the protein-bound chromophore of the light-adapted form, the all-*trans* retinal Schiff base, absorbs light and undergoes the photocycle schematically shown in Fig. 3.6. Although many aspects of the proton pumping mechanism remain to be discovered, much has been learned about the molecular details during the past few years [24]. The primary photochemical event involves an all-*trans* to 13-*cis* photoisomerization, and the first trappable intermediate is **K**. The proton pumping mechanism is facilitated through a series of dark reactions which form, in succession, the **L**, **M**, **N** and **O** intermediates (see Fig. 3.6). The isomerization of the chromophore creates an electrostatic environment that destabilizes the protonated Schiff base, resulting in deprotonation of the chromophore and protonation of the nearby Asp-85 residue. This process generates the **M** state, which is blue shifted because the chromophore is now unprotonated. Subsequent dark reactions transfer the proton from Asp-85 down to the Glu-194 and Glu-204 region, and the chromophore is reprotonated through donation of a proton from Asp-96. The branching-reaction that is the subject of this study is also shown in Fig. 3.6. The branch involves photoactivation of the **O** state by red light, which induces all-*trans*  $\rightarrow$  9-*cis* photochemistry [1]. However, the 9-*cis* chromophore is not stable in the binding site, and hydrolysis of the Schiff base takes place to produce 9-*cis* retinal [1]. The latter unbound chromophore is constrained to the binding site region, because the kinked 9-*cis* geometry can neither enter nor exit the binding site. The result is formation of the **Q** state ( $\lambda_{\text{max}} \approx 390$  nm), which is a highly-stable species with a barrier of  $\sim 190$  kJ mol<sup>-1</sup> to thermal reformation of the bR state [25].

As the functional element of two-dimensional memory applications, BR can operate at the diffraction limit while providing high cyclicity, efficiency, and sensitivity. Light-adapted BR (**bR**) and the blue shifted **M** state provide a bistable set with excellent spectral and refractive properties for real-time holography [10, 26]. But the use of the **M** state as a binary component in long-term holographic storage is hindered by the inability to find a chemically or mutagenically modified protein with a long-lived **M** state at ambient temperature. One option is to use blue-membrane-like or D85N-based variants [27-29], but no solution to the poor cyclicity of these systems has yet been found. An attractive alternative is provided by the long-lived **Q** state, which has a lifetime of 7 – 12 years at ambient temperature. This state is blue shifted relative to the **M** state, and hence provides enhanced refractive and diffractive properties, in addition to an extended lifetime. More recently, the fact that the **Q** state is generated *via* a sequential two-photon process has allowed the development of paged three-dimensional memories [25]. Despite their potential importance in bioelectronics devices, relatively little is known about the properties of the **P** and **Q** states. The present investigation was initiated to provide a better understanding of the photochemical origin and stability of these states, and to probe the effect of solvent environment on their properties.

Popp *et al.* were the first to report the formation of the **P** and **Q** states [1]. These investigators carried out sophisticated holographic studies to demonstrate that these states originated *via* photochemical activation of the **O** state. The **P** and **Q** states were shown to contain 9-*cis* retinal chromophores, and to be photochemically reversible back to **bR** with blue light [1]. The studies reported here confirm their principal conclusions,

although we provide evidence that the **P** state is actually a mixture of two species in dynamic equilibrium. More recently, Dancshazy and coworkers have reinvestigated the long-lived blue states of bacteriorhodopsin, using both photochemistry and thermal stress to initiate the reaction(s) [22, 23]. A key conclusion of these recent studies is that formation of the photochemical and thermal states results in partial denaturation of the protein. We demonstrate here that under the appropriate conditions, these blue-shifted states can be fully reverted to **bR** without imposing any permanent change in the protein.

Although the principal impetus for initiating these studies was the importance of these blue-shifted states to the development of photonic devices based on BR, a better understanding of the origin and properties of these states has fundamental importance. Nature has optimized the binding sites of the retinal-based light-transducing proteins to provide highly efficient bond-specific photochemistry. The rhodopsins and the cone pigments of the vertebrate and invertebrate photoreceptors are optimized by evolution to select for and enhance the efficiency of the 11-*cis* to 11-*trans* photochemical process [30, 31]. Bacteriorhodopsin has been optimized to select for and enhance the efficiency of the all-*trans* to 13-*cis* photochemical process [32, 33]. It remains to be explained why the independent evolutionary enhancement of these systems has converged on quantum efficiencies of  $\sim 0.65$ . Does this quantum yield represent some limiting value for bond-specific photochemistry, or are we observing a simple coincidence? Answers to such questions require a more detailed experimental understanding of how the photochemistry of the retinal chromophores is directed by protein-chromophore interactions. Through studies of side reactions, such as the direct and indirect formation of the **P** and **Q** states in bacteriorhodopsin, new insights into the underlying mechanisms of protein-directed photochemistry are possible.

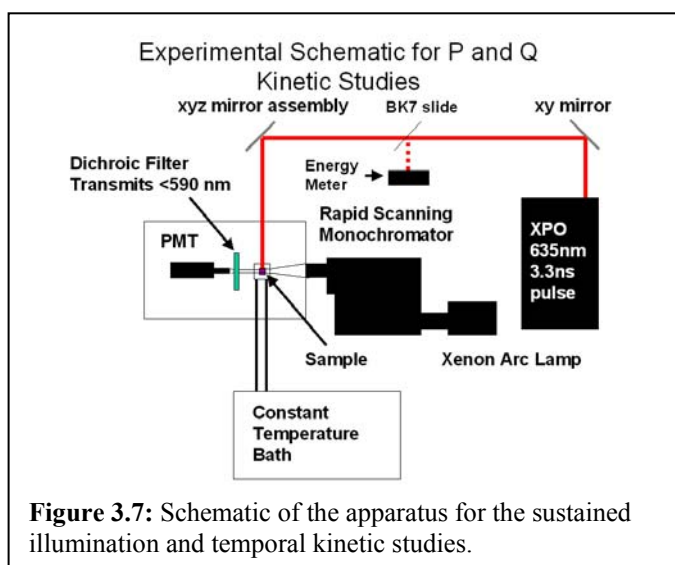
### 3.1.1.9.3. Materials and Methods

Bacteriorhodopsin membrane fractions were purified according to standard procedures [34, 35]. In experiments designed to explore the effect of water concentration, purple membrane (PM) suspensions were prepared with low water content in glycerol (85%, 90%, and >95% glycerol, or 15%, 10%, <5% water by volume) in polymethacrylate semi-micro cuvettes (Fischer #14-385-938). PM pellets produced *via* low pressure centrifugation (Eppendorf vacufuge, 240xg at <20 mbar vacuum, 30°C) were mixed with the appropriate glycerol/water solution, followed by sonication at 20 kHz (Heat Systems Cell Disrupter Model W-225 R) to remove aggregates. Mixtures were then irradiated at 647 nm ( $1.8 \text{ W/cm}^2$ , 6 mm diameter beam) from a Coherent Innova 300 krypton ion gas laser for a total of 45 min. The samples were subsequently homogenized prior to analysis by UV-visible spectroscopy (Cary 50 UV-VIS Spectrometer).

Steady-state and time-resolved kinetic experiments were performed on 85% V/V glycerol to water purple membrane suspensions (1.2 OD per 1 mm path, pH 7, 0.05M phosphate buffer,  $22 \pm 1^\circ\text{C}$ ) in a 1 mm path length quartz flow cuvette (Starna Cells, 73.1F) sealed with parafilm. Steady-state spectra were taken on a Cary 50 UV-visible spectrometer (Varian, inc.) following exposure to red light from a 50 W mercury-xenon

arc lamp passed through a  $647 \pm 40$  nm band pass filter ( $30 \pm 3$  mW/cm<sup>2</sup>) (Melles Griot #03FIV048). Light adaptation and partial regeneration was accomplished *via* exposure to  $550 \pm 20$  nm ( $10 \pm 2$  mW/cm<sup>2</sup>) (Melles Griot #03FIV044) light from the same lamp. Full regeneration was attained with a  $400 \pm 20$  nm ( $10 \pm 2$  mW/cm<sup>2</sup>) (Melles Griot #03FIV026) band pass filter. The average intensity from the lamp was measured by a wavelength and intensity calibrated power meter (Coherent LM-2 interfaced with a Coherent Labmaster Ultima data acquisition unit). Analogous experiments were performed on purple membrane fractions immobilized in a 10% cross-linked polyacrylamide matrix buffered in 50 mM phosphate at pH 8 in 1 cm methacrylate<sup>2</sup> cuvettes. Immobilized purple membrane suspensions were exposed to  $\sim 100$  mW/cm<sup>2</sup> from a 50 W mercury-xenon arc lamp with a glass cutoff filter ( $\lambda > 620$  nm) at 40°C, followed by exposure to a long wave UV lamp centered at 365 nm (UVP, Inc. UVL-14). Spectra were taken of the resulting  $\sim 1$ cm<sup>2</sup> photoconverted volume (i.e., yellow photoproduct) with a diode array UV visible spectrometer (HP 8453).

In the time-resolved experiments, samples at 40°C were exposed to 635 nm, 3.3 ns pulse-width emission from an optical parametric oscillator (OPO) pumped by the third harmonic of a Nd:YAG system (Coherent Infinity-XPO). The energy of each pulse was measured by a calibrated energy meter (Ophir PE50-BB interfaced to an Ophir Laserstar acquisition unit). A rapid scanning monochromator (RSM) system (OLIS instruments, Inc. RSM-1000 stopped flow) observed the spectrum (360-590nm) of these samples orthogonal to the incident beam, while a constant temperature bath maintained the temperature of the samples within 1°C (Julabo F30-C, modified by OLIS instruments, Inc.). To screen out the intense 635 nm emission from the OPO, a dichroic filter (CVI Laser, Inc. CP-SC-590-1.00) was placed in front of the sample photomultiplier in the RSM system. A schematic of the time-resolved apparatus is illustrated in Figure 3.7. A reference spectrum was taken just prior to exposure in each experiment, and the subsequent difference spectrum was monitored by the RSM system, with 1000 scans averaged each second.



The chromophore-analysis studies were performed in a dim red light environment using the method of P. Scherrer *et al* [36]. Using a vortex mixer, 100  $\mu$ l of each sample was agitated for 1 min with 250  $\mu$ l of ice-cold ethanol in a centrifuge tube. 500  $\mu$ l of hexane was then added, followed by two minutes of agitation and subsequent centrifugation for 1 min. The resulting organic layer was transferred to a sample vial with a Pasteur pipette, and immediately

analyzed by HPLC (Waters 600E multisolvent delivery system with a Water 2487 dual

wavelength detector) in a method adapted from recent work by G. Noll and C. Becker [37]. Two Prep Nova-Pak HR Silica columns (3.9 x300 mm Waters, Milford, MA, USA) in series provided the stationary phase. The mobile phase, flowing at 1.5 ml/min, was composed of 93% hexane and 7% tert-methyl-butyl-ether (TBME). Thermal denaturation studies were carried out on 85% V/V glycerol suspensions of purple membrane in a 100  $\mu$ l quartz cuvette (Starna cells 16.100F-Q-10). An electronically controlled, water cooled, Peltier driven sample holder (Varian # 00 10074 00) maintained the temperature, while the spectra were sampled with a Cary 50 UV-visible spectrometer. Samples were equilibrated for 10 minutes at the specified temperature prior to collecting the spectra.

#### 3.1.1.9.4. Results and Discussion

The experiments and observations discussed below will provide evidence that the **P** state is actually comprised of two components with maximum absorptivities at 445 and 525 nm. However, under most experimental conditions, only a single species is observed with an absorption maximum at 440 to 450 nm (mostly **P**<sub>445</sub> with small amounts of **Q** likely present) or 490 nm (roughly equal mixtures of **P**<sub>445</sub> and **P**<sub>525</sub>). To be consistent with the literature, we will refer to such mixtures as the **P** state when differentiation into the **P**<sub>445</sub> and **P**<sub>525</sub> components is either not possible or was not attempted. The extraction experiments carried out in this study, and described below, indicate that both **P**<sub>445</sub> and **P**<sub>525</sub> have 9-*cis* retinal chromophores. The absorption spectra and previous studies of the blue membrane provide strong evidence that both **P**<sub>445</sub> and **P**<sub>525</sub> have protonated Schiff base chromophores [1, 29, 38-41]. We will speculate on the molecular differences of these two species below.

We will also provide additional evidence for the model proposed by Popp *et al* [1], that the **Q** state is comprised of 9-*cis* retinal constrained to remain somewhere inside the chromophore binding site. It is thus likely that there are many forms of the **Q** state characterized by different locations and orientations of the free chromophore inside the binding site. While multiple forms of the **Q** state are likely, under no experimental circumstances were we able to differentiate multiple forms. Upon excitation with blue light, the 9-*cis* retinal chromophore isomerizes to all-*trans* and recombines rapidly with lysine-216 to form **bR**. This process involves at least one intermediate, which we will label  $\Theta$ , which would be characterized by all-*trans* retinal not covalently bound to the protein. Studies are underway to characterize the nature of this short-lived  $\Theta$  species, which is normally not shown in diagrams (e.g. Fig. 3.6).

##### 3.1.1.9.4.1. Hydration Experiments in Glycerol

A sample of bacteriorhodopsin suspended in 85% (V/V) glycerol was illuminated at 647 nm for 45 minutes (Figs. 3.8a-b). The illumination initially generates a rise at 445 nm due to the formation of the **P** state, which is evident when the contribution from light-adapted BR is subtracted. The sample was then left in the dark for 15 hours, resulting in a 390 nm absorbing species, attributed to the **Q** state. These observations provide evidence that the **P** state is a precursor to the **Q** state, and that **P** can thermally transform



to **Q** following access of the branched photocycle upon irradiation of the **O** state. Note that no significant regeneration of **bR** (560-570 nm) from the **P** state can be seen following 15 hours in the dark, so the protein does not thermally regenerate from the **P** state in this environment.

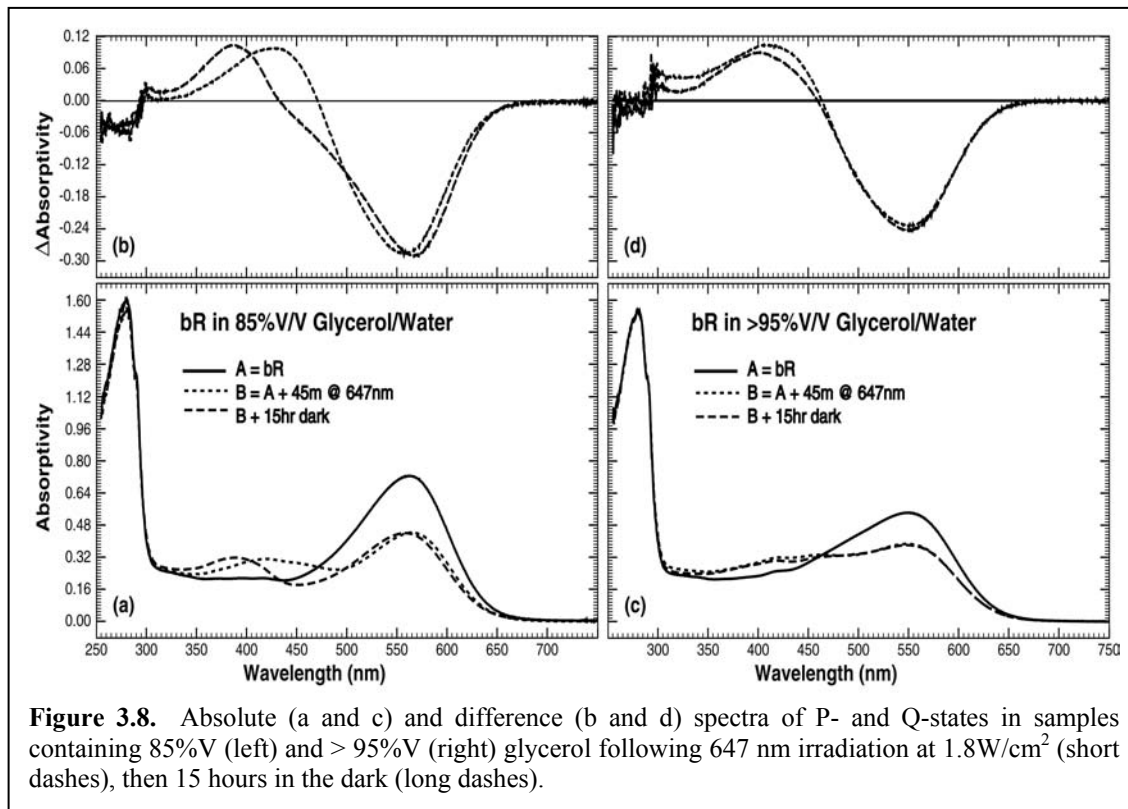


**Figure 3.8.** Absolute (a and c) and difference (b and d) spectra of P- and Q-states in samples containing 85%V (left) and > 95%V (right) glycerol following 647 nm irradiation at  $1.8\text{W}/\text{cm}^2$  (short dashes), then 15 hours in the dark (long dashes).

The **Q** state is thermally produced from **P** as a result of hydrolysis of the Schiff-base linkage binding the retinal chromophore to the protein. Therefore, if all water were removed from the sample, no transition from **P** to **Q** would be expected. A sample of bacteriorhodopsin suspended in >95% glycerol was tested under conditions identical to those described above (Figs. 3.8 c-d), and showed no blue shift over time. Furthermore, no significant changes were observed after 15 hours in the dark, consistent with the interpretation that water was not present in amounts conducive for the hydrolysis reaction to proceed, thus trapping BR in the **P** state, or at least severely inhibiting the **P**  $\rightarrow$  **Q** transition.

#### 3.1.1.9.4.2. Regeneration of the P and Q states

**P** and **Q** state generation/regeneration experiments were performed on bacteriorhodopsin in both 85% (V/V) glycerol suspensions, and polyacrylamide gels. The results of these experiments are shown in Fig. 3.9. In Fig. 3.9a, an 85% glycerol/water suspension of **bR** was successively illuminated with red, green, and violet light at ambient conditions ( $22 \pm 1^\circ\text{C}$ ). Illumination in the green ( $550 \pm 20$  nm) resulted in full regeneration of **bR** from the **P** state, but no significant regeneration from the **Q** state (Fig. 3.9a), indicating that **Q** does not absorb substantially in this spectral region.

However, violet light ( $400 \pm 20$  nm) regenerated **bR** from both **P** and **Q**. Full recovery of the protein is evident not only from the complete return of the 568 nm peak in this spectrum, but the 280 nm peak as well. A polyacrylamide-suspended sample was illuminated for 4 hours with a cutoff filter ( $>620$  nm) at  $40^\circ\text{C}$  to obtain the first spectrum shown in Fig. 3.9c.

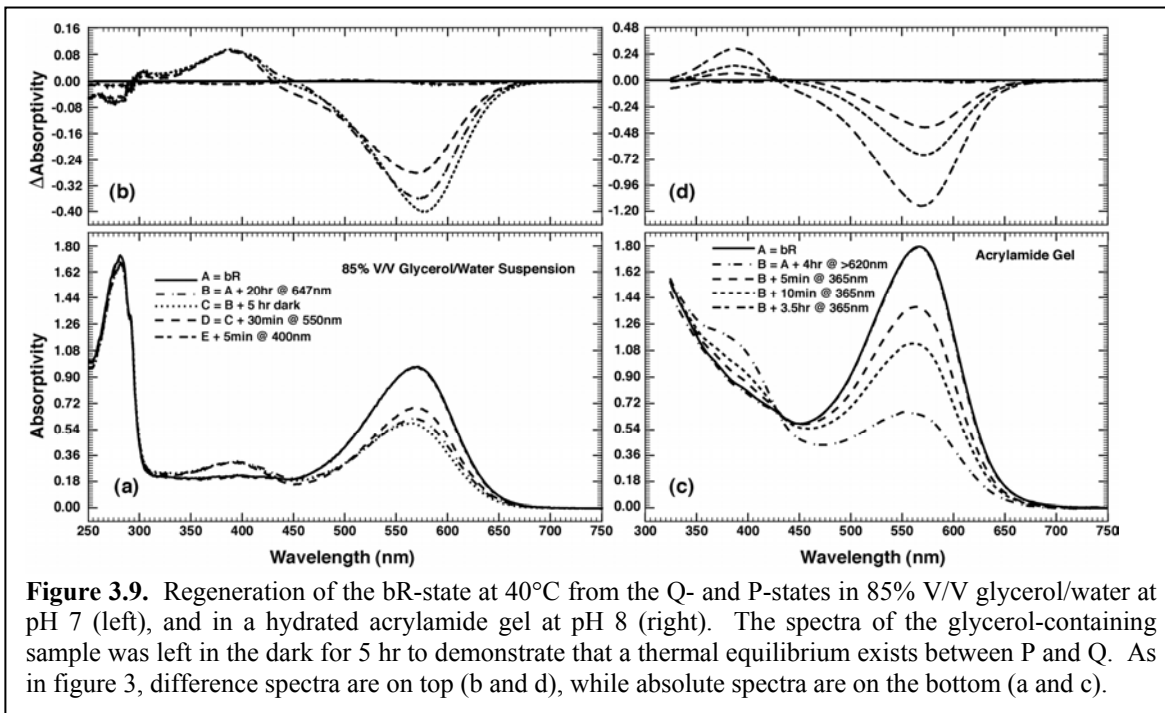


**Figure 3.9.** Regeneration of the **bR**-state at  $40^\circ\text{C}$  from the **Q**- and **P**-states in 85% V/V glycerol/water at pH 7 (left), and in a hydrated acrylamide gel at pH 8 (right). The spectra of the glycerol-containing sample was left in the dark for 5 hr to demonstrate that a thermal equilibrium exists between **P** and **Q**. As in figure 3, difference spectra are on top (b and d), while absolute spectra are on the bottom (a and c).

The unshifting isosbestic point at 430 nm in this spectrum is a clear indication that **bR** and **Q** are the dominant species in this sample, while the **P** state persists in much smaller quantities in the polyacrylamide matrix. This observation is good evidence that gels produced with a high water content are more similar to an aqueous suspension than a glycerol suspension of purple membrane, because they do not inhibit Schiff base hydrolysis. Approximately 50% regeneration occurs after only 5 minutes illumination with UV light centered at 365 nm. Illumination with UV light for 3.5 hours results in 100% regeneration of the chromophore peak from the 390 nm absorbing species. The difference spectra in Figs. 3.9b and 3.9d shows that the **Q** state ( $\lambda_{\text{max}} \sim 380$  nm) can be fully converted back to **bR** via UV irradiation in both sample preparations. This observation is in contrast to the recent work by Dancshazy that shows only partial regeneration after 30 minutes of illumination with blue light [22]. Although the latter data were collected with the sample at  $60^\circ\text{C}$ , the authors state that there is little difference between the  $60^\circ\text{C}$  data and data collected at  $20^\circ\text{C}$ .

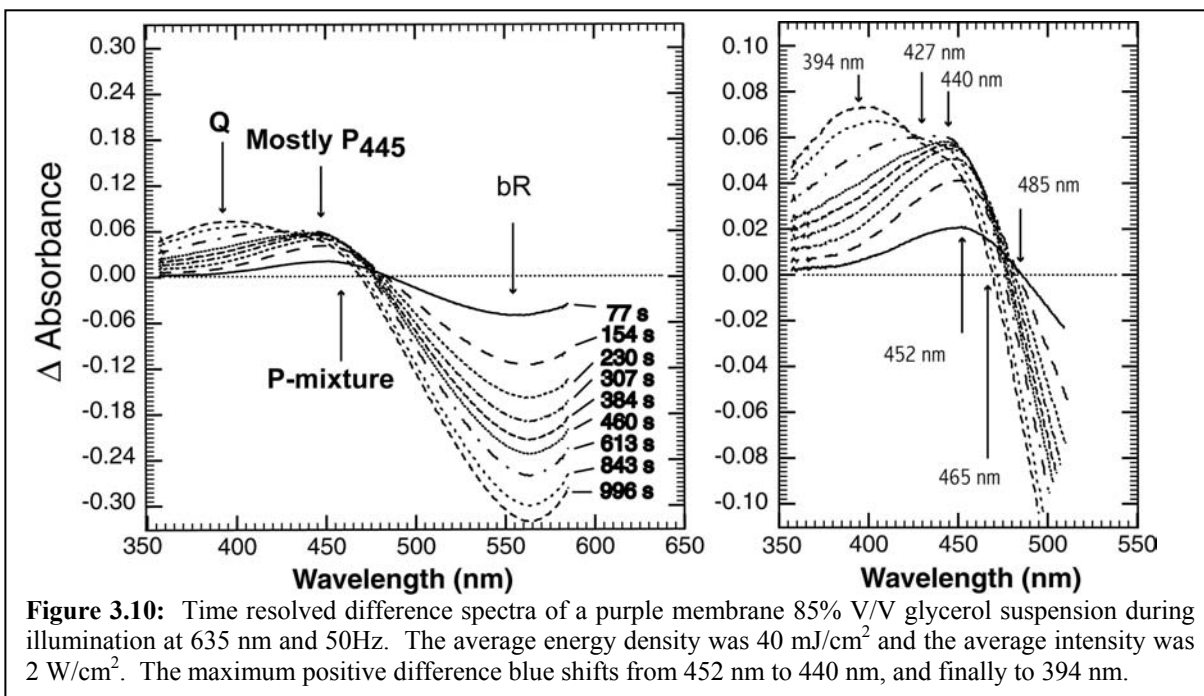
The elevated temperature (40 vs.  $\sim 22^\circ\text{C}$ ) and higher intensity (100 vs.  $30 \text{ mW/cm}^2$ ) required to achieve similar conversion of **bR** to **Q** in an aqueous gel are an indication that the net quantum yield of **P** state formation is lower and more temperature sensitive in a polyacrylamide gel than in a hydration-limited glycerol suspension. At room temperature ( $22 \pm 1^\circ\text{C}$ ), negligible conversion of **bR** to **Q** is found to result from

exposing **bR** to illumination of  $\lambda > 620$  nm in polyacrylamide, with the same intensity ( $100 \text{ mW/cm}^2$ ) and time span (5 hours).

The **Q** and **P** state spectra in Fig. 3.9, generated after 20 hours of exposure at 647 nm, can be interpreted as the result of an equilibrium condition. This interpretation is supported by the lack of a substantial blue-shift in the spectrum after 5 hours in the dark, and by the fact that the 380 peak in the difference spectrum is unchanged following partial regeneration of the **bR** state upon exposure to 550nm light for 30 minutes. Because **P** is thermodynamically more favorable when water is removed, much more is present in equilibrium with **Q**. This results in a higher concentration of **P** in a photostationary state with **bR** and its photocycle intermediates.

### 3.1.1.9.4.3. Sustained Illumination Experiments and Calculated Spectra

Figure 3.10 presents a set of time-resolved difference spectra obtained at a temperature of  $40^\circ\text{C}$  with steady state pulsed illumination at a rep-rate of 50 Hz and a wavelength of 635 nm. The sample was equilibrated at  $40^\circ\text{C}$  for at least 15 minutes to minimize any thermal changes in the spectrum. The sample was then illuminated for 30 seconds to ensure that the fast photointermediates (**M**, **O**, etc.) had reached photostationary state—thus, the reference spectrum in these difference spectra is the photostationary state of **bR** and its fast photointermediates. The first isosbestic point in these spectra shifts from 485 nm to 465 nm, indicating that the **P** state is a two-species mixture. The initial spectrum (maximum difference at 460 nm) has virtually the same isosbestic point (485 nm) that Popp, *et al.* observed for **P** state in thin films (483 nm) [1]. Under these conditions, however, the maximum quickly blue-shifts to 440 nm, then, more slowly, to 394 nm. A second isosbestic point forms at 427 nm after 613 seconds, indicating that the red-absorbing form of the **P** state found in the earlier spectra has all but disappeared.



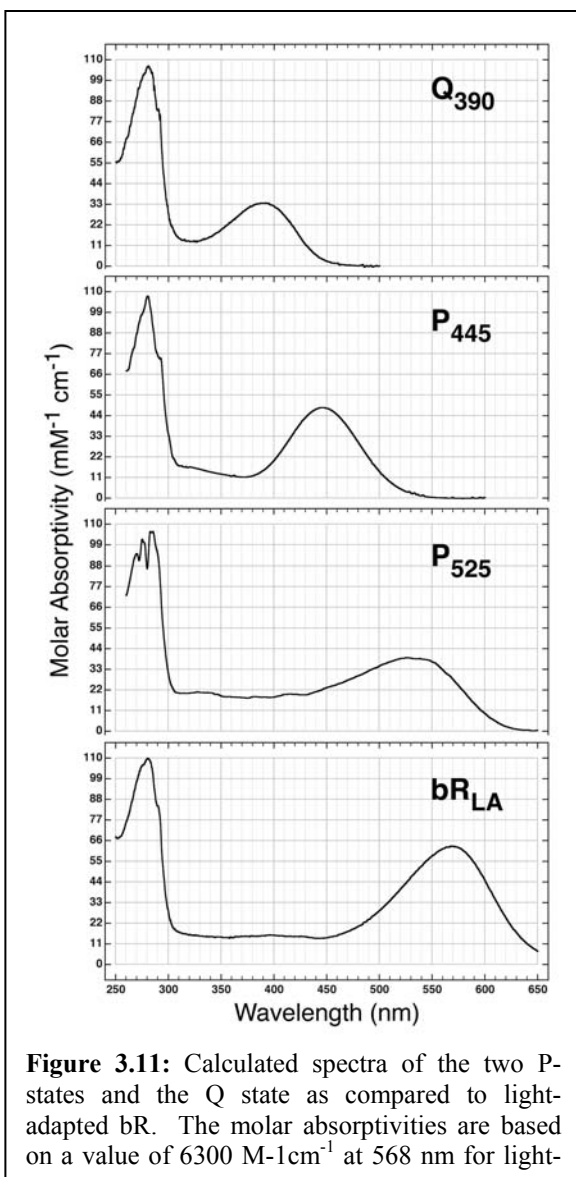


**Figure 3.11:** Calculated spectra of the two P-states and the Q state as compared to light-adapted bR. The molar absorptivities are based on a value of 6300 M<sup>-1</sup>cm<sup>-1</sup> at 568 nm for light-

Further steady state spectroscopic investigations of **P** and **Q** in an 85% glycerol suspension at pH 7 rendered the calculated spectra of the pure species shown in Fig. 3.11, which were calculated *via* the removal of light- and dark-adapted **bR** from several sets of steady state regeneration spectra like those shown in Fig. 3.8, followed by smoothing. These spectra show the best agreement with the available qualitative photokinetic evidence, and the relevant extinction coefficients are tabulated below (Table 1). The **Q** state spectrum is also in good agreement with those presented in the literature [1, 22, 23].

The **P** state saturates to a photostationary state when exposed to red light at  $647 \pm 40$  nm, indicating that this state has some absorbance in this region. As indicated in the time-resolved study above, the **P** state in this system is believed to be comprised of two components. Deconvolution of the spectra from two different regeneration experiments led to the results shown in Fig. 3.11. The long-wavelength state, **P**<sub>525</sub>, ( $\lambda_{\text{max}} = 525$  nm), is believed to be the primary branching photoproduct and appears to be quite unstable and inhomogeneous. We speculate that the inhomogeneity is associated with a variety of protein conformations

unfavorable to the 9-*cis* photoproduct. This inhomogeneous set of protein-chromophore interactions will destabilize the ground state and generate a red-shifted absorption band relative to the second **P** state. The **P**<sub>525</sub> state thermally rearranges quickly to form **P**<sub>445</sub> ( $\lambda_{\text{max}} = 445$  nm), which is considerably more homogeneous and stable when the glycerol

State <sup>(a)</sup>	$\epsilon$ @280 nm (M <sup>-1</sup> cm <sup>-1</sup> )	$\lambda_{\text{max}}$ (nm)	$\epsilon$ (M <sup>-1</sup> cm <sup>-1</sup> )
<b>bR</b>	110,000	568	63,000
<b>P</b> <sub>445</sub>	109,000	445	47,000
<b>P</b> <sub>525</sub>	108,000	525	39,000
<b>Q</b>	106,000	390	33,000

Table 1: Summary of calculated molar extinction coefficients P- and Q- state species. [based on an extinction coefficient of 63,000 M<sup>-1</sup>cm<sup>-1</sup> at 568 nm for **bR**. **bR** = light-adapted bacteriorhodopsin]

content of the sample is high, and the water content of the sample is low (<15% by volume). This two state model can explain why the electronic spectrum of the predominant component reported here,  $P_{445}$ , is blue-shifted from those of the forms previously reported (445 vs. 490 nm [1, 23]). The most plausible explanation for this observation is that the thin film and acrylamide environments of these previous studies favor the second species,  $P_{525}$ , more than a glycerol suspension does.

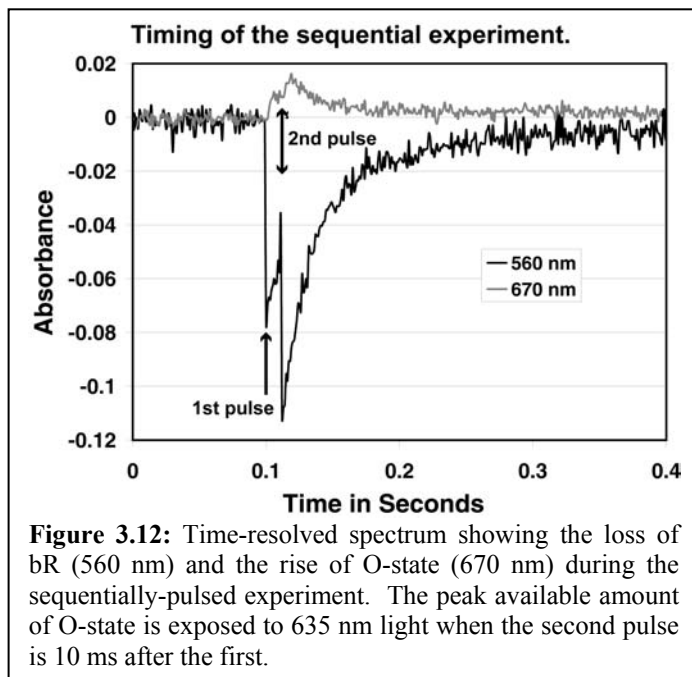


Figure 3.12 shows the results of two temporal kinetic experiments on an 85% (V/V) glycerol suspension of purple membrane at 40°C. In the first case, the sample was exposed to two 635nm, 70 mJ cm<sup>-2</sup> laser pulses of 3 ns duration with temporal separation of one second. Our time resolved spectral data indicated that more than 99.9% of the resting state was populated after one second. In the second case, two 635 nm pulses of less than half the energy density (30 mJ/cm<sup>2</sup>) were incident on the sample with a delay of 0.99 second between each set of two pulses, and a delay of 10 ms between pulse pairs. Thus, the second pulse of the pair intercepts a large accumulation of the **O** state (fig. 3.12). The resulting difference spectrum was deconvoluted assuming a 3 species kinetic model containing the previously calculated spectra of **bR**,  $P_{445}$  and **Q** for these conditions. The relative amounts of  $P_{525}$  and the fast-decaying **K** through **O** intermediates are assumed not to make any significant contribution because of the elevated temperature (which increased all reaction rates), the long delay between exposures and spectra (~1 sec), and the large number of spectra averaged (1000). As can

Of particular interest in these spectra is the significant change in the intensity of the 280 nm peak associated with the aromatic residues in the protein. The experimental studies of Popp, *et al.* [1], and later studies on the similar pink membrane [29], have indicated that the 13-methyl group of the 9-*cis* chromophore in the **P** state interacts with the aromatic residues in the binding site. This interaction is likely to be responsible for the formation of **Q** from the **P** state, because the steric strain of 9-*cis* retinal in the **P** state is high enough to favor a

#### 3.1.1.9.4.4. Temporal Kinetic Studies and a New **P** State Model

Figure 3.12 shows the results of two temporal kinetic experiments on an 85% (V/V) glycerol suspension of purple membrane at 40°C. In the first case, the sample was exposed to two 635nm, 70 mJ cm<sup>-2</sup> laser pulses of 3 ns duration with temporal separation of one second. Our time resolved spectral data indicated that more than 99.9% of the resting state was populated after one second. In the second case, two 635 nm pulses of less than half the energy density (30 mJ/cm<sup>2</sup>) were incident on the sample with a delay of 0.99 second between each set of two pulses, and a delay of 10 ms between pulse pairs. Thus, the second pulse of the pair intercepts a large accumulation of the **O** state (fig. 3.12). The resulting difference spectrum was deconvoluted assuming a 3 species kinetic model containing the previously calculated spectra of **bR**,  $P_{445}$  and **Q** for these conditions. The relative amounts of  $P_{525}$  and the fast-decaying **K** through **O** intermediates are assumed not to make any significant contribution because of the elevated temperature (which increased all reaction rates), the long delay between exposures and spectra (~1 sec), and the large number of spectra averaged (1000). As can

be seen from Fig. 3.13, the initial rate of **P** formation,  $k_P$  (assuming a linear rate constant at high concentrations of **bR**), is more than 8 times faster when the second pulse illuminates a significant concentration of photocycle intermediates ( $k_P=0.093$  mM/(Einstein/cm<sup>2</sup>)), than when **bR** is sole species being irradiated ( $k_P=0.012$  mM/(Einstein/cm<sup>2</sup>)). This result is consistent with the holographic studies performed by Popp, *et al.* [1], which indicated a strongly-favored reaction pathway branching from a red-absorbing intermediate of the standard BR photocycle, specifically the **O** state.

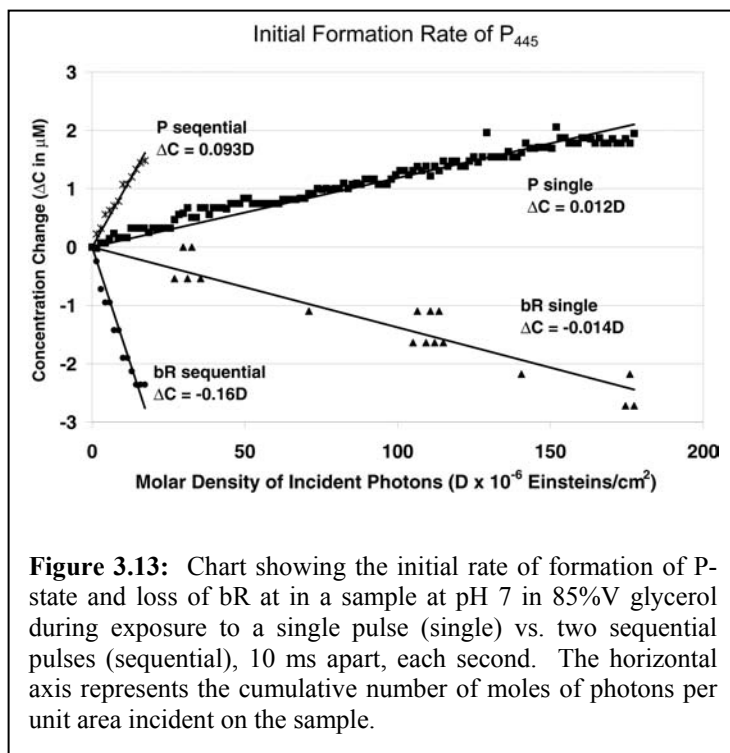


**Figure 3.13:** Chart showing the initial rate of formation of P-state and loss of **bR** at in a sample at pH 7 in 85%V glycerol during exposure to a single pulse (single) vs. two sequential pulses (sequential), 10 ms apart, each second. The horizontal axis represents the cumulative number of moles of photons per unit area incident on the sample.

suspensions exposed to a similar peak power density (~1 MW/cm<sup>2</sup>) at 532 nm [45]. The literature [45, 46] often refers to this high peak power induced denatured form as pseudo-**bR** ( $\lambda_{\max}=370$  nm), and it is invariably accompanied by light-induced blue membrane (LIBM). It is possible that photoexcitation of LIBM will produce a P-like state in the same fashion as photoexcitation of blue membrane produces the pink membrane.

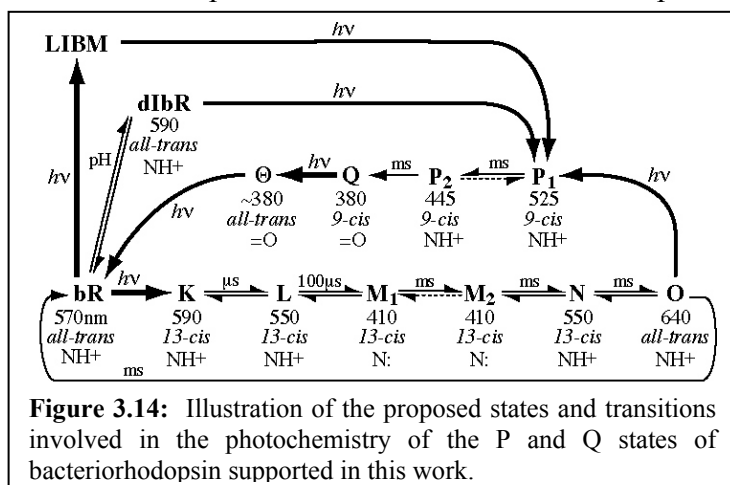


**Figure 3.14:** Illustration of the proposed states and transitions involved in the photochemistry of the P and Q states of bacteriorhodopsin supported in this work.

One plausible explanation for the significant amount of **P** and **Q** state formed in the single pulse experiment (Fig. 3.13) is the existence of a small quantity of blue membrane in the sample, which, when exposed to intense red light, has been shown by many groups to form pink membrane, a species spectrally very similar to **P** [29, 41-44]. A small amount of denaturation could also be occurring in this experiment as a result of the high peak power of the OPO system (~20 MW/cm<sup>2</sup>). Such an effect has been shown to occur in purple membrane

The above experiments lead to a model for the P state which suggests that this species actually consists of two components, **P<sub>525</sub>** & **P<sub>445</sub>** (Fig. 3.14). Photoactivation of the **O** state generates **P<sub>525</sub>** and provides the dominant pathway for the formation of **P** (and

subsequently **Q**). There are two alternative paths that can also photochemically generate **P**, and these involve direct photochemical activation of either **dlbR** or **LIBM**. While our experiments showed no evidence of **LIBM** formation, it is nearly impossible to eliminate the presence of small amounts of blue membrane (see discussion in [47]). The **Q** state is believed to form upon the hydrolysis of the retinal Schiff base bond in  $P_{445}$ . Both of these proposed species are evident in the time-resolved data presented in Fig. 3.10. The two forms of the **P** state proposed here appear to be quite analogous to the two forms of pink membrane discussed in other studies ( $dlbR_{485}$  and  $dlbR_{455}$ , 485 nm and 455 nm  $\lambda_{max}$ , respectively). Tallent, *et al.* proposed that the  $dlbR_{485} \rightarrow dlbR_{455}$  transition is the result of the deprotonation of a nearby residue; an analogous process may be responsible for the  $P_{525} \rightarrow P_{445}$  transition [29]. But the larger shift in wavelength may indicate a more drastic change in the protein environment coupled with relaxation of the chromophore.

#### 3.1.1.9.4.5. Thermal denaturation experiments and chromophore analysis

Figure 3.15 shows several spectra of BR in 85% glycerol before, during, and after being heated to 70°C. This temperature was carefully chosen to avoid excessive damage to the protein, as has been demonstrated in other studies done at higher temperatures [48, 49]. Purple membrane suspensions heated as high as 60°C have been shown to contain only 13-*cis* and all-*trans* chromophores [36]. In the first experiment, the sample was left to regenerate for 24 hours, but unlike previous work on the first thermally-generated state [36, 48], the sample did not completely recover its original spectrum immediately after cooling. This was believed to be

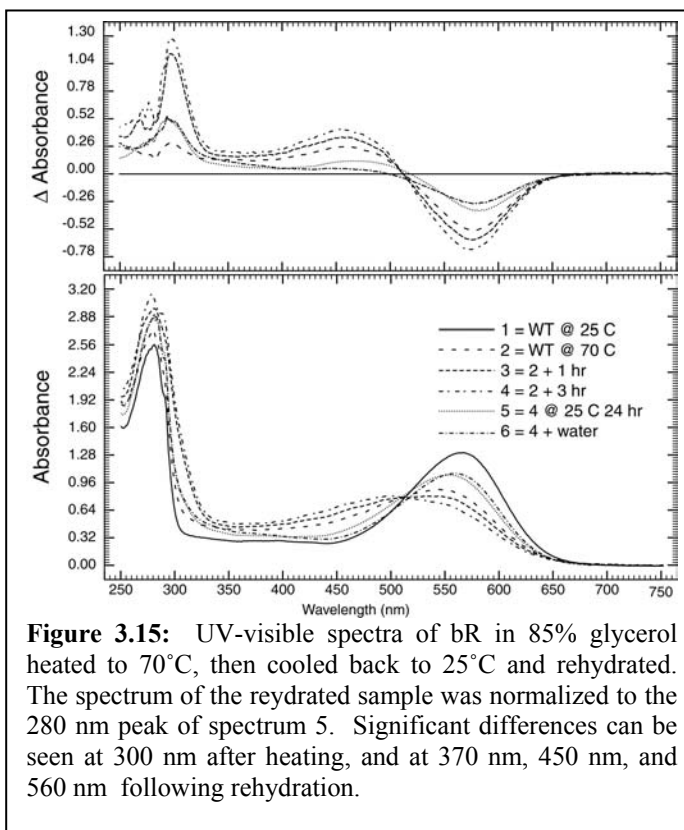


**Figure 3.15:** UV-visible spectra of bR in 85% glycerol heated to 70°C, then cooled back to 25°C and rehydrated. The spectrum of the rehydrated sample was normalized to the 280 nm peak of spectrum 5. Significant differences can be seen at 300 nm after heating, and at 370 nm, 450 nm, and 560 nm following rehydration.

the result of dehydration, because the micro-cuvette containing the sample, while sealed, had a large open air pocket into which water could evaporate. In the second experiment, therefore, water was added following cooling. The consequent spectrum showed a loss in the 460 nm product, with an increase in the unbound (340-400 nm) and bound (500-600 nm) chromophore regions. This indicates that, similar to the photochemical **P** state, two states comprise the 460 nm product. The irreversible rise at 300 nm is characteristic of thermally-denatured protein [48] and indicates that the thermal denaturation products are less stable than the spectrally similar **P**- and **Q**- states. Additionally, the kinetic behavior of the “Q-like” thermally-denatured state does not resemble that of its photochemical

counterpart, and cannot be driven back to the bR resting state upon exposure to violet light (data not shown). In addition, this state shifts further to the ultraviolet (300 nm) at elevated temperatures.

Table 2 lists the results of the chromophore analysis studies. The mild thermal denaturation products of BR contain a predominately 9-*cis* chromophore (25% and 18%), with a very small fraction of the 7-*cis* isomer (3% and 1%). This result provides good evidence that after 13-*cis*, the 9-*cis* conformation has the next highest energy thermodynamically allowed by the protein, with the 7-*cis* conformation higher yet. A 7-*cis* chromophore, however, does not appear in the extractions of the photochemical products, **P** and **Q**, indicating that the integrity of the protein in these states is much greater than it is for the thermally-induced products. Furthermore, the rehydrated sample shows a marked decrease in the proportion of the 9-*cis* chromophore (18% vs. 25%), providing additional evidence that the “P-like” 460 nm absorbing product is a mixture of two species—one that will return to an all-*trans* or 13-*cis* chromophore-containing species without being exposed to blue light, and another that will irreversibly form the “Q-like” thermal product.

**Table 2:** Chromophore composition of photochemical and thermal species determined *via* chromophore extraction and HPLC. The last two columns indicate the % loss the chromophore peak, while the final column indicates the % deviation of this value from the percentage of 9-*cis* chromophore found in the extractions.

BR State	% trans	all- % cis <sup>(a)</sup>	13- % 9- <i>cis</i>	% 7- <i>cis</i>	%loss at $\lambda_{\max}$	%difference
<b>native</b>	<b>74</b>	<b>26</b>	<b>0</b>	<b>0</b>	<b>0</b>	<b>--</b>
<b>647nm, 30 min "P<sub>446</sub>"</b>	<b>65</b>	<b>27</b>	<b>8</b>	<b>0</b>	<b>11</b>	<b>27</b>
<b>647nm, 18hr "Q"</b>	<b>27</b>	<b>26</b>	<b>47</b>	<b>0</b>	<b>43</b>	<b>-9</b>
<b>70°C, 90 min</b>	<b>52</b>	<b>20</b>	<b>25</b>	<b>3</b>	<b>37</b>	<b>33</b>
<b>70°C, 200 min rehydrated</b>	<b>57</b>	<b>24</b>	<b>18</b>	<b>1</b>	<b>20</b>	<b>12</b>

(a) The presence of 13-*cis* isomer is due largely, if not solely, to dark-adaptation in the samples prior to extraction.

#### 3.1.1.9.4.6. Comparison with Previous Studies

The work of Dancsházy *et al.*, [22, 23] demonstrated that continuous broad band ( $\lambda > 500$  nm) illumination of bacteriorhodopsin results in bleached photoproducts that absorb at 390 nm and 490 nm (after singular value decomposition). They proposed a three state model consisting of a light sensitive state (A) in equilibrium with a primary photoproduct (B), and a presumably thermal product (C) that is photochemically irreversible and produced from the primary photoproduct (B):  $A \leftrightarrow B \rightarrow C$ . “A” was assumed to be the bR resting state, “B” the 490 nm absorbing state, and “C” the 390 nm absorbing state. In the follow-up paper [22], the 390 nm absorbing state was reported to be reversible to the bR resting state upon illumination with blue light. In addition, the



authors note that the photobleached state is stable and might have practical applications; however, their regeneration studies indicated a bR recovery rate of less than 80%, thus imposing a severe limitation on applications that require full write-read-erase capabilities.

As previously discussed, the bacteriorhodopsin branched photocycle was first described by Popp and coworkers in 1993 [1]; the branched photocycle intermediates **P** & **Q** bear a strong similarity to the photobleaching products described by Dancsházy, *et al.* However, the nature of the experimental set-up in the latter work (continuous broadband illumination) did not permit differentiation between linear and branched reaction pathways. These observations prompted our reexamination of the photobleaching phenomenon in bacteriorhodopsin.

The results described herein support some of the theories expressed in previous work [1, 22, 23], while demonstrating that **P** and **Q** are stable and can be driven back to **bR** quantitatively under the appropriate conditions. Evidence for the Schiff base hydrolysis mechanism of **P** → **Q** is presented, along with data confirming that these 9-*cis* states are produced predominantly as a result of branching from the main BR photocycle. There is, however, what appears to be a direct route to the **P** state from **bR** (or species in thermal equilibrium with **bR**), which may be due to a contribution from a small equilibrium concentration of blue membrane; previous studies have shown that the primary photoproduct of dIbR is a 9-*cis* species analogous to **P** and denoted as the pink membrane [29, 41-43, 50]. The **P**-state is also shown to be a mixture of two species (**P**<sub>525</sub> and **P**<sub>445</sub>) that behave much like the two components of pink membrane (**dIbR**<sub>485</sub> and **dIbR**<sub>455</sub>). But as we note below, this comparison must be made with caution, as there are some differences that remain to be explained.

In contrast to previous studies, **bR** was demonstrated to be fully regenerable from the **P** and **Q** states. The reformation of the 280 nm molar absorptivity from the **Q**-state is the most significant result of the regeneration experiments, because it indicates that the protein, including the chromophore binding site, is not permanently modified by conversion of the protein to the **P** and **Q** states. That is, full regeneration of the **bR** resting state can be achieved by exposure to blue light.

The thermal denaturation and chromophore extraction experiments demonstrate that the thermal products of **bR**, while having similar electronic spectra and chromophore compositions, significantly differ from **P** and **Q** in terms of chemical behavior and stability. The major differences include the following: (1) only partial regenerability of **bR** from the “P-like” thermal species upon cooling; (2) the small, but significant, presence of the 7-*cis* chromophore, and (3) the formation of an irreversibly denatured, 300 nm absorbing product from the “Q-like” state upon longer exposure to elevated temperature (70°C). Most important, these thermal products will not fully revert to **bR** upon exposure to UV/violet light.

### 3.1.1.9.5. Comments and Conclusions

Bacteriorhodopsin-based optical memory devices have shown potential for many years [25, 27, 51, 52]. The presence of a branched photocycle reaction enables three-dimensional optical storage, whereby the **P** and **Q** states collectively represent *binary 1* and the **bR** resting state represents *binary 0* [25]. The **Q** state can also be utilized for holographic applications [1]. The ability to completely convert **P** and **Q** back to **bR** comprises the erasure mechanism of both binary photonic and holographic optical storage. The present study indicates that a long-lived **P**-state is undesirable in a volumetric memory, because the **P** state establishes an equilibrium mixture of two components with a long wavelength tail associated with the **P**<sub>525</sub> species. Attempts to read or write data with **P** state present may produce unwanted photochemistry and potential data loss. In contrast, the **Q** state is unaffected by red, yellow and most green (>540 nm) light. Hence, efficient formation of **Q** is critical for information storage. In optimizing the overall rate and magnitude of **bR** to **Q** photoconversion in wild type bacteriorhodopsin, the availability of water must be balanced; a compromise must be reached between the competing factors of the quantum yield of **P**<sub>525</sub> and temperature sensitivity (favored at lower water concentrations), and the formation rate and concentration of **Q** (favored at higher water concentrations). Studies are underway to quantify such an optimal condition. Mutational strategies are now in place to optimize the protein for branched-photocycle data storage based on the wild-type experiments reported here.

The molecular nature of the **P**<sub>525</sub> and **P**<sub>445</sub> states remain to be explored. Although we know that both states have 9-cis protonated Schiff base chromophores, we know little else about the nature of the protein-chromophore interactions. We speculate that **P**<sub>525</sub> is a species characterized by a distorted 9-cis retinal protonated Schiff base chromophore with numerous unfavorable chromophore-protein interactions (e.g. Fig. 12 of Ref. [29]). These interactions destabilize the ground state and lead to a red-shifted species. Protein-relaxation leads to a chromophore that is more stable, and produces the blue-shifted **P**<sub>445</sub> state. But the change in the protein environment responsible for the formation of the **P**<sub>445</sub> state leads to unfavorable protein-protein interactions, and hence the **P**<sub>525</sub> and **P**<sub>445</sub> states are in dynamic equilibrium. Solvent environment, pH and temperature all contribute to establishing the relative steady-state concentrations. While it is interesting to compare these two states with the two components of the pink membrane (**dlbR**<sub>485</sub> and **dlbR**<sub>455</sub>) observed by Tallent et al. [29], caution is necessary. The model proposed for **dlbR**<sub>485</sub> and **dlbR**<sub>455</sub> involves distortion around to 10-11 single bond, and a change in the protonation state of a nearby residue [29]. We have no direct evidence or theoretical models to support a similar mechanism coupling **P**<sub>525</sub> and **P**<sub>445</sub>. Further work on this interesting problem is in progress.

We close by examining whether the branched-photocycle is a biologically advantageous process, or one which negatively impacts the survival of the organism. One can provide a straightforward explanation of why the branched-photocycle might be disadvantageous. In an environment where there is no blue light present, formation of the **Q** state is terminal and clearly harmful because the purple membrane would eventually become a yellow membrane and be an ineffective proton pump. But as can be seen by reference to Fig. 3.16, there is ample solar flux in the 300-420 nm region of the spectrum, not only at the surface and 10 cm below the surface of a simulated salt marsh. Irradiation in this region is potentially harmful to microbes.

There is one aspect of the branching reaction which could impart comparative advantage. Consider the situation where the organism has responded to oxygen stress by making quantitative amounts of the purple membrane and has converted over to photosynthetic energy production. The intensity of sunlight suddenly

increases resulting in a dramatic decrease in the external pH due to light-transduction by the purple membrane. The branching reaction might provide comparative advantage by placing a portion of the BR molecules into the **Q** state. The **Q** state would be stable until the organism rose to or very near the surface where a sufficient intensity of light in the 360 – 400nm region would be available to drive **Q** → **bR** photochemistry. While the above mechanism might confer some comparative advantage to the organism, simulations indicate that after a four hour stretch of intense sunlight, the fraction of protein molecules in the **Q** state would be less than 0.01%. The above analysis suggests that the branched photocycle reaction is not relevant to the biological function of the purple membrane. The next question to address is whether evolution has optimized the protein so that the probability of branching is below the above threshold. Such a question is cannot be answered with confidence, but we note that 85% of the random mutants that we have studied yield a higher yield of **Q** state under steady state illumination. It is thus likely that natural selection has indeed minimized the branch photocycle. We have found some variants of the protein that provide a two-orders-of-magnitude increase in the photochemical branching reaction. The use of directed evolution to optimize this reaction is in progress.

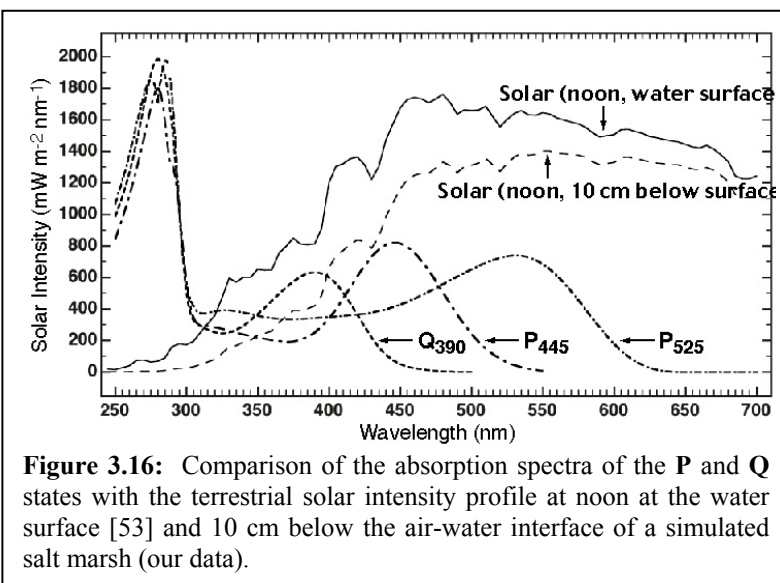


**Figure 3.16:** Comparison of the absorption spectra of the **P** and **Q** states with the terrestrial solar intensity profile at noon at the water surface [53] and 10 cm below the air-water interface of a simulated salt marsh (our data).

**Acknowledgements.** Support for this research was provided by the United States Air Force, (F30602-99-1-0555), the National Institutes of Health (GM-34548), the National Science Foundation (EIA-0129731) and the Army Research Office (MURI: DAAD 19-

99-1-0198). We thank Profs. N. Hampp and R. Needleman for interesting and helpful discussions.

#### **3.1.1.10. Further Characterization of the Branched Photocycle**

The work described above represents the primary effort made in-house to examine and characterize the bacteriorhodopsin branched photocycle. However, the study was basic in nature and further characterization with respect to the behavior of the protein under conditions relevant to routine memory operations was also required. The work described below details that effort.

##### **3.1.1.10.1. Results from Screening Systems**

The screening systems have been described in previous reports. This section will summarize the results obtained from the operation of these systems. The data includes a temperature study for wild-type protein under otherwise standard testing conditions. The effect of pH and salt concentration modifications from the standard gel formulation for wild-type protein were also tested. In addition, a comparison at otherwise identical conditions between the wild-type protein and several of the mutant strains is reported.

##### **3.1.1.10.2. Description of the Standard Experiment (Exposure Curve)**

The key measurement required for the operation of the three-dimensional memory is the integral of the O-state. This measurement is derived from a time-resolved spectral response at a single wavelength and is intended to quantify the amount of protein that under-goes a standard BR photocycle due to laser pulse excitation. The measurement is a standard flash photolysis, or pump-probe experiment that is common in photochemistry. By orienting the pump and probe beams orthogonally and choosing a probe wavelength that is transparent to BR but absorbed by a photo-induced state, the experiment interrogates only the amount of protein reacting to the pump beam at the intersection of the beams. In these experiments, the protein is interrogated at only one location in the volumetric medium, as defined by the intersection of two laser beams. In other words, it can be used to quantify a property of the protein at one specific location in three dimensions.

The screening apparatus has been designed to probe a wavelength associated with the O-state of the BR photocycle. Upon excitation from the pump beam bacteriorhodopsin initiates its photocycle, and as it goes through the O-state, a small drop in the probe beam intensity is detected and amplified. The signal is then digitized and integrated. The resulting number represents the integral of the O-state and is recorded. A proper calibration would provide the information in absorbance units-seconds. However, as all experiments are carried out in either of two screening units, a relative comparison among different cubes tested in the same system is made. A time-resolved trace for a measurement is shown in figure 3.17 below.

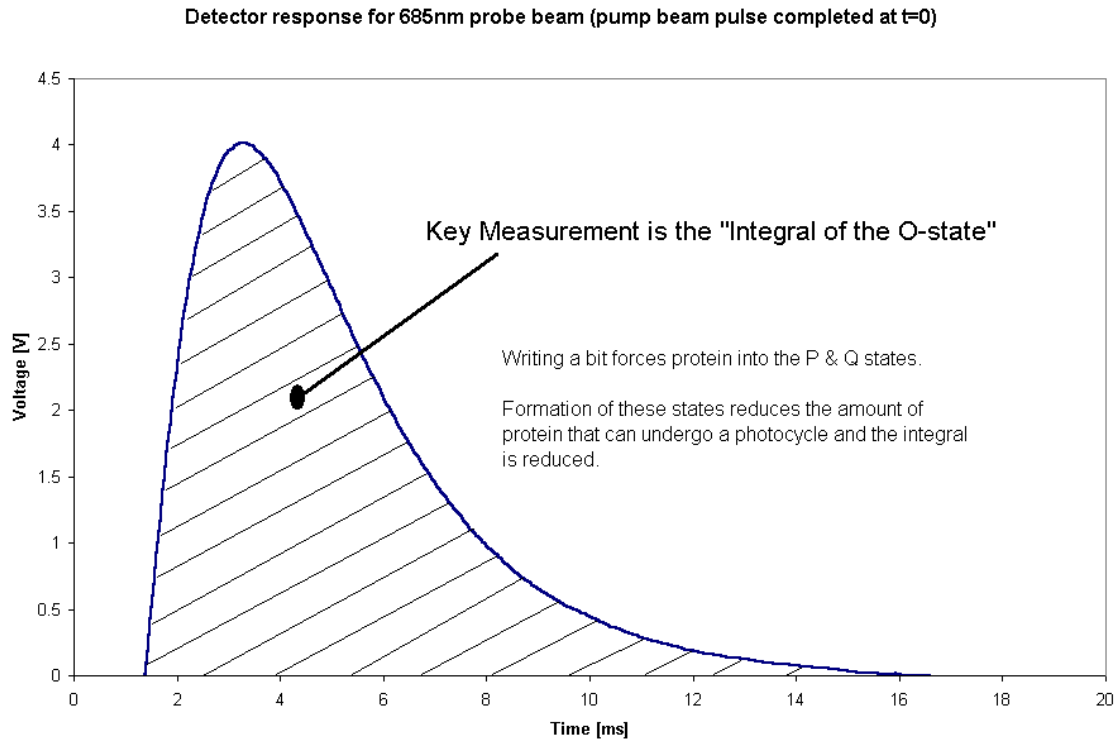


**Figure 3.17:** Measurement of the O-state at 685 nm.

The measurement described above is the key measurement required for the three-dimensional memory. However, useful memory architectures must write as well as read. Therefore, the complete standard experiment referred to as the exposure curve, is not just a measurement of the integral of the O-state, but must be a complete read, write, and erase process. Writing occurs in the three-dimensional memory by exposing the protein to sequential flashes of the pump followed by the probe beams. In the write process the probe beam is used as a second pump and not as a probe. The screening apparatus differentiates the probe beam used for reading and the second pump used for writing by placing a filter in the light path to dim the probe intensity by a factor of 300 during a read cycle.

The writing process is three-dimensional (photochemistry occurs only at the intersection of the two beams, which can be located anywhere in the matrix) because the bR protein has a branched photocycle. The first pump beam illuminates bR and causes the protein to initiate the photocycle. When the maximum amount of bR is in the O-state, the second pump beam is triggered. This beam is transparent to bR and therefore is only absorbed by protein converted to the O-state by the first pump beam. A branched photochemical conversion from the O-state to the P-state makes the three-dimensional memory possible.

The P-state quickly decays thermally to the Q-state, which is permanent. The P and Q-states collectively are defined as a binary one, according to the architecture defined in the introduction. There are two important features of the P and Q-states, which make the three-dimensional memory architecture possible. First, both states are

transparent to the probe beam used during a read just as the BR protein. This means that the determination of the O-state signal is not disturbed by the presence of written bR material. The second important feature is that the P and Q-states disable the regular photocycle. Therefore, the O-state integral is reduced as bR is driven into the Q-state. If a write cycle is performed (pump beam followed sequentially by a second pump beam), followed by a read cycle, the magnitude of the O-state integral will be reduced. Write-read sequences can be sequentially repeated causing continued reduction of the O-state integral. Figure 3.18 below shows such an experiment performed in the screening apparatus.

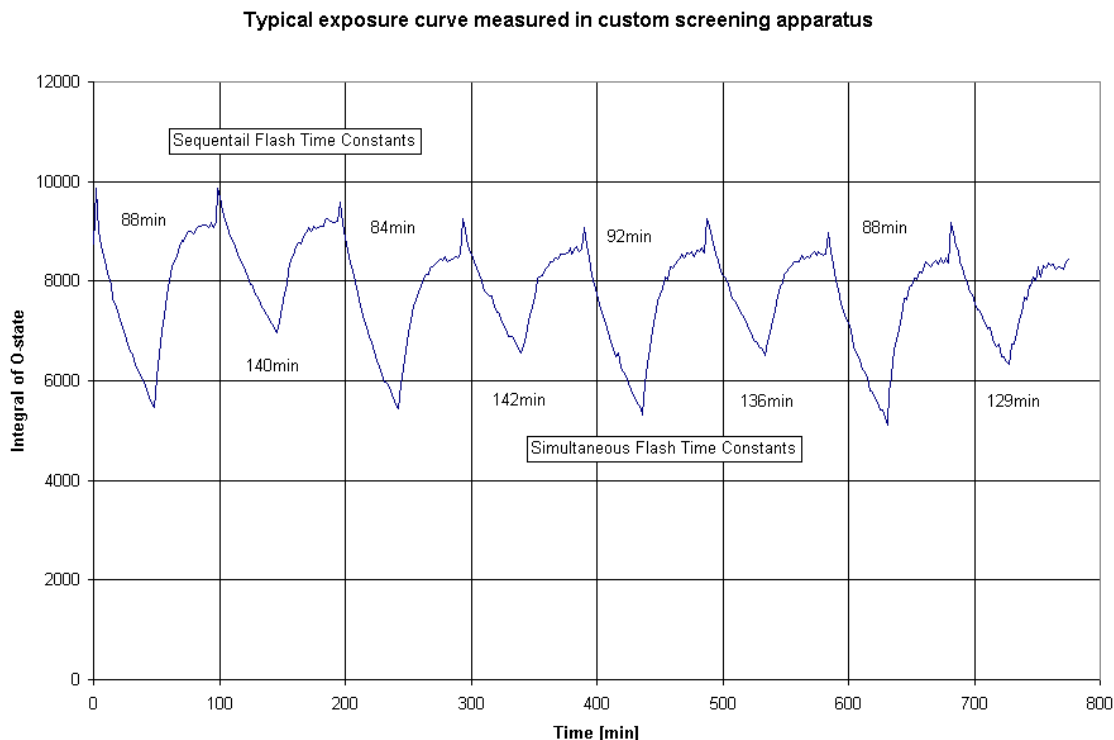


**Figure 3.18:** Typical saw-tooth pattern seen in screening experiments.

It can be seen that after  $t=0$ , the O-state integral is reduced in a manner that approximately follows a first order photochemical reaction. Therefore, a time constant associated with the exponential decay of the O-state signal with increased writing time is determined. This time constant is labeled the sequential-flash time constant. Note that figure 3.18 also illustrates a second time constant, denoted as the simultaneous-flash time constant. Time periods in which the O-state integral increases are also indicated. Each of these features will be described in the following paragraphs.

The simultaneous-flash time constant is measured to insure branched photochemistry. As mentioned previously, a branched photochemical process is required for writing in three dimensions because it provides a three-state system; a binary system is not capable of three-dimensional memory storage (with the exception of two-photon processes), because while attempting to photoconvert a binary one to a binary zero (or visa-versa) in a volumetric matrix, all of the other binary ones along the axis of

illumination will be similarly transformed. However, the observation of a first order photochemical reaction at one location in a bR cuvette (the sequential flash experiment by itself) does not prove that the photochemistry is branched. Of course writing one location and then reading several locations around that spatial point could be used as a test to verify that only one particular location was written. This experiment however, would require 3D positioning of the cuvette, greatly complicating the screening apparatus.

An indirect test of branched photochemistry can be made by varying the timing of the two probe beam pulses, as a method to confirm the original architecture. If the second probe beam is timed such that no O-state is present due to the first probe beam, no writing should occur. This can be accomplished quite easily by flashing both probe beams simultaneously. Therefore, under illumination by simultaneous probe beam flashes, writing should proceed at a slower rate than the sequentially-flashed scenario. Note that in Figure 3.18 this result is quite evident. Ideally there should be no photochemistry at all in the latter case—the fact that there is can be attributed to the fact that long pulse widths for the low power diode lasers used in the experiments allowed for overlap of O-state from subsequent photocycles, i.e., the pulse length was long enough to catch the initial formation of the O-state, and therefore drive a very small amount of the protein into the branched photocycle.

The key feature of comparing the results from the sequentially-flashed probe beams versus the simultaneously flashed probe beams is that the same exact numbers of photons irradiate the region of interest in both cases. Only the relative timing between the firing of the two probe beams is changed, yet the photochemical reaction occurs at a different rate.

Finally, the portions of the saw-tooth pattern illustrated in Figure 3.18, in which the O-state integral rises, is simply an erase step. Under illumination with blue light energy, the P and Q-states are returned back to photoactive BR. The screening apparatus has four blue LED's at 435nm that can illuminate the volume under test. The LED's are not used especially to characterize the erase process, but to return the BR protein to a functional state so that a series experiments can be carried out on a test sample under complete computer control (as illustrated).

The standard experiment therefore, is write-read-write-read-etc. process in which a time constant for the rate of formation of the P and Q-states is measured. An erasure and a repeat of the write-read-write-read-etc. process follows, except that the pump pulses are fired simultaneously. A larger time constant for this second experiment verifies the existence of the branched photocycle, a requirement for the three-dimensional memory architecture. The results reported below are all based on measurements from this standard experimental procedure.

### 3.1.1.10.3. Temperature Dependence of the Formation of the P and Q-states

A standard procedure for producing a gelled cuvette of BR protein was selected for these studies. The conditions of this standard cuvette were determined to maximize the O-state signal from the protein, a property that is extremely sensitive to environmental conditions. The actual formulation is proprietary. A cuvette made with wild-type protein under the standard conditions is used as a baseline experiment (or a calibration) from which the relative performance of new chemical or biologically modified formulations can be measured.

The screening system was designed with a constant temperature control for performing the standard exposure curve experiment. The temperature data consists of a time constant for both sequential and simultaneous flash experiments measured at different temperatures. A rate constant for the process is determined by calculating the reciprocal of the time constant.

The figure below shows results from the standard exposure curve performed on the standard cuvette at different temperatures. As is evident, up to about 42 degrees C, the process follows a typical Arrhenius relationship. The activation energy for the formation of the P and Q-states in this apparatus under the standard conditions was determined to be 42 kcal/mol, meaning that for every 8 degrees C rise in temperature an order of magnitude increase in the rate of formation of the P and Q-states is observed. From this result, it was decided that the standard measurement temperature for further experiments would be 40C, and all results that follow are taken at 40C.

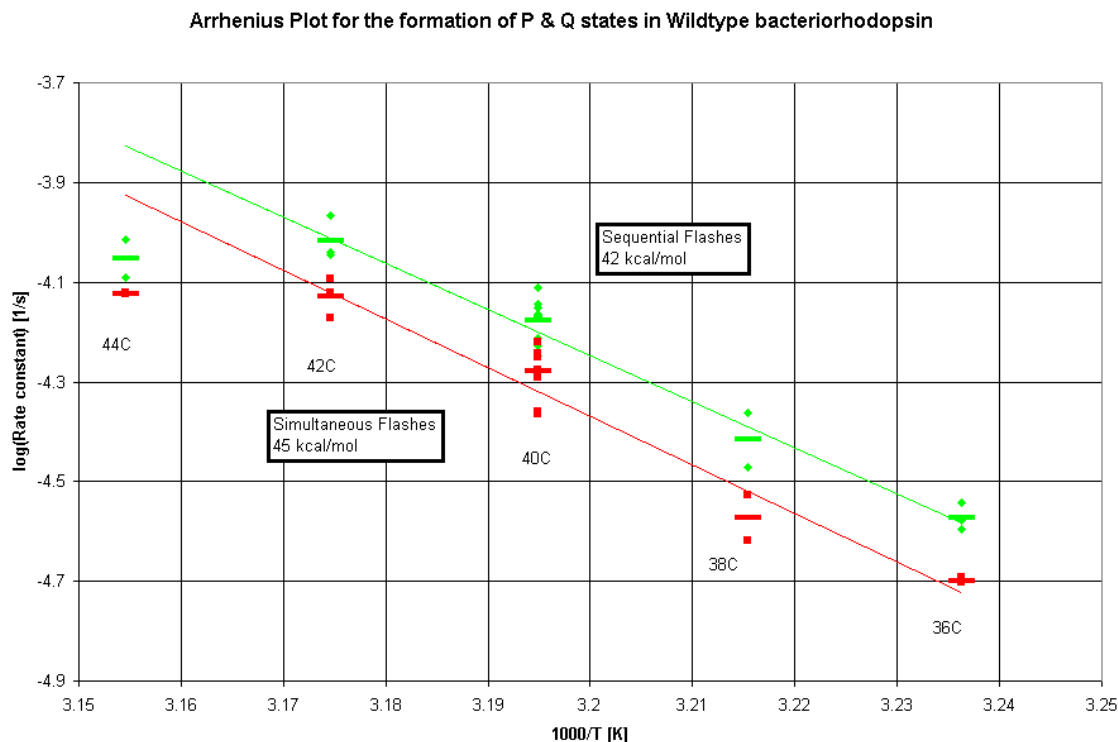


**Figure 3.19:** Arrhenius plot for the formation of P & Q in wild-type bacteriorhodopsin.



Note that the data taken at 44°C does not follow the same Arrhenius relationship. At this temperature problems with the stability of the cuvette and memory medium (gel) are observed, namely, melting of the plastic cuvette material itself and an observation of boiling over of the ingredients inside the cuvette. Therefore, it is important not to jump to the conclusion that the deviation of the data from the Arrhenius relation is an inherent property of the BR protein. In the following figures (3.20-3.24), the effects of pH, temperature, ionic strength, and various mutations on the branched photocycle are illustrated. The effect of pH is particularly interesting. At low pH, where accumulation of the O-state is favored, formation of the P & Q states is inhibited. Another interesting phenomenon at lower pH is seen in the erasing process, where the integral of the O state actually decreases, contrary to what is intuitively expected. The origins of this effect are not yet clear. At neutral to high pH, the trends are as expected. At ultrahigh pH formation of both P & Q are strongly enhanced, but as evident in Figure 3.22 the signal quickly fades, presumably to protein denaturation. The ionic strength dependence was explored to determine if the blue membrane photocycle made any contribution to unwanted photochemistry. Tallent, *et al.*, verified that the blue membrane photocycle behaves analogously to the branched photocycle—blue membrane can be viewed as an approximation of the O-state, and its photoproducts appear to be analogous to P & Q. Because blue membrane formation is equilibrium based (as a function of cation concentration), it stands to reason that there will be a small equilibrium concentration present at all times. Even if that amount is 2% or less, the contribution to unwanted photochemistry could be problematic. The rationale for examining the ionic dependence of branched photocycle formation therefore is obvious—increasing the cation concentration should have the effect of decreasing the amount of blue membrane present, thereby making the memory writing process more efficient. Unfortunately, the trends of both the sequential and simultaneous flashed experiments are for the most part parallel, and do not immediately support the hypothesis as described above. This phenomenon remains under investigation.

The case made for genetic engineering is demonstrated adroitly in Figure 3.24, where O-state integrals and the associated time-constants for access of the branched photocycle for a series of mutants are presented. The power of genetic engineering to alter the nature of the photocycle to the advantage of device applications is obvious. Clearly substantial improvement is evident in the comparison between some of the mutants and the wild-type protein, with respect to both signal intensity and time constant (indicating branched photocycle efficiency). This group of mutants is based on intelligent design, where the known roles of various amino acid residues in bacteriorhodopsin photocycle were used as the basis for generating the mutants. Unfortunately the method is limited by the lack of full understanding of the specifics of bacteriorhodopsin function on an individual amino acid basis, and such broad issues as protein folding. Directed evolution provides a brute-force approach that can circumvent this limitation through generation of mutants that would otherwise be overlooked. The newest BR variants produced as a function of directed evolution are currently being evaluated under conditions relevant to the branched-photocycle memory architecture.

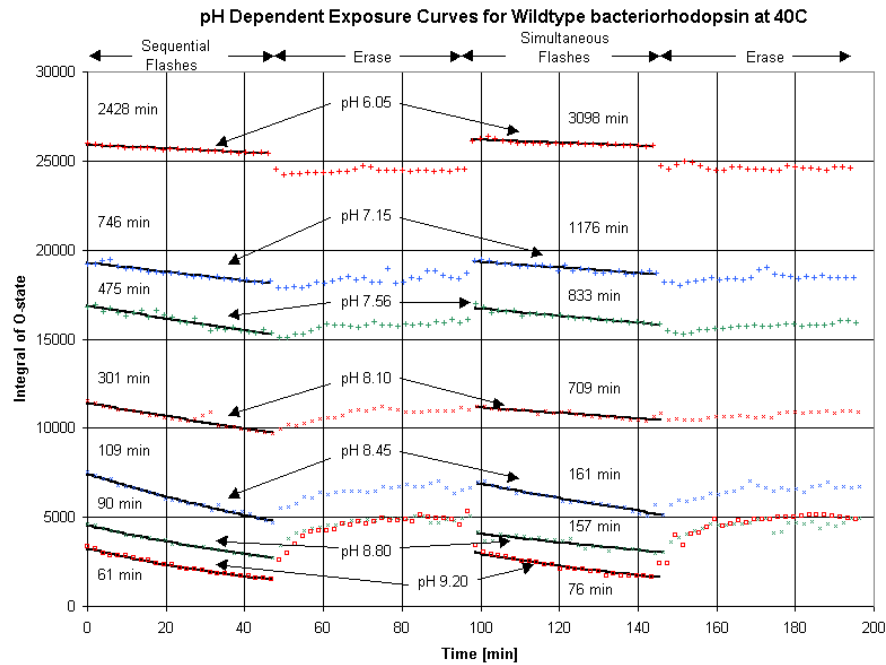


**Figure 3.20:** pH dependence of O-state formation in wild type bacteriorhodopsin at 40°C

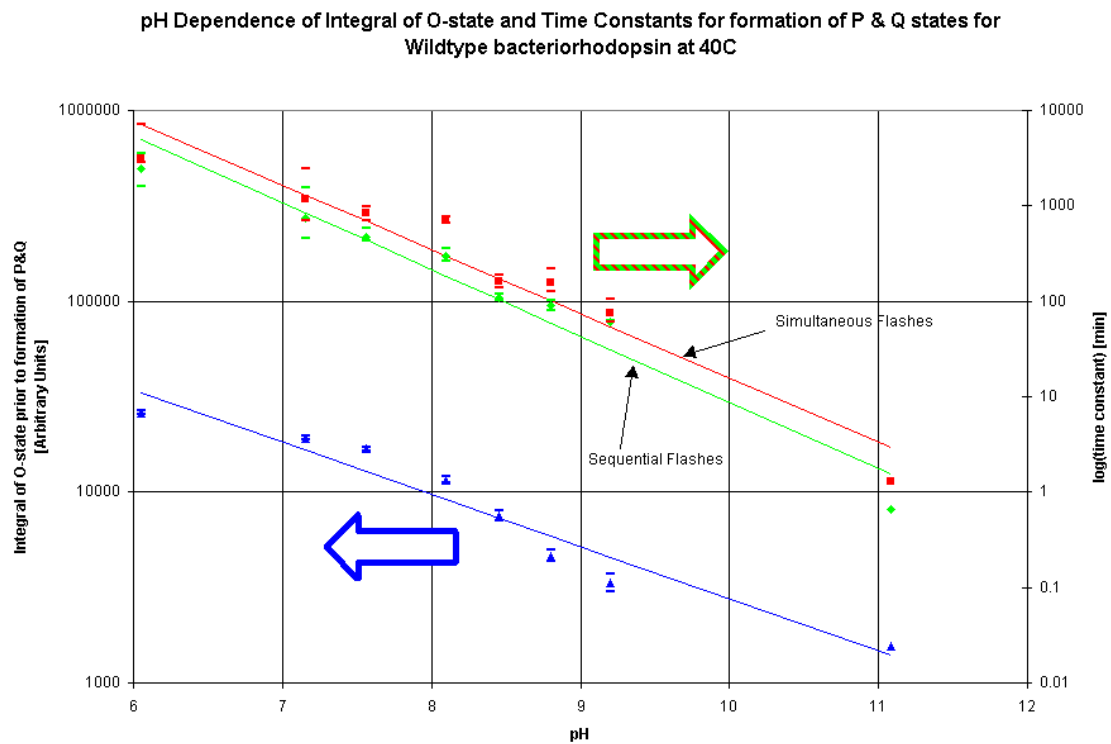


**Figure 3.21:** O-state integral and log(time constant) plotted as a function of pH

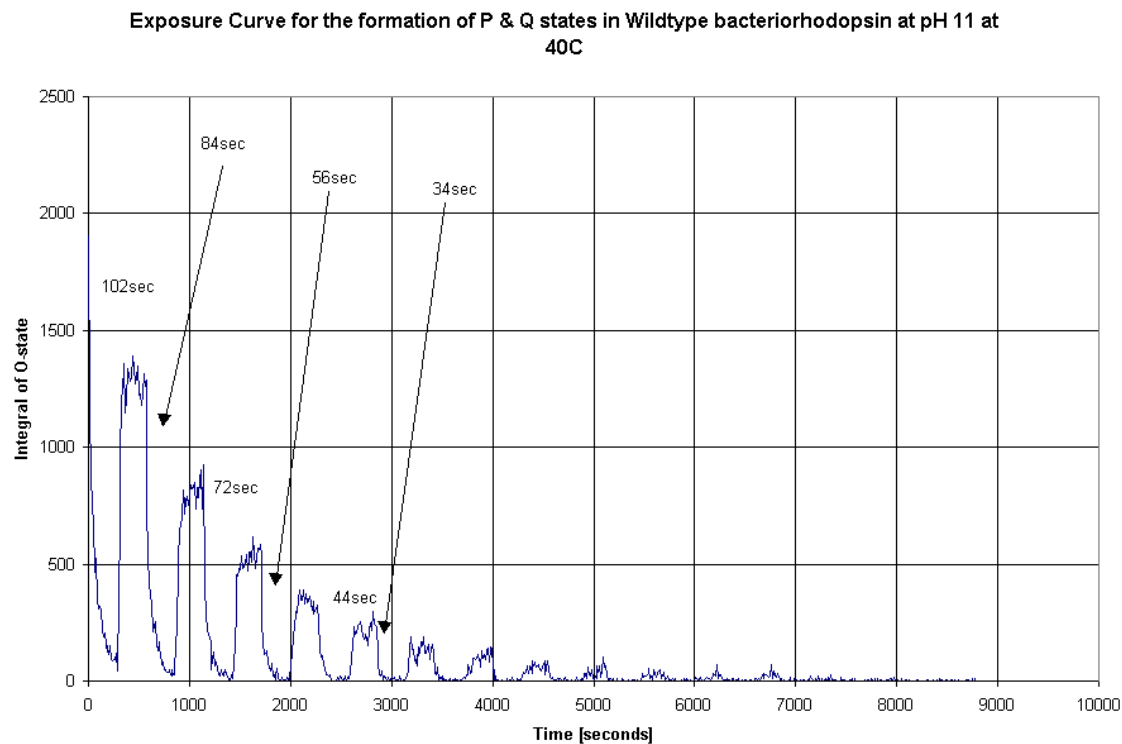


**Figure 3.22:** High pH response for the formation of P&Q in wild type BR.

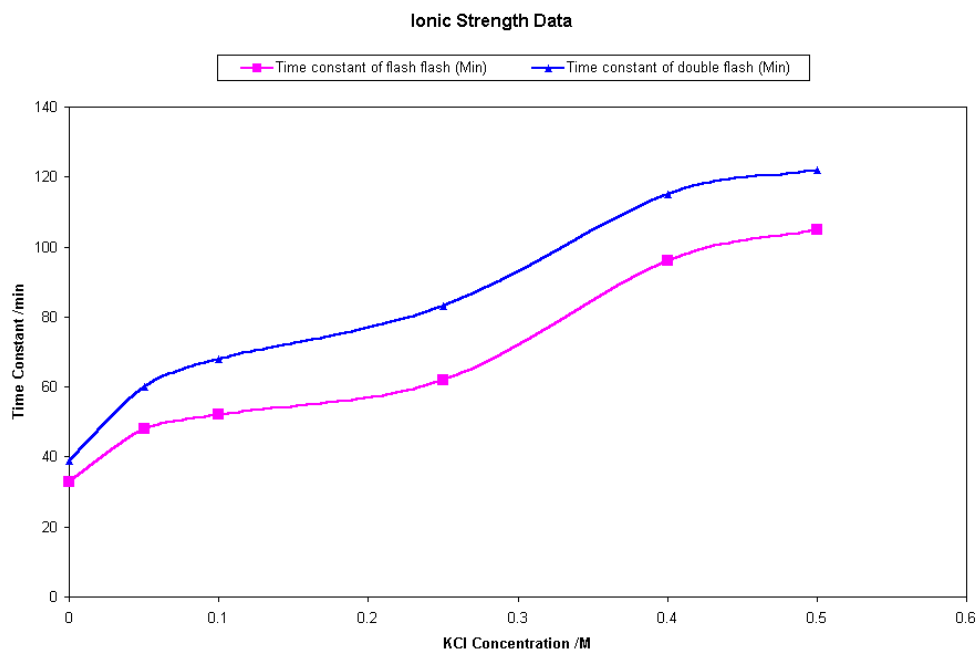
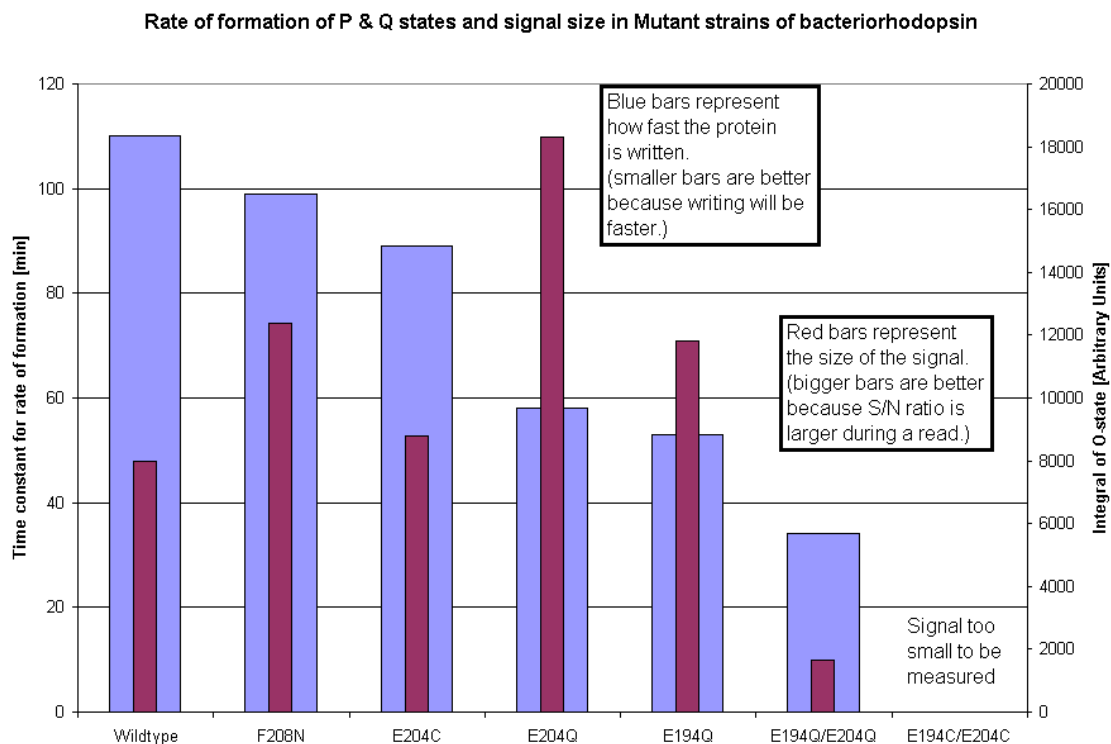


**Figure 3.23:** Ionic Strength Dependence of the Formation of the P and Q-states

**Figure 3.24: Mutant Dependence of the Formation of the P and Q-states**



### 3.1.2. Materials Research at Carleton University

The task of optimizing the polymer host matrix was trusted to Professor Wayne Wang and his student Jeff Franklin of Carleton University, who were responsible for optimizing the matrix with respect to long-term stability and optical clarity. Their progress during the final year of the grant is detailed below. Their progress toward optimizing various hydrogel formulas has been previously outlined in Air Force Report AFRL-IF-RS-TR-2001-279.

The progress described below represents the progress made by researchers at Carleton University during the last year of the grant, as mentioned above. The cumulative results of this research are most impressive, with tremendous reductions in light scattering and optical clarity, coupled with advances in long-term thermal stability. Reductions in light scattering in poly(acrylamide) gels were obtained through the judicious addition of refractive index matching agents. However, the use of ultra high density hydroglasses (as opposed to hydrogels) resulted in a reduction of light scattering in a hard matrix with excellent long term properties. Progress is detailed below in all areas (for both poly(acrylamide) hydrogels and hydroglasses) with respect to aging studies, light scattering, photocuring matrices, and hydroglasses.

### 3.1.2.1. Gel Aging

Experiments with regard to the aging of gels have been monitored for shrinkage, distortion, discoloration, and light scattering under various environments. The effects of pH and temperature on both gel shrinkage and light scattering were examined. It was found that both pH and temperature display an effect on the light scattering of a given gel, while only temperature seems to display an effect on gel shrinkage.

One current theory is that much of the observed deformation comes from chain relaxation of the polymer. In order to test that theory, we have added water to a few distorted gels and allowed them to re-expand. These gels were then resealed and left to stand at room temperature for observation. One notable finding is that submersion of the polymerization solution in a cool bath immediately following mixing markedly reduces the amount of shrinkage observed in the gels over the first few weeks proceeding gelation.

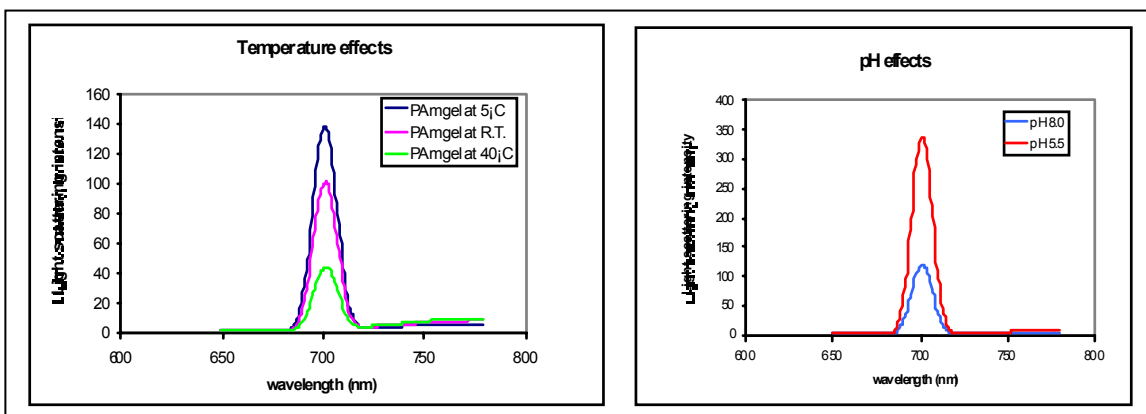


**Figure 3.24:** Effects of temperature and pH on light scattering of PAm gel.

### 3.1.2.2. Summary: Light Scattering Studies

#### 3.1.2.2.1. Characterization of Refractive-Index Matching Gel Additives

Throughout the duration of this and the previous contract, part of the ongoing materials effort has involved reducing the light scattering in the memory gels via the addition of refractive index matching agents. After examining a large number of additives, simple sugars seemed to be the most effective. Proline and Sucrose gels were synthesized with promising results. In addition, the sugar trehalose was investigated with almost identical results to that of sucrose, however, trehalose is a better “long term” storage sugar to use in the production of gel cubes since it is more stable than that of sucrose. Furthermore, several additives we have used to reduce the light scattering properties of the poly(acrylamide) hydrogel system were also applied to another hydrogel, PHEA. This experiment proved that our method of light scattering reduction through the incorporation of biocompatible additives can be applied to other types of polymer systems with the same sort of success.

In addition to monitoring PAM hydrogels containing sucrose for stability over time, various other hydrogel systems and combinations thereof were investigated over the

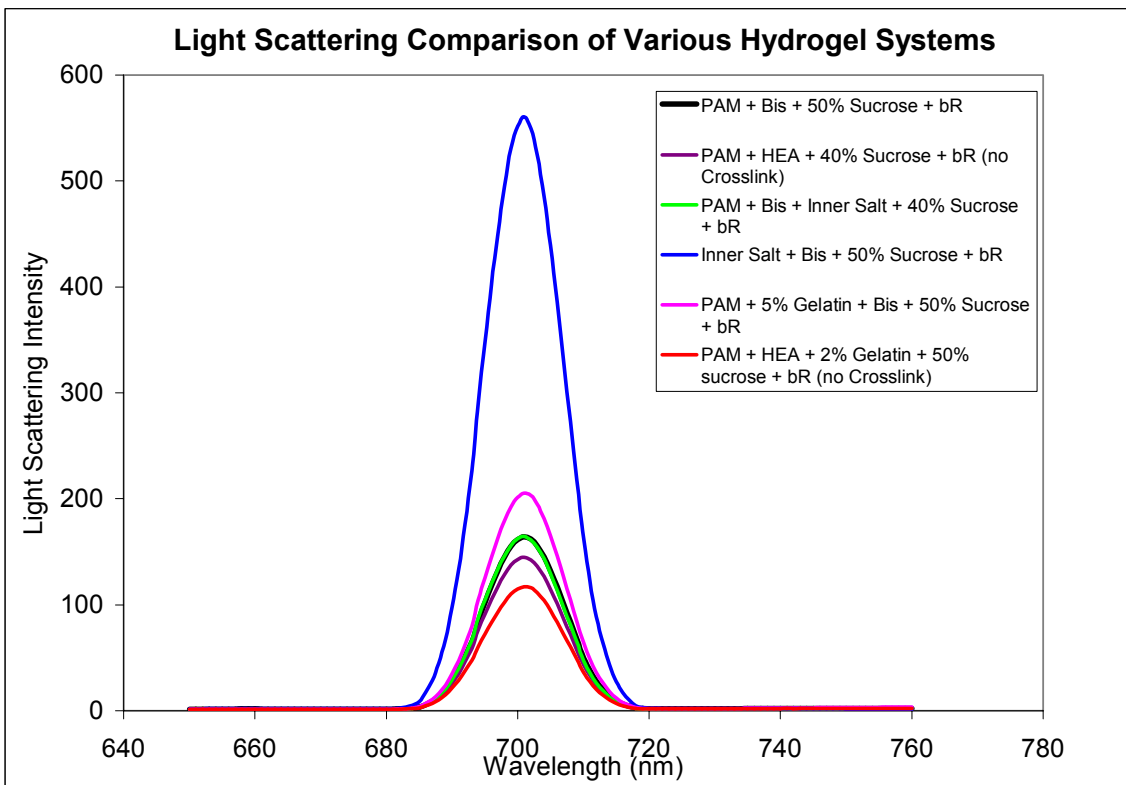


**Figure 3.25:** Light Scattering Comparison of Various Hydrogel Systems

last quarter for their light scattering characteristics as well as for their stability and biocompatibility. Copolymers of acrylamide + 2-[(methacryloyloxy)ethyl dimethyl (3-sulfopropyl) ammonium hydroxide] inner salt + Methylene bis acrylamide; acrylamide + hydroxyethyl acrylate; 2-[(methacryloyloxy)ethyl dimethyl (3-sulfopropyl) ammonium hydroxide] inner salt + Methylene bis acrylamide were investigated over varying concentrations of monomers and additive. Combinations of polymers such as PAm + gelatin, and PAm/HEA copolymer + gelatin were also investigated for light scattering properties with and without the additive “sucrose” over various concentrations. Figure 3.25 displays the light scattering measurements of these various polymer systems. All gels used in this comparison contained the same amount of bacteriorhodopsin. As can be seen in the figure, some hydrogel systems displayed better light scattering properties than that of the optimal PAm system, while others displayed higher scattering than seen in the current PAm gels. A unique finding has been the copolymer of PAm with HEA. This copolymer actually forms a “physical” hydrogel (i.e. gels without covalent crosslinking via hydrogen bonding) when appropriate monomer concentrations are used. From this gelling point on, it was observed that the rigidity of the gel is increased with increasing concentrations of monomer(s). Several concentrations were investigated and their stability monitored up to 70°C. This experiment demonstrated that none of these physical hydrogels became fluid at elevated temperatures (i.e. 70°C) and can therefore be said to display relatively high thermal stability. The fact that there is no covalent

crosslinking within this system allows for a reduction in light scattering over gels that have covalent crosslinking (i.e. PAm). This can be seen in Figure 3.25. The two polymer systems that proved to be better than the PAm system in terms of light scattering were those utilizing this copolymer hydrogel. It can also be noted that the Pam/HEA + 40% sucrose gels displayed better light scattering properties than the Pam + 50% sucrose system with 10% less additive incorporated. Thus, this system can be further improved with increased additive concentration. Further studies of this hydrogel system and investigations into aging of the gel will be required.

### **3.1.2.3. Summary: Development of a Photocurable Polymer Matrix**

One conceivable way of solving the problem of long-term curing effects in the gels (that result in shrinkage) is the utilization of a polymer matrix that is formed by exposure to the appropriate wavelength of light. In our current system, the polymerization of the acrylamide molecules is induced chemically, employing both a catalyst (ammonium persulfate) and an accelerator (TEMED). As the gel matrix is formed, the polymerization becomes a diffusion limited process causing the reaction rate to decrease substantially. However, the rate does not go to zero, and one plausible explanation for the observed gel shrinkage is the contraction of the gel due to the long term reaction of unbound acrylamide and bisacrylamide monomer. A photocurable system uses light as the catalyst, meaning that the reaction will only proceed as long as light of the right wavelength is present. A full background on the synthesis of photocurable and photo-cross-linkable polymer matrices is available in the original proposal for this research effort.

Two photo-cross-linkable polymers were initially attempted, one containing cinnamoyl chloride and the other containing acryloyl chloride as cross linking agents, with a parent copolymer of dimethyl acrylamide / hydroxy ethyl acrylate (MW 71,000). Two grams of the cinnamoyl containing photo-polymer were prepared as outlined in proposal for this project. In addition, 2 grams of an acryloyl containing polymer were prepared from the same parent polymer under the same conditions. These polymers were checked by IR and NMR, both of which appear to be promising. A crosslinking study of the polymer in dilute solution was carried out and displayed a decrease in cinnamoyl absorbance over irradiation time with UV light. This indicates that some crosslinking is indeed occurring. However, no gelation of the polymer solution was observed. UV irradiation of a polymer solution (aqueous) under the high intensity “Novacure” instrument for approximately 3 minutes, yielded a gel. In addition, subsequent tests were performed using a less intense source for a longer period of time, and again the polymer solution formed a gel. Under both conditions, the newly formed photo-crosslinked hydrogel were extremely cloudy and caused a large amount of light scattering. This cloudiness is likely a result of the large proportion of hydrophobic moieties in the polymer. The photo-polymer of discussion was synthesized to contain ~ 10% crosslinking sites which is much higher than needed and makes the polymer less hydrophilic since the cinnamoyl moiety is hydrophobic in nature. Thus, new photo-crosslinkable polymers can be synthesized to contain less of these moieties which will reduce the observed cloudiness and hence the observed light scattering.

In order to decrease the cloudiness in the new polymer, the effect of additives was investigated. The results demonstrated that the inherent hydrophobicity of the polymer as synthesized is not sensitive to the use of additives since there was no change in the light scattering observed. Sucrose, proline, and glycerol were used as additives but to no avail, however, a more rigid or “firm” gel seemed to form as a result of their use.

In an attempt to remedy the light-scattering problems, a copolymer of dimethyl acrylamide and Hydroxyethyl acrylate was synthesized at a 50/50 ratio. This increases the amount of hydrophilicity of the parent polymer prior to modification with cinnamoyl chloride. In addition, the percentage of cinnamoyl moieties incorporated was reduced from ~12% to ~3%. This again reduces the number of hydrophobic groups present on the modified polymer. Upon irradiation under UV light, crosslinking was observed with a large reduction in “cloudiness” of the matrix, however, the matrix was still somewhat fluid. This suggests that either the amount of crosslinking moieties present is not great enough to form an effective 3D network or it is possible that the molecular weight of the polymer is not high enough for this degree of crosslinking. The synthesis of more DMAM/HEA copolymer (50/50) was carried out, but an additional step was taken ruling purification in order to isolate only the high molecular weight polymer present in the reaction mixture. A technique called “reverse precipitation” was utilized in order to effectively obtain the high molecular weight polymer. This procedure was used since the GPC trace of the initial polymer product displayed a high polydispersity and a fair amount of “oligomer” sized molecules. This would undoubtedly affect the efficiency of the final crosslinking reaction, and thus precautions were taken to avoid such difficulties. The high molecular weight portion of the reaction was successfully obtained, as monitored by GPC, however, the yield of polymer obtained was vastly reduced. Therefore, another reaction was setup to produce a sufficient amount of the high molecular weight polymer to be isolated by this protocol. The results of this last reaction are not yet available.

Another polymerization was set up to form the copolymer of dimethyl acrylamide and hydroxy ethyl acrylate. The reaction was performed, and the corresponding polymer was isolated. The molecular weight of the polymer product still remains to be analyzed. This polymer was modified as previously outlined using cinnamoyl chloride to yield the photo-crosslinkable system, however, this reaction was modified over that previously used such that the number of cinnamoyl moieties to be incorporated into the polymer was vastly reduced (i.e. ~1% cinnamoyl groups). Analysis of the results is ongoing.

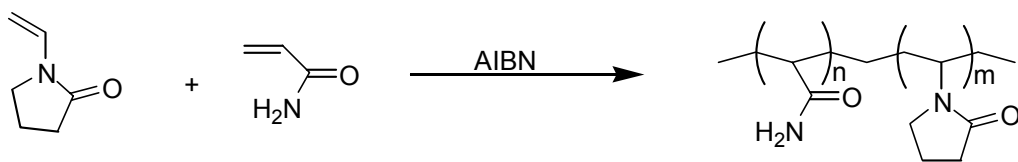
In addition, a reaction was performed in an attempt to synthesize a photo-active monomer for use in copolymerization. 2-hydroxy-ethyl acrylate was reacted with cinnamoyl chloride in DMF and yielded promising results. The product seems to be the desired photo-active monomer as characterized by IR and NMR. A similar reaction was previously outlined (see AFRL-IF-RS-TR-2001-279) in which an interfacial approach (chloroform & water) was used but there was incredible difficulty in isolation of the product and the yields were extremely low.



Investigations into alternative, more hydrophilic hydrogels has looked at using monomers such as hydroxy ethyl acrylate, 2-[(methacryloyloxy)ethyl dimethyl (3-sulfopropyl) ammonium hydroxide] inner salt, ethylene glycol methacrylate phosphate, and ethylene glycol methyl ether acrylate. Some promising systems have emerged as a result of these investigations, however, their stability must still be monitored. In addition, a polymerization reaction of maleic anhydride with N-vinyl-pyrrolidinone was attempted but only yielded low molecular weight polymer or oligomer; thus variations to the reaction scheme will have to be made in order to improve polymer formation.

Photo-crosslinking efficiency/effectiveness was investigated with changes in mole % of the cinnamoyl moiety. As expected, the greater the mole %, the greater the crosslinking, and stability of the system, however, a point is reached (in mole %) when the system becomes no longer water soluble due to high content of the cinnamoyl moiety. Thus if a photo-crosslinking reaction such as this was to be used for application to 3D optical storage, then an optimal range could be probed that would provide the needed stability with the appropriate solubility.

A copolymer of N-vinyl pyrrolidinone and acrylamide has recently been made that has very good optical properties and contains desirable sites for further modification (see scheme 1). The amine functionality can be used to crosslink the polymer system directly with an agent such as glyoxal or it can be modified to incorporate other groups such as a photo-crosslinking site. In addition, the polymer system displays good compatibility with bacteriorhodopsin.



**Scheme 1: Preparation of NVP/Am copolymer**

Future work will be directed towards improvements in the photo-crosslinkable polymer system, either through reduction of hydrophobicity in the preformed polymer or by copolymerization of the photo-active monomer with more hydrophilic comonomers. The fact that formation of a photo-crosslinkable system has been demonstrated is of tremendous importance. Reduction of the photo-polymers' light scattering should be fairly straight forward, however, optimization of the photo-crosslinking conditions (i.e. optimal concentrations, time, etc) will require more time. Efforts need to be directed toward improvement in the photo-crosslinkable polymer system, either through reduction of hydrophobicity in the preformed polymer or by copolymerization of the photo-active monomer with more hydrophilic comonomers. As well, future work into alternative polymer systems will be ongoing with investigations into the stability of the more promising polymers. Of particular interest is the preparation of hydroglass structures at an optimal pH value so that a bR concentration can be determined which may yield

maximal O state signals of the protein within the data cube. The sealing protocol of these cuvettes will follow the outlined procedure above and still needs to be monitored over time for their structural stability.

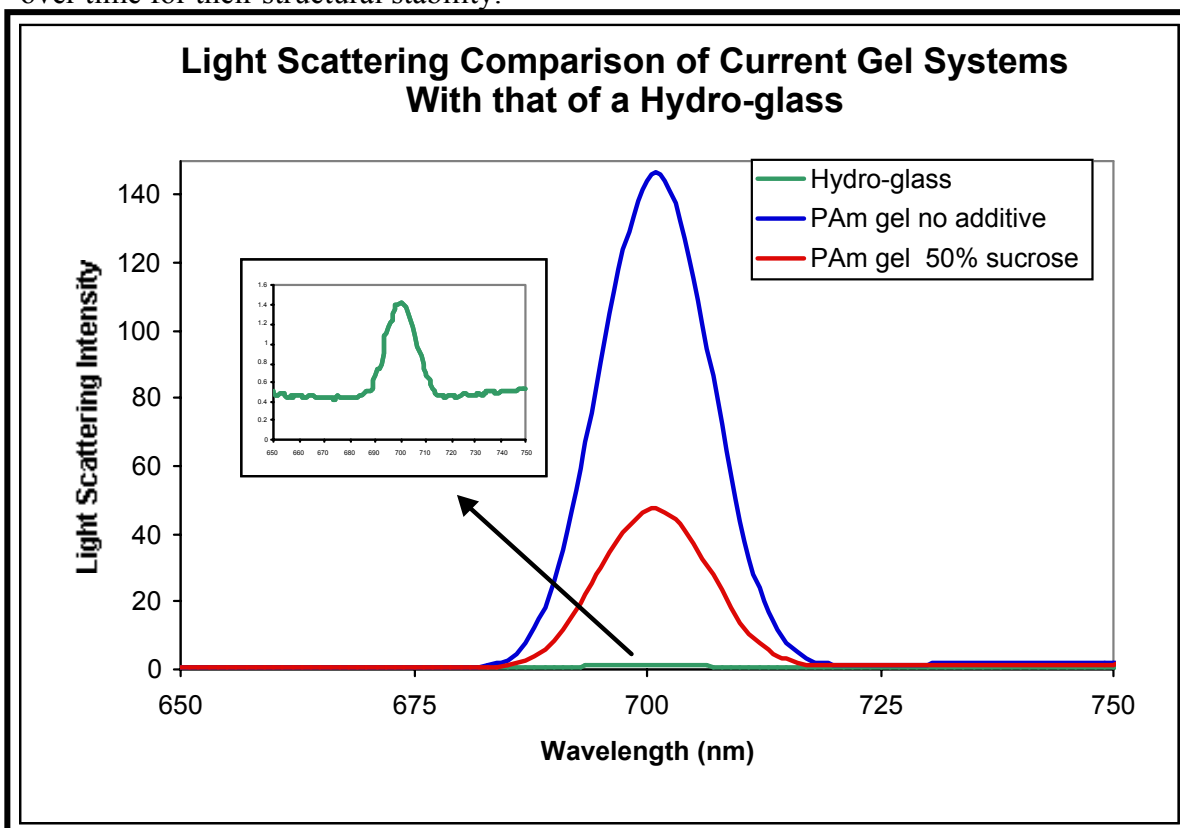


**Figure 3.26:** Light scattering comparison novel hydroglass with previous formulations.

#### 3.1.2.4. Development and Characterization of Polymer Hydroglass Systems:

During the last year of the grant, Jeff Franklin of Carleton University devised a new class of gels for the project, termed hydrogels or hydroglasses. These extremely rigid gels were made using much higher concentrations (i.e. 60%) of monomer as well as an increase in crosslinking agent concentration (acrylamide and bisacrylamide). The resulting gels had a much harder texture and seemed to be optically transparent, although, extremely brittle. An alternative crosslinking agent (piperazine diacrylate) was utilized since it has a six member ring structure and would likely introduce more rigidity into the crosslinked system. The reaction was carried out in water as the term “hydro-glass” implies. Very hard, rigid structures were produced that could be removed from the mold in which they were made (i.e. cuvette). Several different shapes were made in different containers such as; NMR tubes, glass vials, cuvettes, etc. The resultant glass-like structures displayed a high degree of hardness. Some of these polymer structures were cut using a glass-cutting instrument which demonstrated their ability to be subjected to mechanical stress without fracture. The structures also seemed hard enough to be machine polished, however, this still remains untested. The reaction itself is sensitive to various factors such as oxygen and concentration of catalyst. For example, if too much oxygen is present, the reaction slows and the resultant polymer is not as hard as those produced under inert atmosphere. In addition, too much catalyst results in very brittle,

often fractured polymers, while too little catalyst yields softer polymer structures or no reaction.

The light scattering of a hydro-glass cube was tested on the fluorimeter as done for all hydrogel cubes to this point. The scattering was compared to that of a polyacrylamide hydrogel without additive and to one with 50% sucrose (current system) (Figure 3.26). As can be seen, the hydro-glass cube has a marked reduction of light scattering over the current system. Just to point out, the hydrogels were run on the fluorimeter in plastic cuvettes, while the hydro-glass cube did not require a plastic cuvette to contain it.

One impediment to incorporation of bacteriorhodopsin into the hydrogels was the excessive amounts of heat generated during polymerization. The polymerization was monitored using a thermocouple and found to reach temperatures around 105°C. The temperature only remained above 100°C for approximately 25 seconds—however, the temperature is just too high for bacteriorhodopsin to be successfully incorporated. Thus, attempts to fine-tune this aspect of the reaction to a more acceptable temperature for bR incorporation were made. By varying the amount of catalyst, the reaction was slowed somewhat and by placing the cuvette in a water bath during the reaction, successful incorporation of bR occurred. This incorporation was not 100% successful; approximately 40% of the bR was denatured from the exothermic reaction, while approximately 60% remained. This was assumed through the color of bR added and that left in the polymer (i.e. the less bR present, the lighter the purple color). Alternative Hydroglass systems were also investigated. The methods used for the acrylamide, methacrylamide system outlined above report were applied to other monomers. Several combinations of monomers worked well in producing a very hard, glassy structure. In addition, several showed great promise in their light scattering characteristics and the fact that low levels of heat were generated during the reaction.

Following these initial attempts, several hydroglass structures were successfully formed using various monomers such as; Hydroxy ethyl acrylate, Hydroxy ethyl methacrylate, Hydroxy acrylamide, Hydroxy methacrylamide, 2-[(methacryloyloxy)ethyl dimethyl (3-sulfopropyl) ammonium hydroxide] inner salt, N, N-dimethyl acrylamide, methacrylamide, and acrylamide. Monomers were used in various combinations to yield hard, glassy structures. However, depending on concentrations used and the types of monomer, some structures were found to be more rigid and hard than others. It was also found that when using large amounts of hydroxy ethyl methacrylate or hydroxy ethyl acrylate the protein was denatured due to the toxicity of these compounds. Therefore, attempts to keep the concentration of these monomers low enough to incorporate bR are currently underway. In this sense, combinations of three or more monomers are being utilized in various concentrations to yield hydroglass structures. Hydroglasses formed from acrylamide and the inner salt monomer have been used for the successful incorporation of bR. This hydroglass is not as rigid and hard as the methacrylamide/acrylamide structures but it is much more biocompatible towards the protein. Both the toxicity and the heat of reaction are more suited to incorporation of bR.

Fine tuning of these formulations is required to overcome the tendency for the resultant hydrogels to be extremely brittle. By decreasing the amount of crosslinker or increasing the amount of monomer, it was observed that the resultant structures were not as brittle as those formed originally. However, these polymers were not as hard or rigid as the glass-like structures formed from the acrylamide/methacrylamide system first reported. Improvements have been made to this system and thus further tests will be required. A comparison of these structures to the optimized polyacrylamide system should be made with the same concentration of bR present in both. Light scattering measurements are required for both of the samples and aging studies should be performed on each. This will allow one to observe any significant improvements of the new system over that of the old. These tests are currently underway.

Polymers of N-(hydroxymethyl) acrylamide and 2-[(methacryloyloxy)ethyl dimethyl (3-sulfopropyl) ammonium hydroxide] inner salt; and N,N-dimethyl acrylamide and N-(hydroxymethyl) acrylamide were also found to be effective for the incorporation of bR to some extent. The latter system was found to form very transparent, hard, glass-like structures but denatured some of the protein during polymerization due to heat generation. The other system incorporated all of the protein successfully but was also found to form brittle structures. Thus, alterations to concentrations, and polymerization conditions will be carried out in an attempt to achieve the desired characteristics for each.

Although the system is compatible with the protein and displays good optical clarity, when exposed to air, the structure tends to crack and deform at the surface of the polymer glass. Therefore, methods have been investigated to appropriately seal the hydroglass cubes such that no water loss or surface deformation can occur with time. When sealed from air, this system was shown to be stable for greater than one year, however the sealant used attributed a convex type shaping to the outer walls of the material thereby preventing optimal writing and reading conditions. Thus alternative means were investigated. In addition, the pH of the hydroglass structures was investigated for the effects of "O state" formation in the bacteriorhodopsin photocycle.

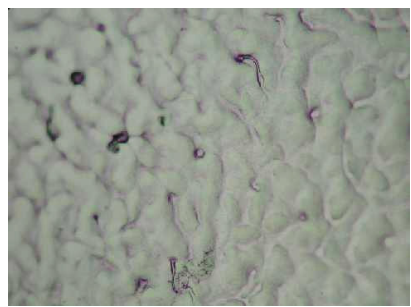
As a means of addressing the sealing issue, various types of epoxy coatings were investigated as well as various methods of application. Dip coating and spray coating of the sealant were both attempted, however, they displayed less than favorable results. Therefore, it was decided that in order to yield an effective cube structure that can be sealed air tight, the hydroglass was to be left in the plastic cuvette in which it was formed. The formulation of the hydroglass polymerization solution was also slightly altered to yield a hard but "tacky" structure that may adhere or stick better to the inside walls of the cuvette. These structures were then, upon cooling, sealed with water, wax and optical epoxy. These structures seem to display acceptable stability and were thus investigated further for writing capabilities.

The samples described above were prepared over various pH ranges (6 – 10) in order to investigate the effects of the system pH on the ability to generate an O state signal of the protein. It was found, as expected, that at higher pH (i.e. pH 10) the signal for O state generation was much greater than that at a lower pH value (i.e. closer to pH

6). With this in mind, the issue of protein OD should now be addressed in order to achieve a maximal signal. To date samples have been prepared at fairly low OD.

In addition, a study was carried out to determine the relative water content within the various hydroglass structures compared to that of a polyacrylamide hydrogel. In order to do this, samples were analyzed on a Seiko TG/DTA 220 where upon the temperature was raised from 20°C to 180°C at 5°C/minute. The temperature was held at 180°C for 10 minutes in each case. All weight loss that occurred at this temperature range was attributed to water loss. The samples analyzed were 1) a very rigid, hard hydroglass structure, 2) a hard, but tacky hydroglass structure, and 3) a PAm hydrogel. The results obtained are as follows:

Polymer System	Weight % Water in Polymer System
Hard hydroglass	14.6 %
Tacky Hydroglass	35.8 %
PAm Hydrogel	73.4 %



Initial problems in obtaining an O state signal within the hard hydroglass structure may have been attributed to the low water content in this case. Surface photographs of a hard hydroglass structure and a PAm gel were taken on a reflectance microscope to see if there was any similarity/differences in surface structure between the two systems. Figure 3.27 displays the results. It can be seen that in the hydrogel, there is a majority of water and hence the surface seems fairly flat and smooth. However, in the hydroglass the majority is polymer network with channels of water (which seem to contain the protein) incorporated. Thus, the surface displays more texture at a microscopic level.

**Figure 3.27:** Surface morphology of a PAm hydrogel (top) and a hydroglass (bottom) system.

X-ray data was also run on the hydroglass systems (both Rigid and Tacky) to determine whether or not the system had any sort of crystallinity to it. The results determined that there is no sort of crystallinity whatsoever in these two systems, they were both observed to be amorphous.

**Figure 3.28:** BR-Hydroglass sealed with UV cured epoxy



### 3.2. Bacteriorhodopsin-Based Three-Dimensional Memory Prototypes

During this research effort, a series of prototypes were constructed. Initial devices were simple screening devices meant to evaluate various protein-based memory media with respect to the efficiency of branched photocycle access. These units were developed in-house and were instrumental, both in formulating the

memory medium and for memory architecture design. However, in order to take the technology to the next level of sophistication, a local custom-electronics/prototyping firm was contracted to build the final prototype that is discussed below.

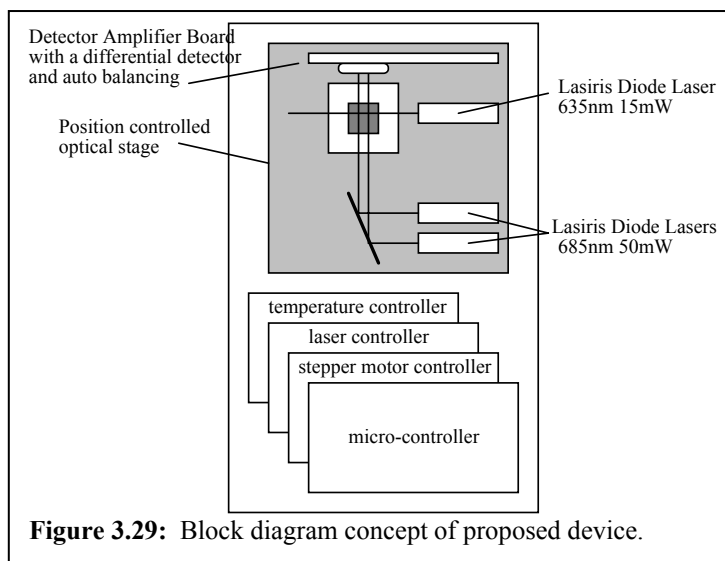


**Figure 3.29:** Block diagram concept of proposed device.

#### 3.2.1. Critical Link Prototype

##### 3.2.1.1. General Description

The final series of prototypes were developed in collaboration with Critical Link, Inc., of Syracuse NY. Critical Link is a custom prototyping firm capable of a much higher degree of sophistication than possible in house at Syracuse University. The Critical Link Prototype is a self-contained memory device capable of discrete data storage, with an ultimate capacity of 3 kB. The new prototype is modeled on the same design as previous systems fabricated in-house but includes higher power lasers, fiber coupling, vibration isolation, and 16-bit resolution differential detection (as opposed to 8-bit resolution absolute detection). The paging and data (diode) lasers are more powerful than those used in the screening device, and are coupled to the data cuvette by vibration-stabilized fiber optics. The data cuvette itself rests in a temperature-stabilized housing that sits on kinematic base capable of 2.5 cm displacement in x, y, and z. A vibration-stabilized base supports all of the surrounding optical components (including the detectors and fiber optic mounts). RS232 communication between the memory and the computer facilitates operation through a visual basic graphical interface, using a number of simple user-supplied commands.

##### 3.2.1.2. Operational Basis

Similar to the screening prototypes developed in house, the Critical Link prototype is not capable of parallel operation, predominantly due to limitations in the proteins evaluated thus far—until we have more efficient proteins for memory evaluation, the necessary intensity for photochemical access of the branched photocycle (i.e., writing) is

only possible at the intersection of the two laser beams emitted from the diode lasers. Once the protein efficiency problem is solved, parallel operation should be possible. However, the current architecture is capable of only single bit operation, and uses a differential reading process to determine the binary state of a particular location in the memory matrix. The original concept device schematic is shown in Figure 3.29. The basis for bit determination incorporates a series of three optical fibers coupled to the data laser and spaced 125 microns apart. Each of the fibers is used to interrogate neighboring bits, thereby determining the magnitude of the O state. The relative O-state magnitude is used to determine the binary state of the bit (a large O-state signal indicates a binary zero, while a small signal represents a binary one, as a result of photoconversion into the Q-state).

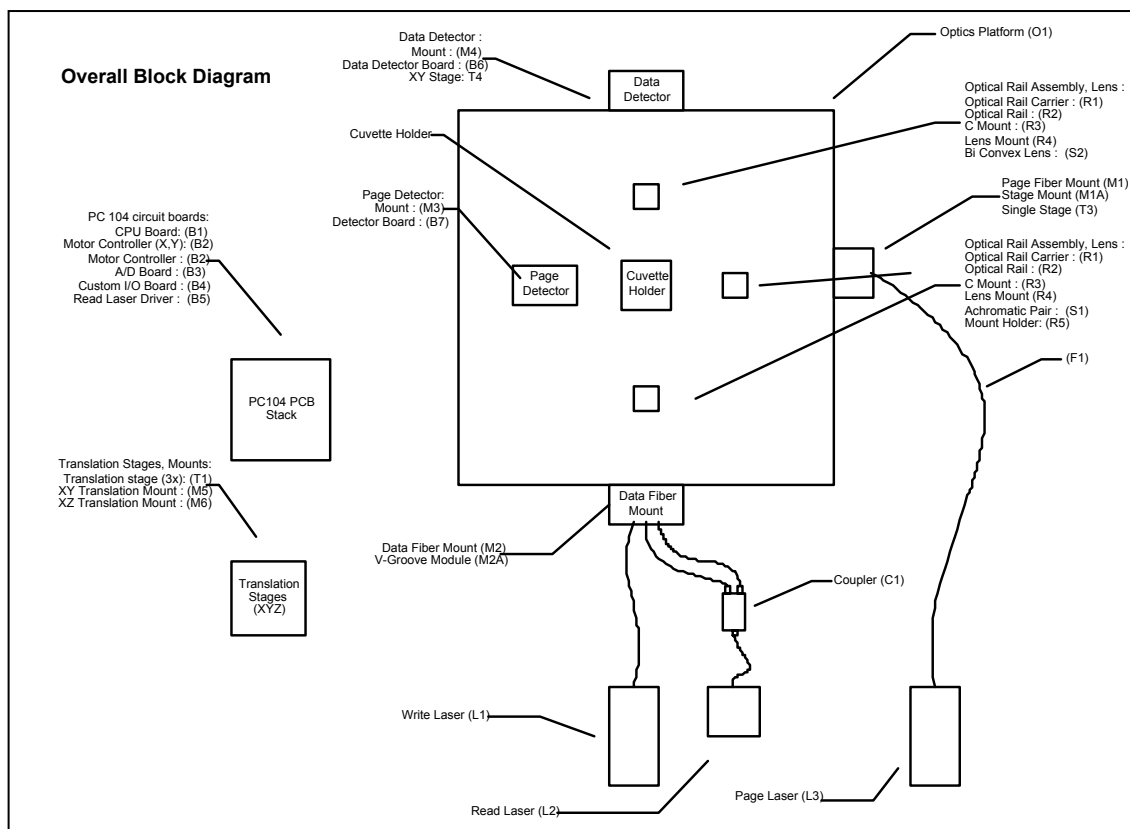


**Figure 3.30:** Overall Block Diagram of the device proposed by Critical Link, based upon concepts provided by the W.M. Keck Center for Molecular Electronics at Syracuse University.

A block diagram schematic of the device is shown in Figure 3.30. The goal was to develop a proof of principle random access memory controller, which would be capable of full write-read operation, as well as monitoring and maintaining an operational environment for the protein (with respect to temperature and ambient light levels, and interface with multiple computer interfaces). In addition, the prototype had to be self-contained and have a relatively small operational footprint. Several technical challenges of the architecture had to be overcome. Primarily, the prototype had to demonstrate the

technology by writing and reading simple binary data, which would take the form of a change in signal magnitude of the O-state. Discrimination between areas of photoconversion (i.e., zeros vs. ones) had to be implemented in the form of comparative differential absorptivities. Furthermore, a system for accurate mapping of binary data in a 3D environment also had to be incorporated, such that data could be reproducibly located on subsequent memory operations. For the actual device, this translated to a need to precisely align the relative orientations of both the data and paging lasers, the detectors, and the memory material. The following section details individual components of the prototype, including both illustration and relevant commentary. Critical Link's goal was to develop a proof-of-concept random access memory controller that had the following criteria: (a) 3D memory with capacity for 2k bytes composed of 32 x 32 x 32 cells in x/y/z planes in a 1cm<sup>3</sup> cube gel; (b) Built on the current technology developed at the W. M. Keck Center for Molecular Electronics, incorporating multiple independent light sources (orthogonal beams) and low noise detectors; (c) Investigate alternative technical approaches incorporating high power lasers, a differential detector, fiber coupling, and signal processing algorithms; and (d) Develop new generation platform to continue research

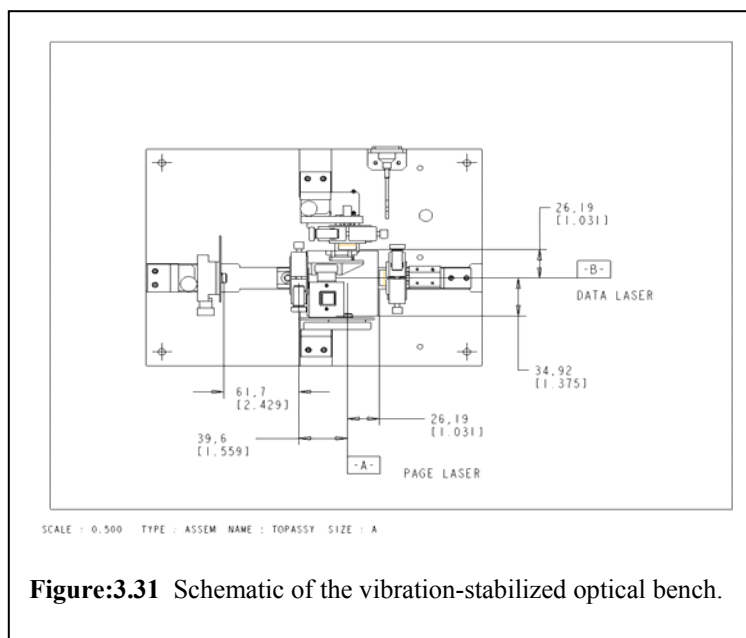


**Figure:3.31** Schematic of the vibration-stabilized optical bench.

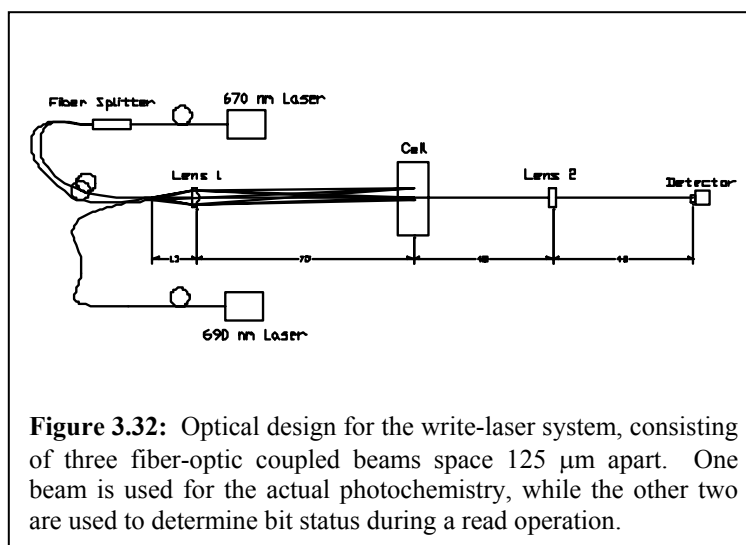


**Figure 3.32:** Optical design for the write-laser system, consisting of three fiber-optic coupled beams space 125  $\mu\text{m}$  apart. One beam is used for the actual photochemistry, while the other two are used to determine bit status during a read operation.

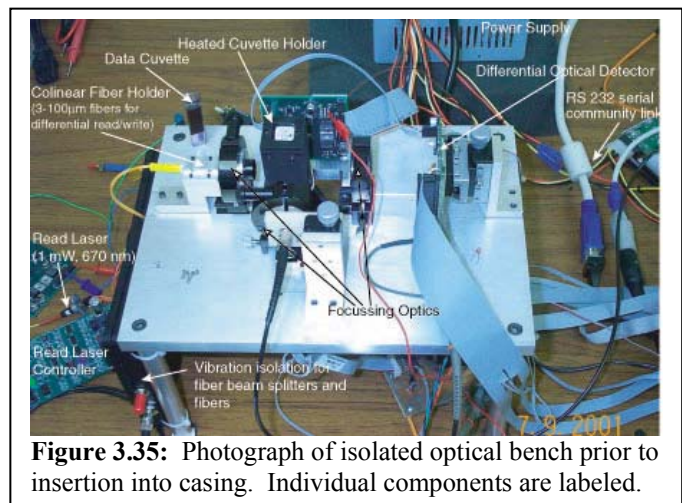
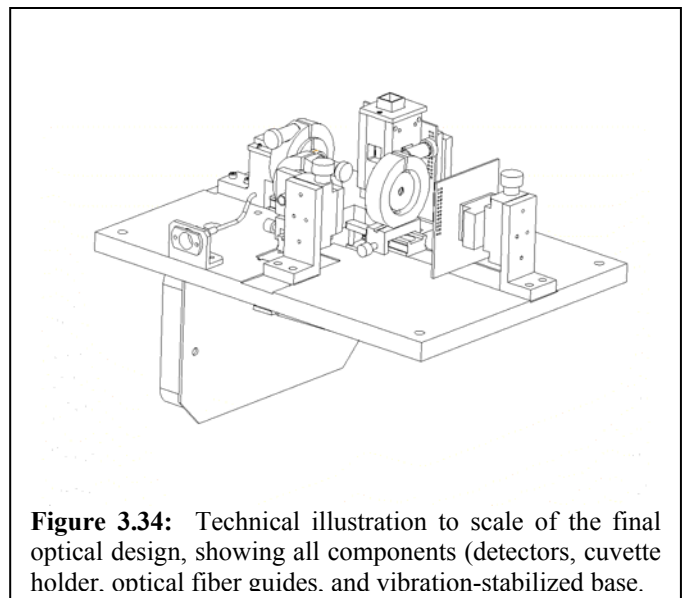
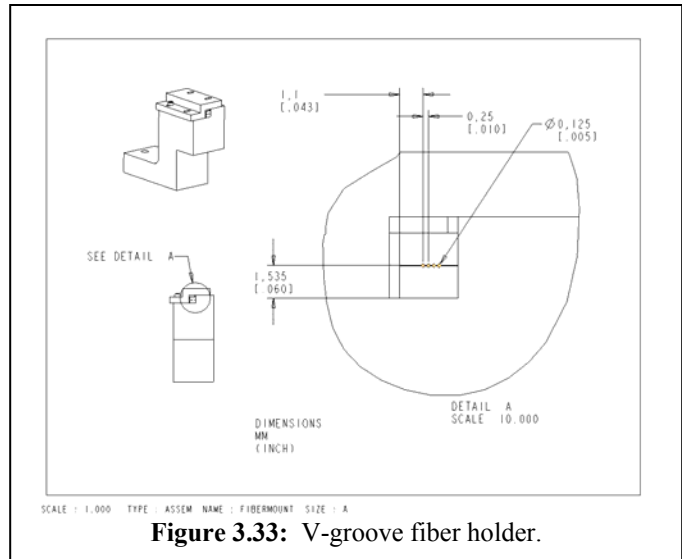
Multiple disciplines were needed to accomplish this, including optics, mechanical, electrical, software, system engineering, and various fields of chemistry. A strong interdisciplinary team was assembled to facilitate device design and construction. Critical Link used the same detector circuit used in the screening prototypes designed in-house



and adopted the same basic architecture (single orthogonal beams, not extended to page or image light paths). It was decided differential detection was the most important new advance; modulation of the light sources was required (i.e., different read and write intensity and control of one beam on or off for writing.) To simplify this, three independent sources were selected: two low intensity for read and one high intensity for write. Fiber coupling provided the best approach to form three independent closely spaced beams, and the highest power fiber-coupled laser modules available were chosen. The scope of the signal processing is a simple algebraic model to distinguish two very similar O-state integrals.

The following criteria were decided upon for the optics subsystem: (a) Design point selected calls for a differential detection to eliminate laser generated noise (b) probing laser illuminates 2 pixels, and (c) one pixel is the reference pixel.

Several alternative laser sources and optics arrangements were investigated, including direct coupling vs. fiber coupling, methods to accurately align fibers, and dual vs. triple laser sources. In the end, a design was chosen (illustrated in Figure 3.31) that incorporated three independent fiber coupled laser sources that comprised write, read, and probe functions, with the paging beam orthogonal to the write and probing beams. In addition, the probing beam was split to illuminate two pixels. This optical arrangement allowed for a 300  $\mu\text{m}$  diameter beam in the cuvette, and an illuminated area of 500  $\mu\text{m}$  at the face of the detector.



The paging laser chosen was a stand alone (diode & driver), fiber coupled (100  $\mu\text{m}$  core, 22 NA) 300 mW diode laser at 635 nm (TE cooled). A similarly configured write laser was chosen, 500 mW at 690 nm.

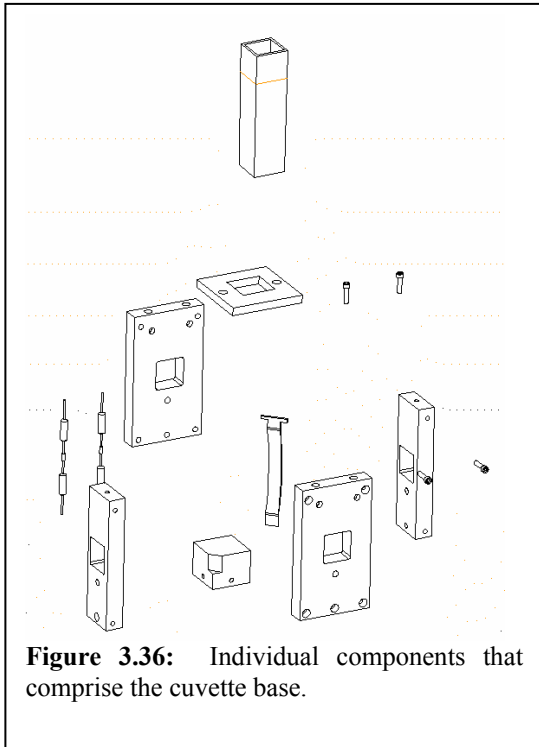


**Figure 3.36:** Individual components that comprise the cuvette base.

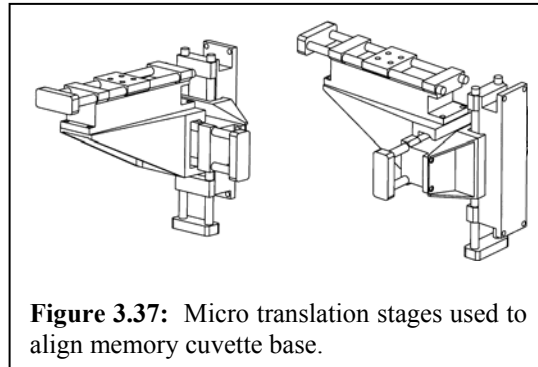


**Figure 3.37:** Micro translation stages used to align memory cuvette base.

The probe laser (Figure 3.32) was specifically chosen to be low power to avoid initiating any photochemistry—5 mW at 670 nm with separate diode & diode-driver boards, a low noise diode driver, fiber optic coupled, then split (50/50) with a 100  $\mu\text{m}$  splitter. The two optical fiber paths were secured with a V-groove fiber holder (Figure 3.33), a high precision linear fiber array that holds both probing and write fibers with a center spacing of 125  $\mu\text{m}$ . Photolithography was used to guarantee sub-micron tolerances.

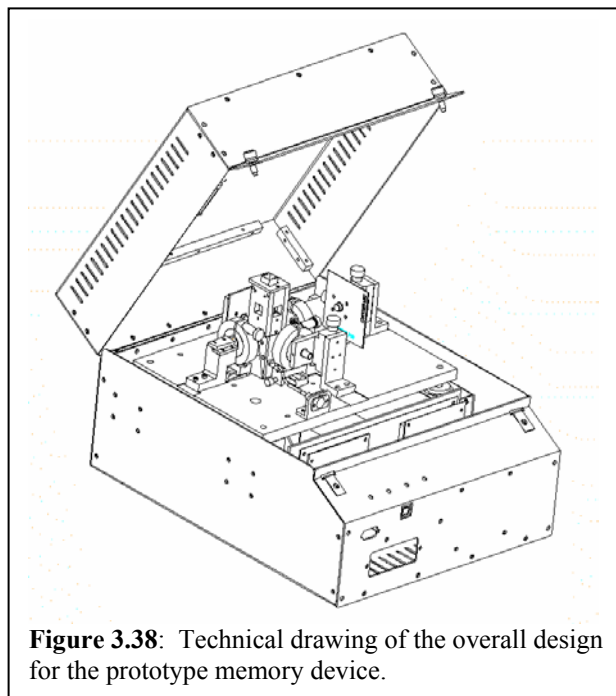


**Figure 3.38:** Technical drawing of the overall design for the prototype memory device.

The optical systems and detectors were placed on a vibration-isolated platform as illustrated in Figures 3.34 & 3.35. This precision machined aluminum plate is used as a base to attach the optics, motion system (see below), the data fiber holder & data detector, and the page fiber holder & detector. Alignment of the lasers was accomplished with two translation stages, one for alignment of the probe and data beams with the paging beam, and another for alignment of the probe beam with the data detector. The data cuvette is housed in a custom made holder, illustrated in Figure 3.36. The holder is attached to the motion system and uses a spring mechanism to hold the cuvette in place. Heat is delivered *via*

power resistors in the corners. Temperature monitoring is done *via* the two thermistors attached in the side plates. The position of the holder (and the cuvette contained within) is accomplished through three motorized micro translation stages (see Figure 3.37) that are capable of up to 2.54 cm translation in X, Y, or Z. The stages are controlled by DC servo motors, and can reproducibly locate any given position in a volumetric matrix with an accuracy of less than 10  $\mu\text{m}$ . Finally, the entire system is housed in a mechanical subsystem enclosure, containing the optics, electronics, and power supply. The optics platform is shock mounted to reduce vibrations. All of the enclosure sides are removable to allow easy access to internal components, and the cuvette is accessed through a hinged opening in the top cover (Figure 3.38).

The electrical subsystems were composed of a combination of off-the-shelf and custom hardware, with everything based on an industry standard PC-104 bus. Off-the-shelf hardware included an integrated CPU module with a bootable flash disk, two RS232 ports, a keyboard, IDE, floppy, and VGA support for development. The motor controller module is a two channel DC H-bridge servo with encoder inputs based on the National LLM629 module. The A/D module consisted of 16 analog inputs & 16 bit resolution, 100 kHz sampling rate, and 4 12 bit analog outputs. Custom electronic hardware included the data detector (dual photo diode detector, very low noise transimpedance amplifier, feedback loop with integrator and sample/hold for stability and acquisition control, analog variable gain amplifier to scale signal, and a differential signal driver). The page detector, also custom, includes power supply generation and filtering, as well as the associated low gain transimpedance amplifier for paging laser timing verification, making possible the capability of integrating the page beam intensity and controlling the beam on time for a more precise

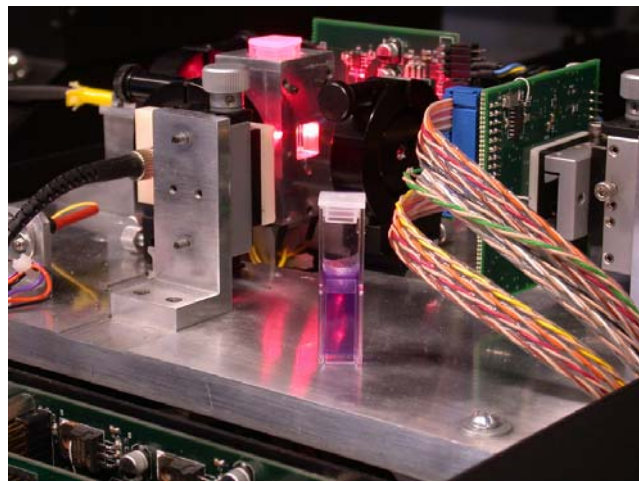


**Figure 3.39:** Close-up of prototype memory device, including memory cuvette in foreground. The read detector is on the left, facing the cuvette holder. Both fiber-optically coupled lasers can be seen entering from the left. The electronics in the foreground control all routine operations.

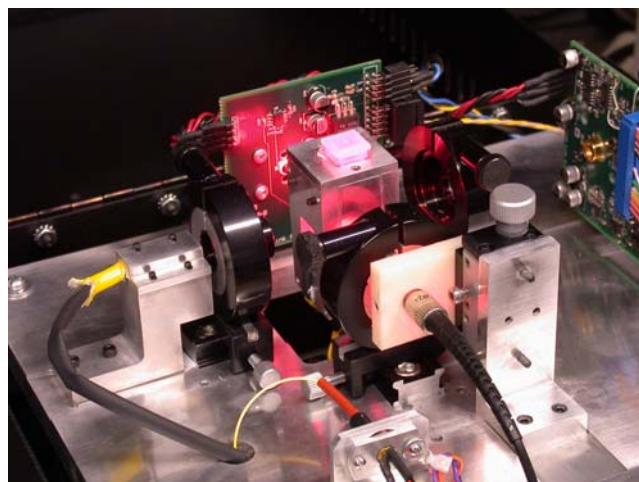


**Figure 3.40:** Another view of the optical base and associated components.



energy pulse. Other custom electronic hardware includes the following: Custom Xilinx FPGA for system timing and control, Laser modulation for Read and write cycles, PWM control for cuvette heaters, PC-104 backplane and mount, Motor encoder interface, Thermistor current source and amplifier, Cuvette heater drive circuitry, and Probe laser power supply generation.

Several embedded software systems also had to be written, including two independent software components that reside in the controller. These systems respond to host commands through a simple ASCII interface (MX 100, LP ON, RD). Other characteristics include RS/232 and USB support, device drivers for all hardware components, motor controllers, A/D board, lasers, and heater (*via* FPGA). Finally, the embedded software supports high level commands such as Read and Write operations and reports back status, cuvette temperature, and any errors. The host software runs on both Mac and PC with a simple windows-style interface to set any necessary parameters for routine write and read operations. A graphical display is provided for data collect, and script files are supported.

Overall, the major obstacle was overcoming noise in the signal generated during a read operation. A significant source of the noise was from the environmental mechanical vibrations that coupled into the fiber optical system. Differential detection did not eliminate all the noise, making shock mounting and signal processing algorithms necessary. There was virtually no electronic noise down to the A/D resolution. The laser also contributed some noise that could not be removed through differential detection. Reduction in laser-induced noise in the signal could only be obtained the examining several laser drivers, and selecting the best available. An additional source of noise could be from the memory medium itself, due to

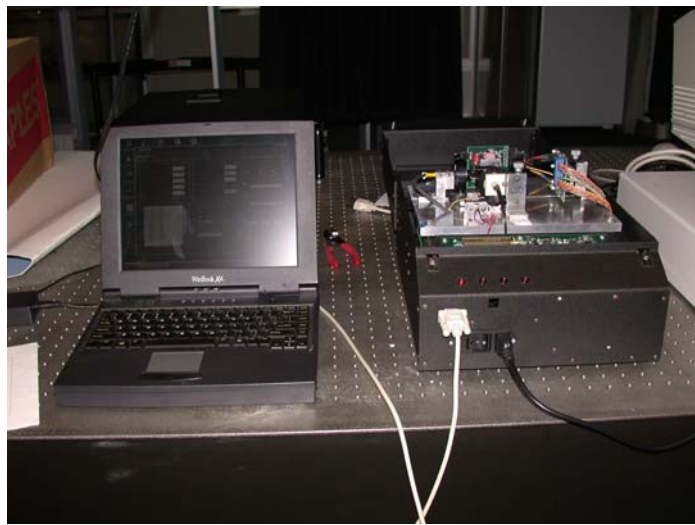


**Figure 3.41:** Full view of BR-based volumetric memory prototype. All aspects of routine write & read operations are handled via the interface (RS 232).

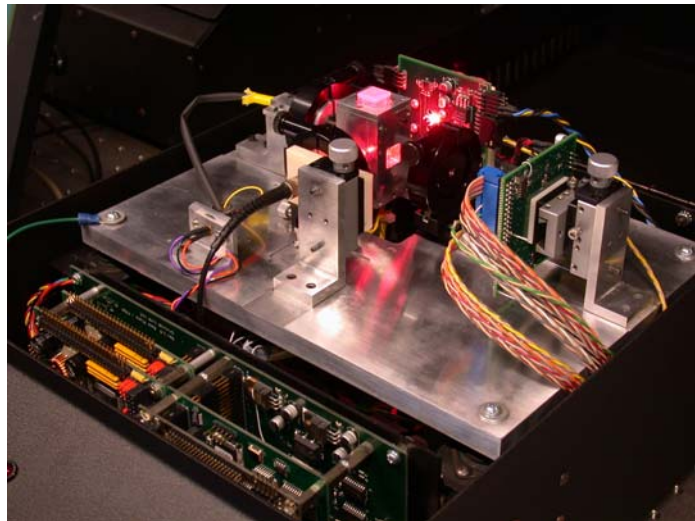


**Figure 3.42:** Expanded view of the optical base and associated components.

an apparent vibrational mode in the gel: a vibration mode in the gel will cause the excited beam of BR molecules to behave like a vibrating string. Current improvements in the stiffness of the memory medium fabricated by researchers at Carleton University are expected to resolve some of the media-related sources of noise.

Figures 3.39 through 3.43 show photographs of the actual unit designed and built in collaboration with Critical Link. More detail on technical specifications and the actual operation of the prototypes developed through this research effort is provided in the Appendix (*User Manual for the Protein-Based Three-Dimensional Memory Prototypes*) found at the end of this report.

#### 4.0. Conclusions

The original objective of this research effort was to investigate new technologies for enhancement of the Branched Photocycle Volumetric Optical Memory, based on the photochromic protein bacteriorhodopsin. Included was the goal to incorporate attributes that will lead to a reduction in both physical size and production costs, while increasing the efficiency by which the memory performs routine operations. A number of specific technical goals were set, including incorporation of diffractive and/or plastic optics that would be more cost-effective, utilization of economic linear array devices for writing and reading, and development of a computer interface with a cross-platform driver (SCSI II, SCSI III, and Firewire interfaces). Furthermore, the scope of the proposed project encompassed investigation of alternative disk-based architectures, investigation of random mutagenesis as a tool for generating enhanced BR mutant proteins with increased O→P efficiency, and exploration of photocurable polymer host matrices for bacteriorhodopsin that will overcome problems with long-term curing effects (e.g., gel shrinkage—*via* subcontract to Carleton

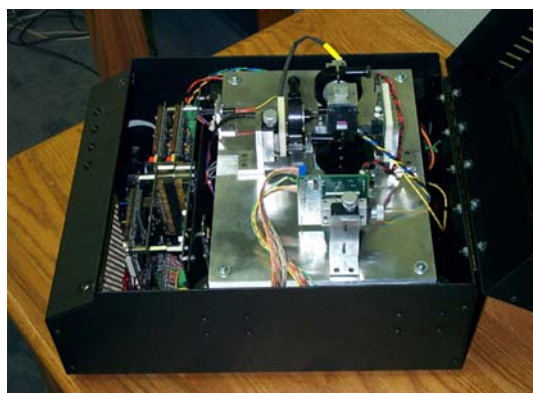


**Figure 3.43:** Two views of the completed prototype built in collaboration between Critical Link and the W.M. Keck Center for Molecular Electronics at Syracuse University.

University). The proposed tasks reported in the statement of work included the following specific objectives:

1. Development of novel photocurable polymer matrices that will exhibit reduced scattering and minimize gel shrinkage. In addition, engineering parameters and data necessary for large-scale production and pre-pilot production of the polymer matrix for fabrication of the BR-based memory medium for ultimate commercialization were to be collected.
2. Random mutagenic methods were to be employed toward the production of analog proteins better suited to memory storage. The novel protein variants were then to be evaluated with respect to photokinetic properties and potential as memory storage elements. Furthermore protein screening methods were to be explored.
3. An optical layout incorporating cost effective plastic and/or diffractive optics was to be developed. More cost effective linear array devices were to be explored for both the write and read operations as alternatives to spatial light modulators and CCD arrays.
4. SCSI II, SCSI III, and Firewire interfaces were to be developed that will allow the protein memory to be interfaced to any standard computer.
5. Disk-based architectures for the branched-photocycle memory were to be explored and developed as an alternative to the cube-based architecture.

Unfortunately, circumstances precluded meeting all of these tasks, although all of them were addressed as part of the research effort. As enumerated above, tasks one and two were fully explored and are discussed above (section 3). Although initially explored, tasks three & four were abandoned due to personnel turn-over and a major shift in the direction of the research effort (detailed below). Task 5 was never fully explored as it was deemed overly ambitious when considering the available personnel and resources. Despite the fact that not all goals were met, the progress made in the areas of new materials and prototype development were substantial, and have paved the way toward a commercially-viable technology. Specifically, the notable developments and advances were made through the initiation of an active program utilizing directed evolution for generation of more efficient and functional BR variants, generation of a novel memory matrix material that exhibits long-term stability, has high optical quality, and resists shrinkage, and the fabrication of a new series of prototypes. These prototypes are as fully developed as necessary given the current state of the BR-based memory medium, and are valuable for new materials evaluation.

#### **4.1. Why Some Goals Were Not Met**

The major obstacle to the satisfactory completion of the tasks above was the protein itself, as was recognized from the beginning of the effort. The main issue was

one of efficiency, in that although the branched-photocycle architecture is entirely valid and has been effectively demonstrated, it lacks efficiency to such an extent so as to preclude commercial viability—*for the wild type protein*. For this reason, the most successfully-completed task was the establishment of both the facilities and expertise necessary for implementation of new techniques in genetic engineering, namely, random & semi-random mutagenesis, and directed evolution. These techniques enable the production of new BR-based materials that will make commercial viability not only a possibility, but likely. The new capabilities described (and demonstrated) in section 3.1.1 are producing more protein analogs than can be effectively evaluated in a reasonable amount of time (e.g., see Figure 3.5). Basic screening procedures have been developed that examine the O-state *in vivo*, however directly examining the branched photocycle poses an exceedingly difficult problem and may not be possible. Some of directed evolution mutants, however, are already showing promise, including the triple mutant I119T/T121S/A126T; this has the highest Q-value we have yet measured for a BR mutant, and its efficiency and photokinetic properties are being evaluated at this time. And herein lies the beauty of the directed evolution technique—the roles of Isoleucine 119, Threonine 121, and Alanine 126 in bacteriorhodopsin are for the most part unknown, and rational mutant design would have disregarded their potential to improve bacteriorhodopsin's efficiency as a memory material. The added capability of directed evolution and semi-random mutagenesis to the W. M. Keck Center for Molecular Electronics, and its impact on protein-related device development, is perhaps one of the most valuable results of this research effort. It's full impact on the branched-photocycle memory remains to be realized. The primary remaining challenge is the development of a suitable high throughput screening protocol. Techniques such as flow cytometry to sort cells that have optimal properties and *in vivo* screening for the branched photocycle are currently being investigated.

With respect to task number one from above, development of a photocurable matrix, this task failed to produce the desired result. The polymer matrices obtained through development of photocurable polymers did not meet the initially positive expectations. Instead, the resultant gels suffered from poor optical quality (exhibiting extreme cloudiness), poor yields, or failure to form a suitable matrix that was not semi-fluid. However, an alternative non-photocurable approach has produced high-optical-quality hydrogels that resist shrinking and maintain a suitable environment for the protein. This new class of hydrogels—essentially ultra-high density poly(acrylamide)—are stable enough to use without a cuvette to contain them. Although more work needs to be done with respect to characterization and synthesis scale-up of these gels, they possess the most potential of any of the materials developed to date. Extensive characterization of the gels are needed, however, as bacteriorhodopsin and the branched photocycle are incredibly sensitive to the immediate chemical environment; initial studies have already indicated that the protein behaves differently when encapsulated in these new high-density hydrogels. This may be due to the reduced amount of water present as compared to the standard poly(acrylamide) gels used in section 3.1.1.

Without an efficient protein to drive prototype development, it was deemed unreasonable to pursue tasks three through five with any diligence. In addition, the



primary researcher involved in with these tasks was forced to relocate and leave the project due to personal reasons (Dr. Enrique Izaguirre). Dr. Duane Marcy was hired to replace Dr. Izaguirre, but by this time the deficiencies in the wild type protein were evident, and the research effort was redirected toward materials optimization. Dr. Marcy's primary contribution then became the motivating force for prototype development based on the original branched photocycle architecture. His designs culminated with the screening devices and the Critical Link prototype as described above, and in further detail in the Appendix that follows this discussion. These prototypes proved invaluable for characterization and evaluation of both novel bacteriorhodopsin variants and matrix materials. As such, we consider the development of these prototypes to be the major accomplishment under the collective auspices of this grant and Air Force contract F30602-98-C-0105.

## 4.2. Future Directions

The W. M. Keck Center for Molecular Electronics has been extremely fortunate to be the beneficiary of two generous federally funded initiatives delivered to us through Air Force Research Labs in Rome, NY. The ultimate goal of these funds was to provide the necessary research and development necessary to help make the transition of the bacteriorhodopsin-based three-dimensional optical memory from the laboratory to the marketplace. While that goal has not entirely been met, the progress

demonstrated through the combined efforts of these initiatives has verified the architecture and provided the direction that is needed to ensure the most feasible route to commercialization. The insight into the biophysical nature of both bacteriorhodopsin, and in particular the branched photocycle, gained through this research effort has been invaluable for future development of the BR-based memory device. It is now clear that the wild-type protein is not optimal as a volumetric memory element, and directed evolution is the best vehicle for production of an optimized protein (for this and many other biomolecular electronic applications). The implications of this revelation have the potential to be wide-spread in the field of biomolecular electronics: the researcher no longer has to rely on the confines and limitations of pre-existing natural properties. The ability now exists to improve the properties that tend to limit practical applications of proteins & enzymes, including long-term stability, expression level, narrow effective operational temperature ranges, substrate inhibition and competition, and reaction rates; in effect, we can improve upon properties and functionalities already present in Nature. Furthermore, the option now exists to “evolve” a protein in the laboratory to function in

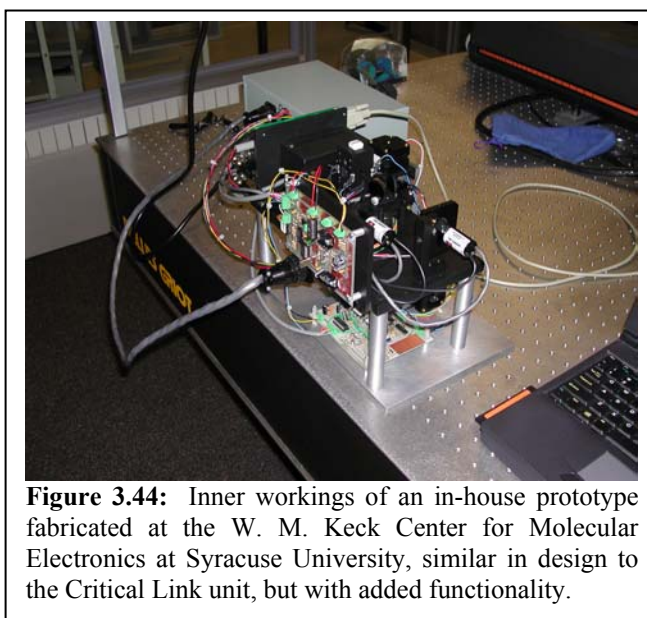


**Figure 3.44:** Inner workings of an in-house prototype fabricated at the W. M. Keck Center for Molecular Electronics at Syracuse University, similar in design to the Critical Link unit, but with added functionality.



ways never intended, by targeting non-natural (serendipitous?) properties with potential applications. The results of this effort have led to more expanded funding through both the NSF (BioQubic) and the NYS Infotonics Consortium to evaluate genetically-modified bacteriorhodopsin variants as candidates for the branched-photocycle memory and as an enhanced holographic medium.

The ultimate success of the branched photocycle architecture hinges on the development of an optimized bacteriorhodopsin protein, a target that is actively being sought through the aforementioned funding and ongoing research program. The various prototypes that have been developed and described herein are ideal for evaluation of the new memory media as they become available. In addition to the those fabricated by Critical Link, a last prototype was developed within the Keck Center that has enhanced capabilities, including the ability to do a global erase *in situ*. The newest prototype, shown in Figure 3.44, combines the capabilities of the in-house developed screening devices, with the X-Y-Z translational capability of the Critical Link prototype. The combination of this device, the Critical Link prototype, and the screening devices will allow our highest screening throughput productivity to date.

With the production of optimized BR variants (as determined by initial screening and in-depth photokinetic evaluation of promising candidates), further prototype development will ensue. Implementation of (1) spatial light modulators or linear diode arrays for true parallel access (both write and read operations), (2) multiplexing techniques for improved storage density and optical throughput, and (3) more cost-effective optical and electronic elements, will be proceed once commercial viability is a more realistic possibility. Until that point, however, further prototype development is not worth pursuing.

It is worth noting that from the start of these efforts, the ultimate goal has been and remains the development of a commercially-viable technology, and the establishment of a start-up company based in Central New York. Given the advances over the last two years made possible through this project, we still view this goal as realistic. We are working on putting the infrastructure for the company, LambdaGen ©, in place and looking for venture-capital. LambdaGen © will be a Syracuse-based company to commercialize the BR-based optical memory, as well as other BR-based device architectures.

## 5.0. References

1. Popp, A., M. Wolperdinger, N. Hampp, C. Bräuchle, and D. Oesterhelt, *Photochemical conversion of the O-intermediate to 9-cis-retinal-containing products in bacteriorhodopsin films*. Biophys. J., 1993. **65**: p. 1449-1459.
2. Luecke, H., B. Schobert, H.T. Richter, J.P. Cartailler, and J.K. Lanyi, *Structure of bacteriorhodopsin at 1.55 Å resolution*. J. Mol. Biol., 1999. **291**(4): p. 899-911.

3. Druzhko, A., S. Chamorovsky, E. Lukashev, A. Kononenko, and N. Vsevolodov, *4-keto bacteriorhodopsin films as a promising photochromic and electrochromic biological material*. BioSystems, 1995. **35**: p. 129-132.
4. Vought, B.W. and R.R. Birge, eds. *Molecular electronics and hybrid computers*. Wiley Encyclopedia of Electrical and Electronics Engineering, ed. J.G. Webster. Vol. 13. 1999, Wiley-Interscience: New York. 477-490.
5. Ni, B., M. Chang, A. Duschl, J. Lanyi, and R. Needleman, *An efficient system for the synthesis of bacteriorhodopsin in Halobacterium halobium*. Gene, 1990. **90**: p. 169-172.
6. Peck, R.F., S. DasSarma, and M.P. Krebs, *Homologous gene knockout in the archaeon Halobacterium salinarum with ura3 as a counterselectable marker*. Molecular Microbiology, 2000. **35**(3): p. 667-676.
7. Lukashev, E.P. and B. Robertson, *Bacteriorhodopsin retains its light-induced proton-pumping function after being heated to 140°C*. Bioelectrochemistry and Bioenergetics, 1995. **37**: p. 157-160.
8. Spassov, V., H. Luecke, K. Gerwert, and D. Bashford, *pK(a) calculations suggest storage of an excess proton in a hydrogen-bonded water network in bacteriorhodopsin*. Journal of Molecular Biology, 2001. **312**(1): p. 203-219.
9. Tajkhorshid, E., J. Baudry, K. Schulten, and S. Suhai, *Molecular dynamics study of the nature and origin of retinal's twisted structure in bacteriorhodopsin*. Biophys. J., 2000. **78**: p. 683-693.
10. Hampp, N., *Bacteriorhodopsin: mutating a biomaterial into an optoelectronic material*. Applied Microbiology and Biotechnology, 2000. **53**(6): p. 633-639.
11. Juchem, T. and N. Hampp, *Interferometric system for non-destructive testing based on large diameter bacteriorhodopsin films*. Optics and Lasers in Engineering, 2000. **34**(2): p. 87-100.
12. Callahan, M. and B. Jerpseth, *An efficient random mutagenesis technique using an E. coli mutator strain*. Methods Mol. Biol., 1996. **57**: p. 375-385.
13. Wan, L., M.B. Twitchett, L.D. Eltis, A.G. Mauk, and M. Smith, *In vitro evolution of horse heart myoglobin to increase peroxidase activity*. PNAS, 1998. **95**(22): p. 12825-12831.
14. You, L. and F. Arnold, *Directed evolution of subtilisin E in Bacillus subtilis to enhance total activity in aqueous dimethylformamide*. Protein Eng, 1996. **9**(8): p. 719.
15. Bowie, J.U., J.F. Reidhaar-Olson, W.A. Lim, and R.T. Sauer, *Deciphering the message in protein sequences: tolerance to amino acid substitutions*. Science, 1990. **247**(4948): p. 1306-10.
16. Wen, J., X. Chen, and J.U. Bowie, *Exploring the allowed sequence space of a membrane protein*. Nature Structural Biology, 1996. **3**(2): p. 141-8.
17. Krebs, M.P., W. Li, and T.P. Halambeck, *Intramembrane substitutions in helix D of bacteriorhodopsin disrupt the purple membrane*. J Mol Biol, 1997. **267**(1): p. 172-83.
18. Anni, H., O. Nikolaeva, and Y. Israel, *Selection of phage-display library peptides recognizing ethanol targets on proteins*. Alcohol, 2001. **25**(3): p. 201-209.

19. Brust, M. and C.J. Kiley, *Some recent advances in nanostructure preparation from gold and silver particles: a short topical review*. Colloids and Surfaces A: Physicochemical and Engineering Aspects, 2002. **202**(2-3): p. 175-186.
20. Krebs, M.P., R. Mollaaghababa, and H.G. Khorana, *Gene replacement in Halobacterium halobium and expression of bacteriorhodopsin mutants*. Proceedings of the National Academy of Sciences of the United States of America, 1993. **90**(5): p. 1987-1991.
21. Whaley, S.R., D.S. English, E.L. Hu, P.F. Barbara, and A.M. Belcher, *Selection of peptides with semiconductor binding specificity for directed nanocrystal assembly*. Nature, 2000. **405**(6787): p. 665-668.
22. Dancshazy, Z. and Z. Tokaji, *Blue light regeneration of bacteriorhodopsin bleached by continuous light*. FEBS Lett., 2000. **476**(3): p. 171-173.
23. Dancshazy, Z., Z. Tokaji, and A. Der, *Bleaching of bacteriorhodopsin by continuous light*. FEBS Lett., 1999. **450**: p. 154-157.
24. Lanyi, J. and A. Pohorille, *Proton pumps: mechanism of action and applications*. Trends in Biotechnology, 2001. **19**(4): p. 140-144.
25. Birge, R.R., N.B. Gillespie, E.W. Izaguirre, A. Kusnetzow, A.F. Lawrence, D. Singh, Q.W. Song, E. Schmidt, J.A. Stuart, S. Seetharaman, and K.J. Wise, *Biomolecular electronics: Protein-based associative processors and volumetric memories*. J. Phys. Chem. B., 1999. **103**: p. 10746-10766.
26. Hampp, N., R. Thoma, D. Zeisel, and C. Bräuchle, *Bacteriorhodopsin variants for holographic pattern recognition*. Adv. Chem., 1994. **240**: p. 511-526.
27. Millerd, J.E., A. Rohrbacher, N.J. Brock, C. C.K., P. Smith, and R. Needleman, *Improved sensitivity in blue-membrane bacteriorhodopsin films*. Optics Letters, 1999. **24**(19): p. 1355-1357.
28. Tallent, J., Q.W. Song, Z. Li, J. Stuart, and R.R. Birge, *Effective photochromic nonlinearity of dried blue-membrane bacteriorhodopsin films*. Optics Letters, 1996. **21**: p. 1339-1341.
29. Tallent, J.R., J.A. Stuart, Q.W. Song, E.J. Schmidt, C.H. Martin, and R.R. Birge, *Photochemistry in dried polymer films incorporating the deionized blue membrane form of bacteriorhodopsin*. Biophys. J., 1998. **75**: p. 1619-1634.
30. Ebrey, T. and Y. Koutalos, *Vertebrate photoreceptors*. Progress in Retinal and Eye Research, 2001. **20**: p. 49-94.
31. Stuart, J.A. and R.R. Birge, *Characterization of the primary photochemical events in bacteriorhodopsin and rhodopsin*, in *Biomembranes*, A.G. Lee, Editor. 1996, JAI Press: London. p. 33-140.
32. El-Sayed, M. and S. Logunov, *On the molecular origin of the protein catalysis of the primary process in bacteriorhodopsin photosynthesis: Retinal photoisomerization*. Pure and Appl. Chem., 1997. **69**(4): p. 749-754.
33. Mathies, R., S. Lin, J. Ames, and T. Pollard, *From femtoseconds to biology: mechanism of bacteriorhodopsin's light-driven proton pump*. Annu. Rev. Biophys. Biophys. Chem., 1991. **20**: p. 491-518.
34. Becher, B.M. and J.Y. Cassim, *Improved isolation procedures for the purple membrane of Halobacterium halobium*. Prep. Biochem., 1975. **5**: p. 161-178.

35. Oesterhelt, D. and W. Stoeckenius, *Isolation of the cell membrane of Halobacterium halobium and its fractionation into red and purple membrane*. Methods Enzymol., 1974. **31**: p. 667-678.
36. Scherrer, P., M.K. Mathew, W. Sperling, and W. Stoeckenius, *Retinal isomer ratio in dark-adapted purple membrane and bacteriorhodopsin monomers*. Biochemistry, 1989. **28**(2): p. 829-34.
37. Noll, G.N. and C. Becker, *High-performance liquid chromatography of non-polar retinoid isomers*. Journal of Chromatography, A, 2000. **881**(1+2): p. 183-188.
38. Fischer, U.C., P. Towner, and D. Oesterheldt, *Light induced isomerization, at acidic pH, initiates hydrolysis of bacteriorhodopsin to bacterio-opsin and 9-cis-retinal*. Photochem. Photobiol., 1981. **33**: p. 529-537.
39. Maeda, A., T. Iwasa, and T. Yoshizawa, *Formation of 9-cis- and 11-cis-retinal pigments from bacteriorhodopsin by irradiating purple membrane in acid*. Biochemistry, 1980. **19**: p. 3825.
40. Maeda, A., I. Tatsuo, and T. Yoshizawa, *Photoreaction of the acidified form of bacteriorhodopsin and its 9-cis derivative in purple membrane at low temperatures*. Photochem. Photobiol., 1981. **33**: p. 559-565.
41. Pande, C., R.H. Callender, C.H. Chang, and T.G. Ebrey, *Resonance raman study of the pink membrane photochemically prepared from the deionized blue membrane of H. Halobium*. Biophys. J., 1986. **50**: p. 545-549.
42. Chang, C.-H., S.Y. Liu, R. Jonas, and R. Govindjee, *The pink membrane: the stable photoproduct of deionized purple membrane*. Biophys. J., 1987. **52**: p. 617-623.
43. Chung-Ho, C., R. Jonas, T.G. Ebrey, M. Hong, and L. Eisenstein, *Protonation changes in the interconversions of the pink membrane, blue membrane and purple membrane*, in *Biophysical studies of retinal proteins*, T.G. Ebrey, H. Frauenfelder, B. Honig, and K. Nakanishi, Editors. 1987, University of Illinois Press. p. 156-166.
44. Gross, R.B., *The Development, Characterization and Applications of Polymeric Films Containing Bacteriorhodopsin*. 1995, Syracuse University.
45. Czege, J. and L. Reinisch, *Photodestruction of bacteriorhodopsin*. Photochem. Photobiol., 1991. **53**(5): p. 659-66.
46. Masthay, M.B., D.M. Sammeth, M.C. Helvenston, C.B. Buckman, W. Li, M.J. Cde-Baca, and J.T. Kofron, *The Laser-Induced Blue State of Bacteriorhodopsin: Mechanistic and Color Regulatory Roles of Protein-Protein Interactions, Protein-Lipid Interactions, and Metal Ions*. Journal of the American Chemical Society, 2002. **124**(13): p. 3418-3430.
47. Li, Q., S. Bressler, D. Ovrutsky, M. Ottolenghi, N. Friedman, and M. Sheves, *On the protein residues that control the yield and kinetics of O<sub>630</sub> in the photocycle of bacteriorhodopsin*. Biophysical J., 2000. **78**: p. 354-362.
48. Cladera, J., M.L. Galisteo, M. Dunach, P.L. Mateo, and E. Padros, *Thermal denaturation of deionized and native purple membranes*. Biochim. Biophys. Acta, 1988. **943**(2): p. 148-56.
49. Muller, J., C. Munster, and T. Salditt, *Thermal denaturing of bacteriorhodopsin by X-Ray scattering from oriented purple membranes*. Biophys J, 2000. **78**(6): p. 3208-17.

50. Liu, S.Y. and T.G. Ebrey, *The quantum efficiency for the interphotoconversion of the blue and pink forms of purple membrane*. Photochem. Photobiol., 1987. **46**(2): p. 263-267.
51. Birge, R.R., B. Parsons, Q.W. Song, and J.R. Tallent, *Protein-based three-dimensional memories and associative processors*, in *Molecular Electronics*, M.A. Ratner and J. Jortner, Editors. 1997, Blackweel Science Ltd.: Oxford. p. 439-471.
52. Hampp, N., A. Popp, C. Bräuchle, and D. Oesterhelt, *Diffraction efficiency of bacteriorhodopsin films for holography containing bacteriorhodopsin wildtype BRwt and its variants BR<sub>D85E</sub> and BR<sub>D96N</sub>*. J. Phys. Chem., 1992. **96**: p. 4679-4685.
53. Wenham, S.R., M.A. Green, and M.E. Watt, *Applied Photovoltaics*. 1994, Sydney: Bridge printery.

## 6.0. Appendix: User Manual for the Protein-Based Three-Dimensional Memory Prototypes

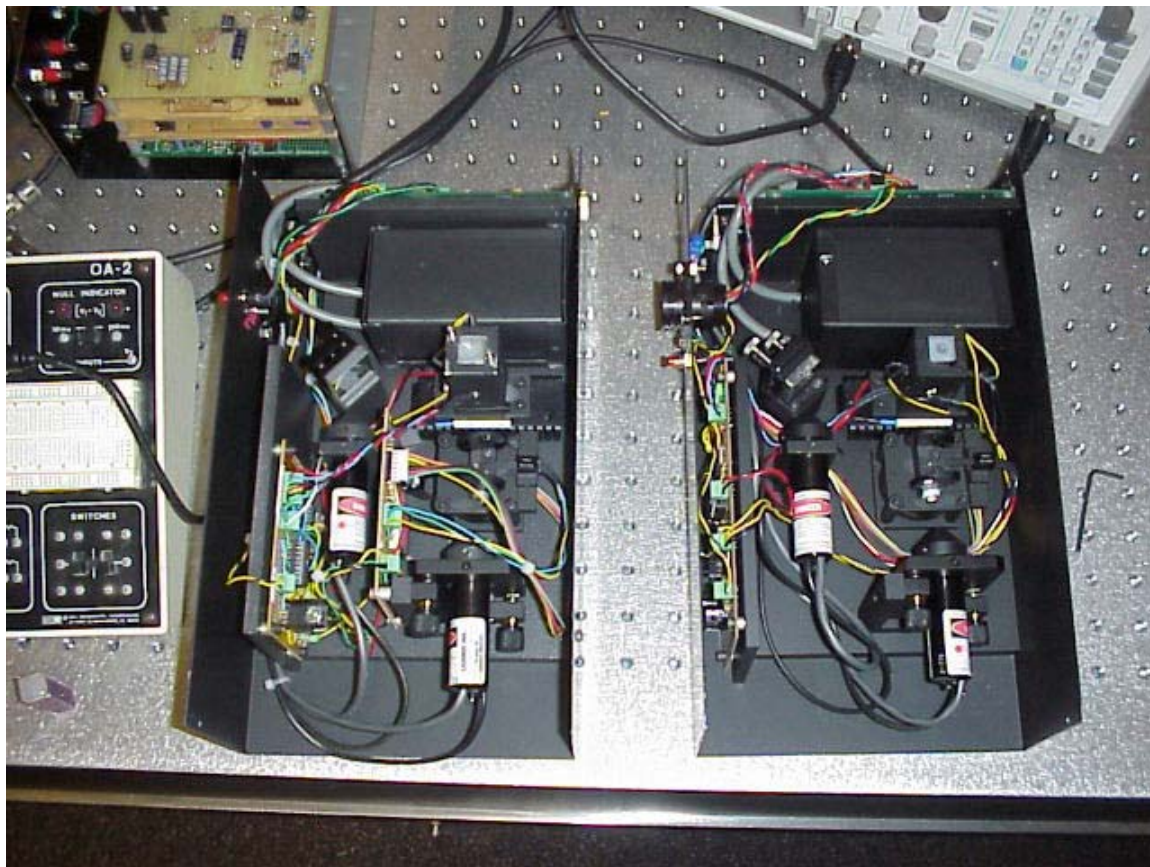


**Figure 6.1:** Bacteriorhodopsin-based three-dimensional memory screening devices developed at the W. M. Keck Center for Molecular Electronics at Syracuse University.

## Appendix Table of Contents

### Bacteriorhodopsin Three-Dimensional Memory User's Manual

- 6.1. Overview
- 6.2. Hardware Setup
- 6.3. Software Setup
  - 6.3.1. Installing the Source Code
  - 6.3.2. Running the Software
- 6.4. Aligning the Optics
- 6.5. Software Description
  - 6.5.1. Timing
  - 6.5.2. Settings
  - 6.5.3. Controls
  - 6.5.4. Model
  - 6.5.5. Advanced
  - 6.5.6. Locate
- 6.6. Hardware Description
  - 6.6.1. Mechanical/Optical Setup
  - 6.6.2. Electrical Setup
    - 6.6.2.1. Power Supply Overview
    - 6.6.2.2. System Overview
  - 6.6.3. Micro-controller board
    - 6.6.3.1. Connector Schematic
  - 6.6.4. Detector Board
    - 6.6.4.1. Schematic
    - 6.6.4.2. Board Layout
  - 6.6.5. Interface Board
    - 6.6.5.1. Schematic
    - 6.6.5.2. Board Layout
  - 6.6.6. Laser Modules
  - 6.6.7. 3-D Motion Board
    - 6.6.7.1. Schematic
    - 6.6.7.2. Board Layout
- 6.7. Communications Protocol

## 6.1. Overview for the Bacteriorhodopsin Three-Dimensional Memory User's Manual

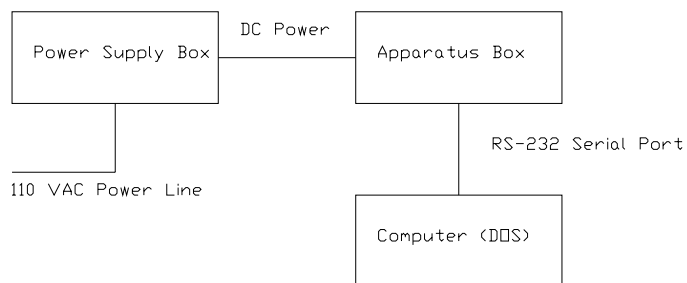
As a requirement of the contract for the protein based three-dimensional memory project, three different PC compatible external “hard drives” were assembled at Syracuse University. Two of the units are referred to as screening devices while the third is a complete three-dimensional memory system. The operation for all three instruments is identical. Each have the same hardware and embedded software, as well as driver software and the communications protocol. The difference is that commands dealing with the three-dimensional positioning of the memory medium are only operational in one of the devices (the actual memory system) The screening devices are only one-bit machines, as they have no positioning mechanism. They are intended to be used as instruments to aid in the improvement of the memory material.

## 6.2. Hardware Setup for the Bacteriorhodopsin Three-Dimensional Memory

Upon receipt of the memory unit, it must be connected to both power and a PC. Each of the memory systems is fabricated in two separate boxes. One box contains the power supply and the second contains the prototype. A short cable connects the power supply box to the prototype. A short cable connects the power supply box to the prototype. The prototype is then connected to the serial port (RS-232) of a PC (IBM type).

**Figure 6.2.** Overview of Screening Apparatus

Overview of Screening Apparatus





### 6.3. Software Setup for the Bacteriorhodopsin Three-Dimensional Memory

#### 6.3.1. Installing the Software

Once the memory system is connected to the computer the software must be installed. Microsoft QuickBasic is required in order to run the program. The Qbasic program Memory.bas on the disk that comes with the prototype must then be copied into the progs directory of the Qbasic environment. Once the file has been copied the software is ready to run.

#### 6.3.2. Running the Software

Use the Qbasic environment to open the file titled “Memory”. Then use the Qbasic start command to run the program. A prompt will appear, stating to either turn-on or re-start the memory prototype. (The re-start button is a small red button on the side of the prototype.) When a communications link is established between the PC and the prototype, the driver software will automatically start. The driver software first initializes the prototype and then it is ready for use.

### 6.4. Aligning the Optics for the Bacteriorhodopsin Three-Dimensional Memory

The memory system will **NOT** function unless the optics are aligned. To align the optics it is necessary to have a functioning memory cuvette.

Place the cube in the cube holder and go to the “Advanced” menu. Run Item 1 – Align. The software will start updating the “Blanking Voltage” variable on the screen.

The first objective when aligning is to make sure the data laser hits the photo-detector. (See Hardware Description if not familiar with these terms.) There are two thumb screws on the data laser mount that are used to position the laser beam. Adjust the two screws until the blanking voltage displayed on the screen **is maximized**. Note that the blanking voltage is displaying in graphical form as well as numerical form. When the blanking voltage is maximized, the data laser is pointed directly at the photo-detector and its position should not be changed from this point.

The second objective, which will complete the alignment, is to make the page laser beam intersect with the data laser beam. To do this the O-state trace observed on the screen must be **maximized**. To make the memory prototype start displaying the O-state trace, press the space bar. At this point, 256 read operations will occur in succession. Use the two thumb screws on the page laser mount to move the beam up and down. As the page beam crosses the data beam a signal will appear on the screen. The signal strength will be very sensitive on position as the beam diameters are only approximately 300 $\mu$ m. If the alignment process does not complete within 256 tries, simply repeat the procedure.

## **6.5. Software Description for the Bacteriorhodopsin Three-Dimensional Memory**

### **6.5.1. Executing a memory command**

Once the QBASIC program has established contact with the three-dimensional memory prototype, the program will initialize all of the internal registers in the micro-controller. The memory device is then ready to use. Across the top of the screen is the main menu. Each of these menu items is selected by pressing the letter highlighted on the screen. When a new menu item is selected, a numbered list of commands associated with that menu item is displayed on the left hand side of the screen. A command is executed by pressing the number associated with that command in the list.

All memory operations are accessed by:

1. Choosing the proper menu by pressing the appropriate letter.
2. Selecting the command by pressing the appropriate number.

For example: to turn the data laser on.

Press c (or C) to select the Controls menu.

Press 2 to toggle the data laser on.

A status window will be displayed on the screen. Within the status window it will indicate that the data laser has turned on.

Some commands require input data. When this is the case a command line appears at the bottom of the screen asking for the required information.

### **6.5.2. Timing Menu**

Commands 1–4 are associated with timing properties for writing data into the three dimensional memory. The figure below describes the write timing properties.

Commands 5-6 are associated with timing properties for reading data from the three dimensional memory. The figure below describes the read timing properties.

When one of the commands is executing a command prompt at the bottom of the screen requests the new timing data is entered in milliseconds. The status window is updated after the new time is entered.

Commands 7-9 are currently not implemented.

Command 0 is for exiting the program.

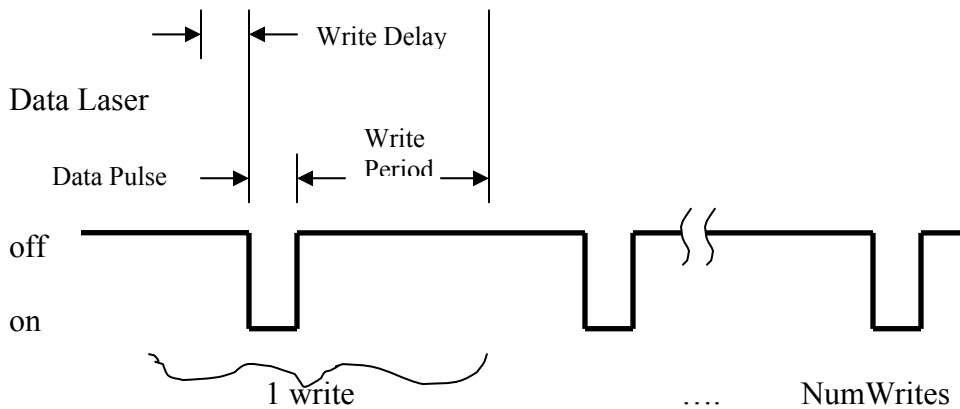
#### **6.5.2.1. Timing Menu Commands**

- 1-Page Pulse (see figure below)
- 2-Write Delay (see figure below)
- 3-Data Pulse (see figure below)
- 4-Write Period (see figure below)

Page Laser

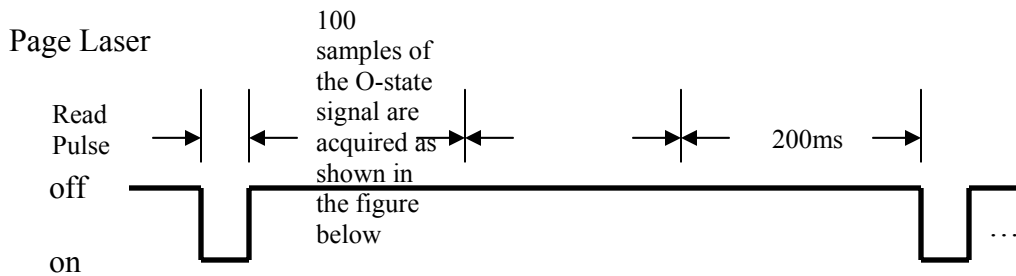


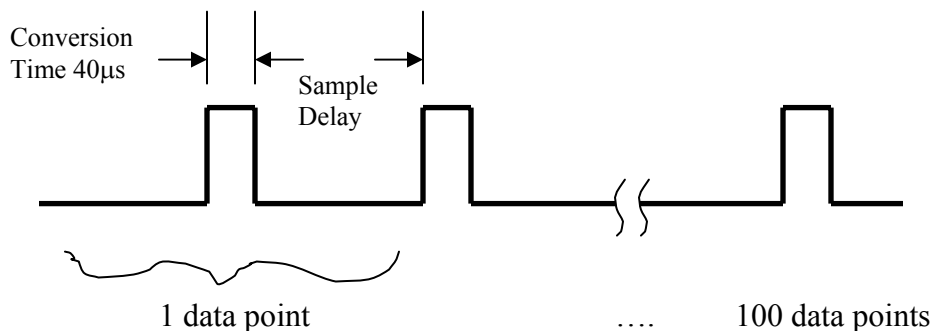
Data Laser



5-Read Pulse (see figure below)

6-Sample Delay (see figure below)





## 0-Exit Program

### 6.5.3. Settings Menu

#### 1-Gain

The gain of the O-state signal detector amplifier is selected with this command. Gain 1 is the least gain and is used for the largest signals. Gain 4 is the most gain and is used for the smallest signals. The default is gain 4. The relative gain associated with each number is as follows: 1-1, 2-2.2, 3-4.7, 4-10.

#### 2-Temp

This is the cuvette temperature entered in degrees C. The new temperature setting takes effect immediately.

#### 3-High Temp

Used for a temperature calibration routine. Not currently implemented.

#### 4-# of Writes

When a write command is executed, this is the number of write sequences that will be performed.

#### 5-# of Reads

When a read command is executed, this is the number of read sequences that will be performed.

#### 6-# of Erase

Used in association with the advanced command list. See **Advanced** commands for information.

## 7-# of Steps

Used in association with the advanced command list. See **Advanced** commands for information.

## 8-# of Seq

Used in association with the advanced command list. See **Advanced** commands for information.

### 6.5.4. Controls Menu

#### 1-Page Laser

Toggles page laser on and off.

#### 2-Data Laser

Toggles data laser on and off.

#### 3-Erase

Toggles Erase LEDs on and off.

#### 4-Filter

Moves the filter that reduces the data laser light intensity to read intensity, in or out of the way of the data laser beam.

#### 5-Averaging

Toggles averaging on and off. When a read command is executed, the read operation is repeated Number of Reads times. If averaging is on, all of these read operations are averaged on a point-by-point basis. The final result displayed is the average of Number of Read operations. If averaging is off, the data is displayed and then lost. Only the last read is left displayed on the screen. It is sometimes useful to watch the data with no averaging to see the amount of noise contained in the signal.

#### 6-Modeling

Turns modeling on or off. When modeling is on, two traces appear in the signal window. The white trace is the actual O-state data, while the purple trace is a least squares fit of a kinetics model to the data. When the error between the fit and the actual data is greater than a preset limit, that O-state trace is ignored by the data collection system. (i.e. If the purple line and white line do not match to within the tolerance, the

white line is thrown out.) In this way, modeling is used by the system as a software noise reduction technique.

The description of how the least squares fit is accomplished and how the error tolerance is set, is described in the modeling section of this chapter of the manual.

### **6.5.5. Functions Menu**

#### **1-Write**

Initiates a write sequence. A write sequence will change the spot (voxcell) in the cuvette to the P-state (binary 1 state). One write pulse first flashes the page laser and then the data laser. Repeating many write pulses (# of writes) creates a write sequence. The timing for the write pulses is described in the Timing section of this chapter and the number of writes is described in the Settings section of this chapter.

#### **2-Read Blank**

The blank voltage is an output signal from the detector amplifier. The blank voltage is different than the standard O-state signal used to monitor the memory state of the spot (voxcell) at the intersection of the two lasers. The blank voltage, or blanking voltage, has been named such because the detector amplifier functions as an auto-zeroing amplifier. What this means, is that regardless of how bright the light is hitting the detector, the O-state signal always is a transient response starting from zero volts. This allows cuvettes with different OD's to be tested without changing any settings.

Therefore, the blank voltage is simply a measure of how much light is hitting the detector when the data laser is on. Assume a voltage of 3V is returned when a Read Blank Command is executed and no cuvette is in the holder. Now, assume a cuvette is placed in the holder and a Read Blank Command returns 2V. The cuvette has a transparency of,  $T=0.67$ . If one assumes no reflection, then the cuvette has an optical density of 0.18 OD at 690nm. (690nm is the wavelength of the data laser).

#### **3-Read Temp**

The read temperature command returns the current temperature of the cuvette in degrees C.

#### **4-Read O-state**

The main determine of the binary state of the recorded memory material is determined by reading the O-state.

The following operations occur when the Read O-state command is executed. First, the filter is moved into the data beam path to produce a non-destructive probe beam from the data write laser. The data laser is then turned on and given some time to stabilize. The page laser is then pulsed while the change in probe beam light intensity is

recorded. Once the data is recorded, the integral of the O-state trace is calculated. This is repeated number of reads times. If averaging and modeling are on, the data will be handled as described in the Controls section of this chapter.

## 5-Read Data

Read data is combined command that will perform a Read Blank, Read Temp, and Read O-state.

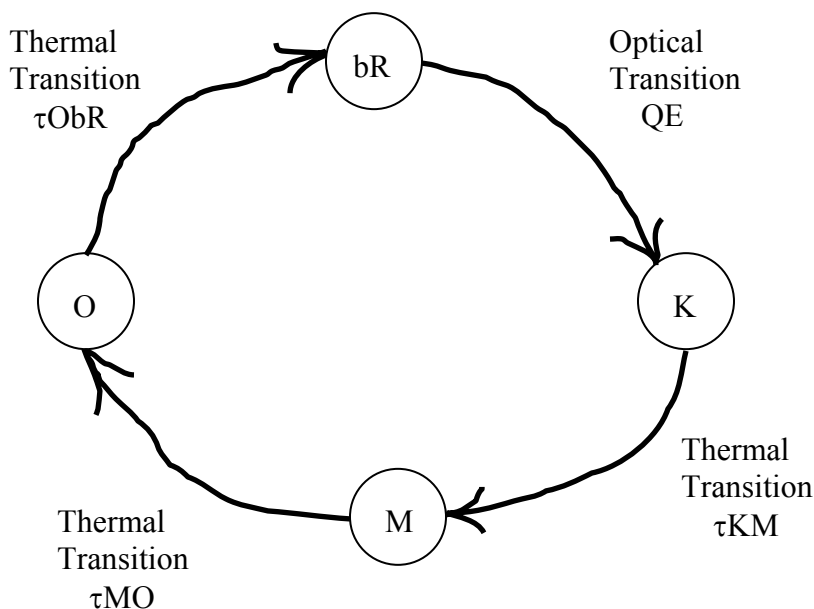
### 6.5.6. Model Menu

Modeling consists of a least squares fit to the observed O-state waveform. This section of the manual will be broken into three parts; The Model, Least Squares Fit, and Software Noise Reduction.

#### 6.5.6.1. The Model

The model is based on the kinetics diagram shown below.

**Figure 6.3:** Simplified photokinetic model of the bacteriorhodopsin photocycle.



Each of the circles represents a photochemical state of the bR material. The bR-state and the O-state are the only two states that determine the optical transmission of the cuvette at 690nm. (The wavelength of the probe data beam.) Before the page pulse is issued, it is assumed that the concentration of the material is 100% in the bR state. After the page laser is pulsed, a simple Runge-Kutta numerical algorithm is used to determine the concentration of each of the photochemical states as a function of time. Based on the concentration in each state, the transmission can be calculated as function of time. From the transmission response, the voltage response of the detector can be modeled. When

modeling is turned on, this calculation appears as a purple line along with the white line, which is the actual data observed by the detector.

The purple line will be changed by the four quantities shown in the kinetics diagram; QE,  $\tau_{KM}$ ,  $\tau_{MO}$ , and  $\tau_{ObR}$ . It will also be affected by setting the optical density of the cuvette, which determines the absolute concentration of the material in each state.

#### 6.5.6.2. Least Squares Fit

In order to accomplish a least squares fit, one can see that the terms QE,  $\tau_{KM}$ ,  $\tau_{MO}$ , and  $\tau_{ObR}$  must be adjusted until the purple line (model) matches the white line (actual data).

The real O-state waveform is always sampled 100 times across the time span chosen from the timing menu. An error term is calculated by summing the square of the difference between the purple line ( $g_i$ ) and the white line ( $y_i$ ) at each of the 100 points. The error term is then defined as

$$E = \sum_{i=1}^{100} (y_i - g_i)^2 .$$

The least squares technique requires minimizing the above equation. The minimum can be found by simultaneously solving the system of equations shown below

$$\frac{\partial E}{\partial QE} = 0, \frac{\partial E}{\partial \tau_{KM}} = 0, \frac{\partial E}{\partial \tau_{MO}} = 0, \frac{\partial E}{\partial \tau_{ObR}} = 0 .$$

The program uses Newton's method to solve the preceding system of equations. Newton's method is an iterative technique and therefore requires an initial guess. After the initial guess, the algorithm is typically repeated until the four equations above equal zero to within a specified tolerance. This program does not actually iterate over and over until there is a solution. What happens is that one iteration is performed with each read operation. Therefore, one must continue to read the cuvette to get the purple line to converge toward the white line. In Newton's method convergence is very fast once the initial guess is close. However, if the initial guess is far away, convergence will be very slow. The modeling menu allows one to update the initial guess at any time.

#### 6.5.6.3. Software Noise Reduction

The vertical axis is an eight bit digitized voltage, therefore the maximum error at each point is  $256^2$ , and the maximum total error is therefore  $100 \times 256^2$ . When the fit is not good the error is typically 100,000 to one million, while a good fit has an error less than 10,000. The error limit term in the modeling menu allows one to throw out data when the error is above the error limit.



For example, assume the number of reads is set to eight and averaging is on. Also assume the first three reads are within the tolerance of the error limit, but the fourth is not. Finally, the last four are again within the error limit. The program will only average the seven good reads. This way, out-liars can be removed from the data stream. If all eight reads do not return data within the error limit, an integral of the O-state equal to zero is returned.

#### **6.5.6.4. Modeling Menu Commands**

##### **1-570 OD**

One can specify the optical density of the cuvette at 570nm. This allows the QE term to be comparable when testing cuvettes of differing optical densities. The default is 2.

##### **2-Quantum Eff**

Allows one to enter the initial guess for the quantum efficiency (QE term) of the bR to K transition in the kinetics model shown above.

##### **3-Tau KM**

Allows one to enter the initial guess for the time constant of the K to M transition in the kinetics model shown above.

##### **4-Tau MO**

Allows one to enter the initial guess for the time constant of the M to O transition in the kinetics model shown above.

##### **5-Tau ObR**

Allows one to enter the initial guess for the time constant of the O to bR transition in the kinetics model shown above.

##### **6-Error Limit**

Allows one to enter the amount of error above which data is thrown out.

#### **6.5.7. Locate Menu**

The locate menu is only useful on the memory prototype that includes the three-dimensional positioning motors for obvious reasons. This menu will be inactive for the two screening systems that do not have positioning motors. The commands may be executed without error, although nothing will happen.

## **1-Choose Motor**

Only one motor may be operated at a time, and this command allows selection. The x-direction is parallel to the page laser beam and the y-direction is parallel to the data laser beam. The z-direction, up and down, is perpendicular to both laser beams. Selecting no motor turns all the motors off. When a motor is left on, it will heat up, so it is good practice to turn the motors off when not in use.

## **2-Direction**

The direction applies to all three motor axes. “Left” means toward the home position. The home position is found by moving the motor until a limit switch is hit. When the limit switch is hit, the motor simply stops moving in the “left” direction. “Right” means away from the home position. There is no limit switch in this direction, the motor screw will simply unthread and the cuvette will stop. The motor screw may have to be rethreaded by hand. To prevent this problem do not go more than 1200 steps from home in the “right” direction. This applies to all three motor axes.

## **3-# of Motor Steps**

This is the number of steps a motor will make when the move cuvette command is issued. Each step is approximately 25 $\mu$ m.

## **4-Move Cuvette**

When this command is issued, the cuvette will move along the chosen axis, in the chosen direction, for the chosen number of steps.

## **5-Find Home**

This command will automatically move the cuvette to the limit switches for all three axes.

## **6.5.8. Advanced Menu**

The advanced commands are not basic commands that the memory system executes, but are a series of basic commands strung together to perform a specific task using the memory.

### **1-Align**

The command is used to align the lasers. There is a separate chapter in this manual that explains the details of the alignment procedure using this command. See that chapter for a description of the functionality of this command.

## 2-Temp Test

Executing this command creates the data file: **tempdata.dat**

The following algorithm describes how the tempdata.dat file is created.

```
Set temperature setpoint to 25°C
FOR i = 1 to 15
    Record temperature data in file
    Wait 1 minute
NEXT i
Set temperature setpoint to 45°C
FOR i = 1 to 30
    Record temperature data in file
    Wait 1 minute
NEXT i
Set temperature setpoint to 25°C
FOR i = 1 to 30
    Record temperature data in file
    Wait 1 minute
NEXT i
```

The data file has a list of temperatures and if plotted, this graph can be used to tune the PI temperature controller. This task has been performed and the temperature control coefficients are hard coded in the 3D memory system.

## 3-Read Test

Executing this command creates the data file: **readdata.dat**

The following algorithm describes how the readdata.dat file is created.

```
FOR i = 1 to NumSeq
    Read the cuvette and record the Integral of the O-state
    as well as the modeling information
    Wait 1 minute
NEXT i
```

The data file can be used to create a histogram of the Integral of the O-state. This will allow one to determine the noise statistics associated with reading a 3D bit within the cuvette.

## 4-Erase Test

Executing this command creates the data file: **erasedata.dat**

The following algorithm describes how the erasedata.dat file is created.

```
FOR i = 1 to NumSeq
  Turn on the Erase LEDs for 5 minutes
  Read the cuvette and record the Integral of the O-state
  as well as the modeling information
NEXT i
```

This information can be used to determine the time constant associated with the erase photochemistry to insure complete erasure is performed during other experiments. It can also be used to form a completely erased cuvette.

#### 5-FF DF

Executing this command creates the data file: **FFDF.dat**

The following algorithm describes how the FFDF.dat file is created.

Read the cuvette and record the Integral of the O-state  
as well as the modeling information

```
FOR i = 1 to NumSeq

  FOR j = 1 to NumStep
    Perform a standard write command (sequential flash)
    Read the cuvette and record the Integral of the O-state
    as well as the modeling information
  NEXT j

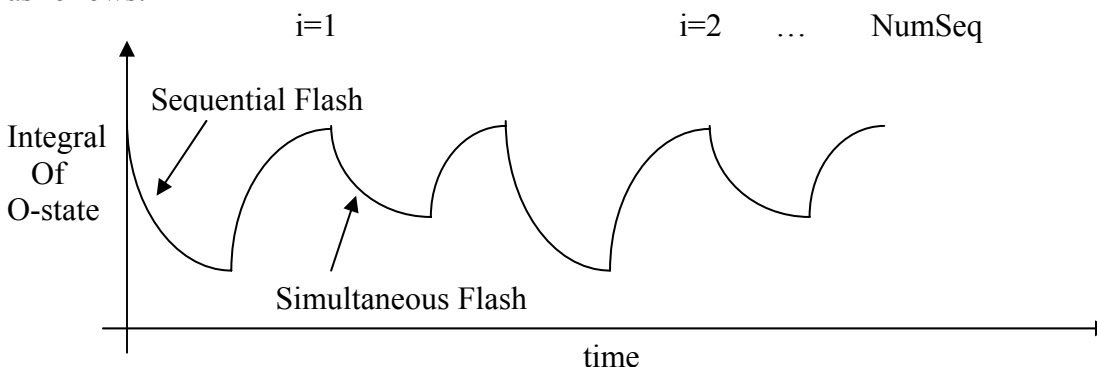
  FOR j = 1 to NumErase
    Turn on Erase LEDs for 2 minutes
    Read the cuvette and record the Integral of the O-state
    as well as the modeling information
  NEXT j

  FOR j = 1 to NumStep
    Perform a write command with both lasers
    pulsing at the same time (simultaneous flash)
    Read the cuvette and record the Integral of the O-state
    as well as the modeling information
  NEXT j

  FOR j = 1 to NumErase
    Turn on Erase LEDs for 2 minutes
    Read the cuvette and record the Integral of the O-state
    as well as the modeling information
  NEXT j
```

NEXT i

The data recorded the file can be plotted versus time to reveal a plot that appears as follows:



From this plot one can determine the time constant associated with a standard write as well as the size of the read signal. The simultaneous flash portion of the plot has significance in that the same exact number of write photons expose the material as do in the sequential flash portion of the plot. However, if the writing that occurs during the simultaneous flash is less than during the sequential flash then branched photochemistry must exist. The degree of branched photochemistry can be determined by comparing the sequential flash time constant to the simultaneous flash time constant. The erase time constant can also be observed in the plot.

## 6-Unwanted

Executing this command creates the data file: **unwanted.dat**

The following algorithm describes how the unwanted.dat file is created.

Read the cuvette and record the Integral of the O-state  
as well as the modeling information

FOR i = 1 to NumSeq

FOR j = 1 to NumStep

Perform a standard write command (sequential flash)  
Read the cuvette and record the Integral of the O-state  
as well as the modeling information

NEXT j

FOR j = 1 to NumErase

Turn on Erase LEDs for 2 minutes  
Read the cuvette and record the Integral of the O-state  
as well as the modeling information

NEXT j

```

FOR j = 1 to NumStep
    Perform a write with the page laser only
    Read the cuvette and record the Integral of the O-state
    as well as the modeling information
NEXT j

FOR j = 1 to NumErase
    Turn on Erase LEDs for 2 minutes
    Read the cuvette and record the Integral of the O-state
    as well as the modeling information
NEXT j

FOR j = 1 to NumStep
    Perform a write command with both lasers
    pulsing at the same time (simultaneous flash)
    Read the cuvette and record the Integral of the O-state
    as well as the modeling information
NEXT j

FOR j = 1 to NumErase
    Turn on Erase LEDs for 2 minutes
    Read the cuvette and record the Integral of the O-state
    as well as the modeling information
NEXT j

FOR j = 1 to NumStep
    Perform a write command with the data laser only
    Read the cuvette and record the Integral of the O-state
    as well as the modeling information
NEXT j

FOR j = 1 to NumErase
    Turn on Erase LEDs for 2 minutes
    Read the cuvette and record the Integral of the O-state
    as well as the modeling information
NEXT j

NEXT i

```

This command performs the same experiment as above, but includes writing with only one laser at a time. This allows for the determination of the amount of unwanted photochemistry associated with individual lasers.

## 7-One bit Map

A map command creates a file that stores the Integral of the O-state on a 25x25 grid along a plane in the memory cuvette. The map plane is formed by the page and data laser beams. The map commands can only be executed on the 3D memory system and not the screening systems.

Executing this command creates the set of data files:

**XYmapi.dat, i=0 to NumSeq**

The following algorithm describes how the XYmapi.dat files are created.

```
FOR i = 1 to NumSeq
  Write a bit in the center of the map
  Read the cuvette and record a map of the Integral of the O-state
NEXT i
```

The files may be plotted as contour plots showing the formation of a bit in the center of the cuvette.

#### **8-Four Bit Map**

Executing this command creates the set of data files:

**XYmapi.dat, i=0 to NumSeq**

The following algorithm describes how the XYmapi.dat files are created.

```
FOR i = 1 to NumSeq
  Write four bits, forming a square in the center of the map
  Read the cuvette and record a map of the Integral of the O-state
NEXT i
```

The files may be plotted as contour plots showing the formation of four bits, one behind the other on the axis of each laser beam.

#### **9-FFDF Map**

Executing this command creates the set of data files:

**FFmapi.dat; FEmapi.dat DFmapi.dat DEmapi.dat, i=0 to NumSeq**

The following algorithm describes how the FFDF.dat file is created.

Read the cuvette and record the Integral of the O-state  
as well as the modeling information

```
FOR i = 1 to NumSeq
```

```
  Read the cuvette and record a map of the Integral of the O-state
```

```

FOR j = 1 to NumStep
    Perform a standard write command (sequential flash)
NEXT j

Read the cuvette and record a map of the Integral of the O-state

FOR j = 1 to NumErase
    Turn on Erase LEDs for 2 minutes
NEXT j

Read the cuvette and record a map of the Integral of the O-state

FOR j = 1 to NumStep
    Perform a write command with both lasers
    pulsing at the same time (simultaneous flash)
NEXT j

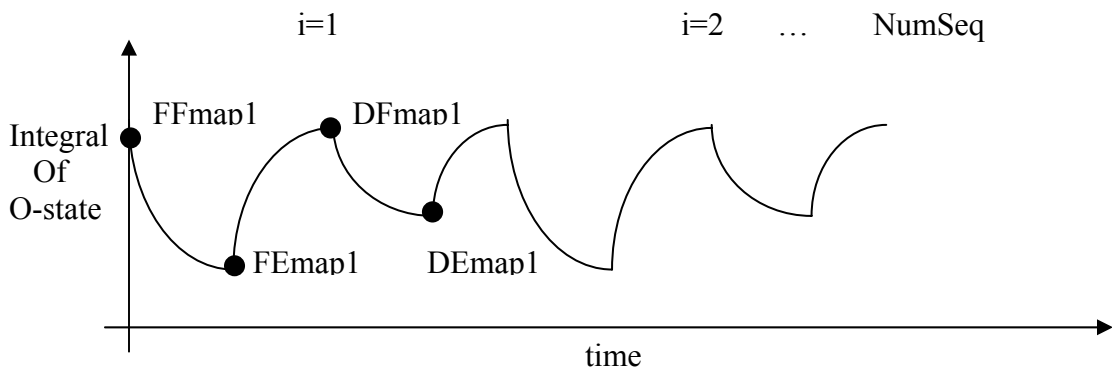
Read the cuvette and record a map of the Integral of the O-state

FOR j = 1 to NumErase
    Turn on Erase LEDs for 2 minutes
NEXT j

NEXT i

```

The data recorded the file can be plotted versus time to reveal a plot that appears as follows:



From this plot one can see a contour plot of the bit forming and then disappearing.

## 6.6. Hardware Description for the Bacteriorhodopsin Three-Dimensional Memory

### 6.6.1. Mechanical/ Optical Setup

The mechanical/optical layout of the Screening Apparatus is shown below



## Mechanical and Optical Layout of Screening Apparatus

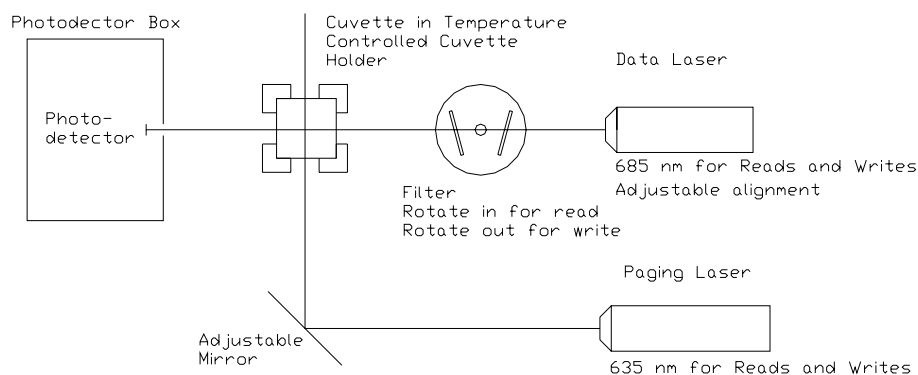


**Figure 6.4:** Mechanical and Optical Layout of the Screening Apparatus

The data laser is mounted in an adjustable mount. The light from the data laser goes through the Cuvette and hits the detector on the detector board. The data laser adjustable mount is used to align the laser correctly. The focus of the laser is set so the smallest part of the beam is where the detector is hit. A filter is mounted between the laser and the cuvette. The filter is designed with two neutral density filters. The filters are mounted on a stepper motor. The stepper motor is used to move the filter in and out of the way of the data laser light. The filter is in during read operations and out during write operations. The filters are mounted at a small angle to the light path. This reduces reflected light that goes back into the laser, reducing laser noise.

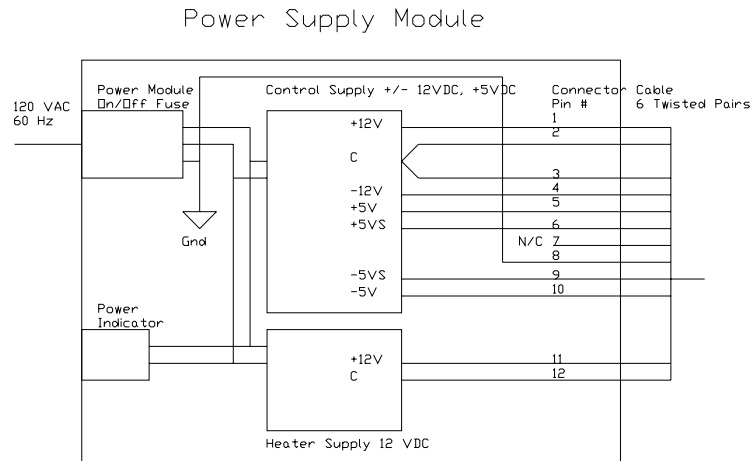
The page laser is mounted on a fixed mount. The light is reflected off a mirror with an adjustable mount and passes through the cuvette. The adjustable mount of the mirror is used to align the beam so that the beams intersect in the center of the cuvette. The focus of the laser is adjusted so at the intersection point the page laser beam size is the same as the data laser beam size.

Temperature control of the cuvette is attained using a Peltier Device to heat the cuvette holder. The Peltier Device is mounted between the Cuvette holder and the base plate. The orientation of the Peltier Device is such that the heat is moved from the base into the cuvette holder. The temperature of the cuvette holder is measured using a sensor (LM35DZ) set in the cuvette holder. A Peltier Device is used because originally the plan was to heat and cool the cuvette. After it became clear that the bR worked best at about 40 C only heating was used.

The cuvette 3-D motion system (3-D memory only) has a 3-D motion system for the cuvette. The motion system has three stages set perpendicular to each other. Each

stage is moved by a stepper motor. Each stage has a limit switch in one direction. When the cuvette is moved so the limit switches are closed is defined as the home position. The range of motion in each direction is 1 centimeter.

**Figure 6.5:** Power supply module.



## 6.6.2. Electrical Setup

### 6.6.2.1. Power Supply Overview

The Power Supply Box provides regulated DC power for the prototypes. The power supply box is connected to 110VAC. The Power Supply Box has an on/off switch, fuses and an indicator light. Within the box are two power supplies. The first supply (ASTECH ATV251) provides +5V at 2.0A, +12V at 0.4A and -12V at 0.4A. This supply is used for analog and digital electronics (except the Interface Board) and to power the two laser modules. The second supply (ASTECH ATV 12N3.4) provides +12V at 3.4A. This supply is used for the Interface Board, the 3-D Motion Interface Board (3-D memory only), the heater, the erase LED's, and all stepper motors.

### 6.6.2.2. System Overview

The Screening Apparatus and the 3-D Memory prototypes are each contained in a box. The outputs of the boxes are a RS-232 Serial Port and a Power Connector. Within the box are all of the components of the prototypes.

A microcontroller board interfaces with the computer. The microcontroller receives commands from the computer and runs the prototype. Below is a system diagram for the prototypes.

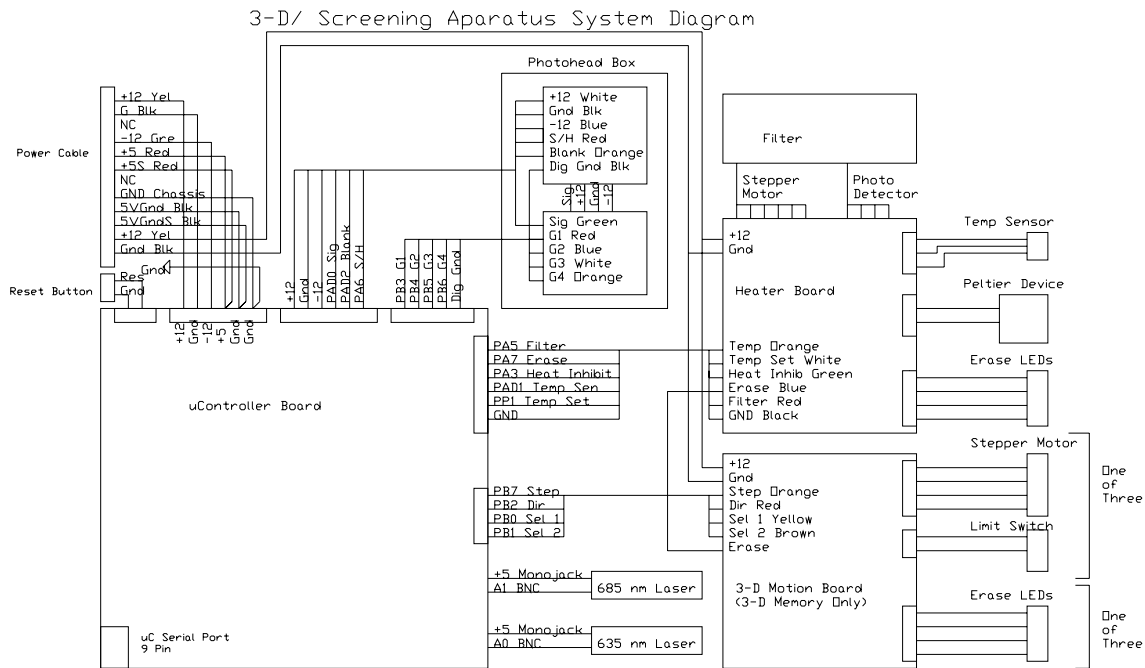


**Figure 6.6:** Prototype system diagram.

### 6.6.3. Microcontroller Board

The microcontroller board is a M68EVB912B32. This is an evaluation board for the Motorola M68HC12B microcontroller (16 bit). The board has a built in RS-232 Serial Port. The power required is +5V. This board receives commands from the PC and based on these commands sends and receives data from the other boards and the Laser Modules. Reset of the board is through an on board push button or a push button on the box. The controls are implemented as follows:

Laser Module – Each of the Laser Modules (Data Laser 685nm, Page Laser 635 nm) is directly controlled by the Microcontroller. Power to the Modules is from the +5V supply that powers the microcontroller board. The power is connected via a 3.5mm audio jack. Control of the lasers is from the microcontroller (pin PA0 for the Data Laser and PA1 for the Page Laser. The control signals go through BNC connectors.

Interface Board – The Interface Board is connected to the Microcontroller board via a cable. Control lines and there function are as follows:

PA7 Erase - This turns the erase LED's on and off. LED's are connected in two sets of two LED's. The LED's are 430 nm and are arranged on the cuvette holder to illuminate the portion of the cuvette where writing takes place.

PA5 Filter – This controls the filter moving it in or out of the Data Laser beam path.

PA3 Heat Inhibitor - This turns the heater off to prevent noise during reads.

PAD1 Temperature – This has an analog signal of the cuvette holder temperature. The signal is 50mV/C.

PP1 Temperature Set – This is a PWM Signal from the microcontroller that provides the set point for the temperature controller. The signal is filtered (low pass) and is 50 mV/C.

GND – This provides a common ground for the two boards.

Detector Board – The Microcontroller board is connected to the Detector Board via two cables. Connections are as follows:

Power – Power to the Detector Board is +12V, GND and –12V.

PAD2 Blank Signal – This is an analog signal representing the steady state laser power received by the detector board. This signal is read by the ADC on the microcontroller.

PAD0 Signal – This is an analog signal representing the absorption change in the bR due to O-state. This signal is read by the ADC on the microcontroller.

PA6 S/H – This is a control going to the detector board.

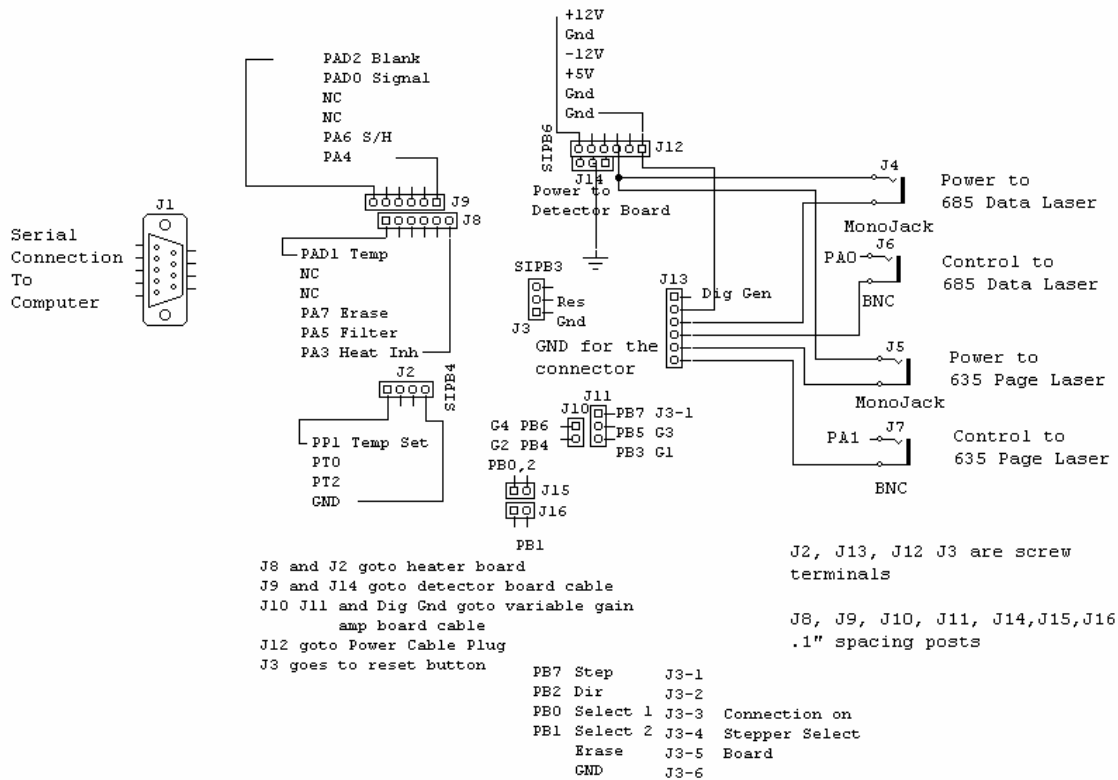
PB3, PB4, PB5, PB6 Gain control. This is a control going to the detector board. This controls the gain of the signal (range of 1-10).

3-D Motion Interface Board – The Microcontroller Board is connected to the 2-D Motion Interface Board via one cable. Connections are as follows:

PB7 Step – This is a pulsed signal that moves the selected stepper one step per pulse.

PB2 Direction – This is the direction of the selected stepper.

PB0, PB1 Select 1 and 2 – These control which of the three steppers is selected (0,0 is all steppers off).



### 6.6.3.1. Connector Schematic

Figure 6.7: Connector Schematic

#### 6.6.4. Detector Board

The Detector Board (actually two boards) is used in read operations. Light from the data laser passes through a pair of neutral density filters, reducing its intensity by a factor of 250. The light then passes through the cuvette with the bR. The detector board has a photodiode, with a built in amplifier. The light hits a photodiode on the detector board. The photodiode is in an IC with a built in op amp in a transimpedance configuration. With an external resistor the gain of the op amp is set to 10 million. The output of the photodiode amp is sent to an integrator. The output of the integrator is feed back into the photodiode IC through a sample and hold IC. The feedback is used to provide a blanking signal to the photodiode. In operation, the laser is turned on, and the integrator increases the output until the signal going to the photodiode is zero. The sample and hold is turned to hold and the page laser is pulsed. The output from the photodiode op amp is proportional to the change in absorbency due to the presence of O-state in the bR. The second detector board has a selectable gain amp. The gain choices are 1, 2, 5 and 10. The signal from the selectable gain amp and the blanking signal are sent to the microcontroller for analog to digital conversion.

The detector boards are housed in a separate small aluminum box to reduce noise.

#### 6.6.4.1. Detector Board Schematic (Part 1)

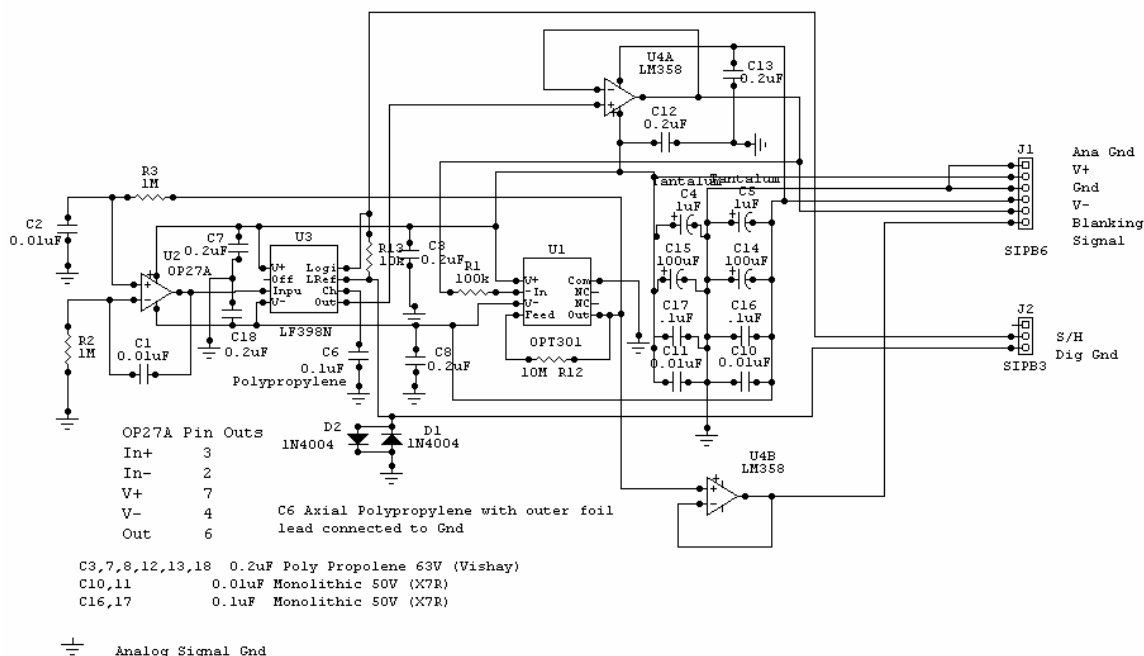
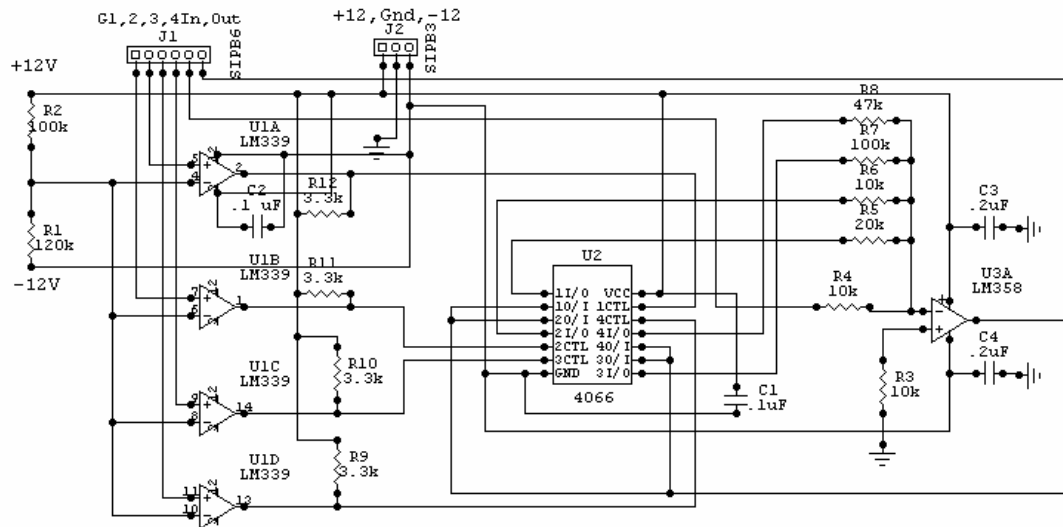
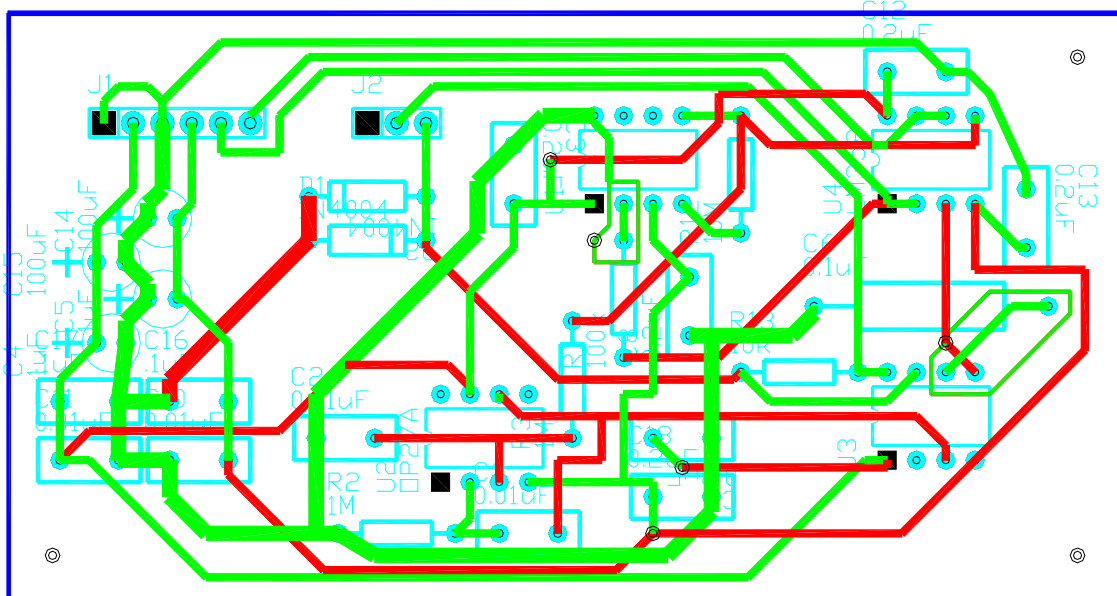


**Figure 6.8:** Detector Board Schematic (Part 1)

**Figure 6.9:** Detector Board Layout (Part 1)



Variable Gain Amp used with the Photo Head.  
Signal is amplified and inverted. Gains are 1,2,4,7,10.



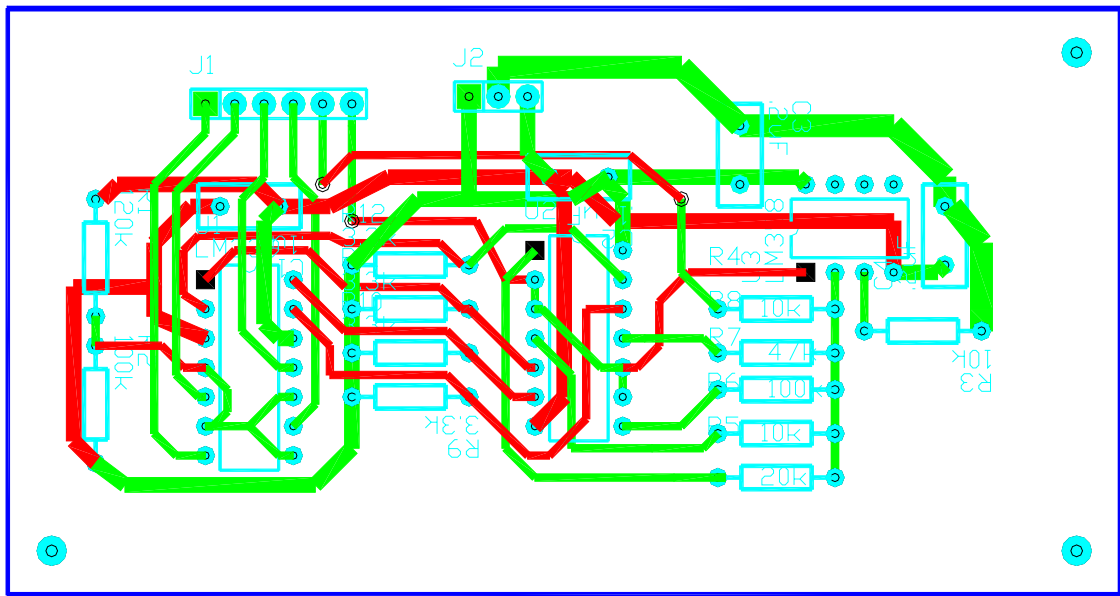


**Figure 6.10:** Detector Board Schematic Circuit Views (Part 2).



### 6.6.5. Interface Board

This board controls the filter, the erase LED's, and the Cuvette temperature. The board is provided with 12V and 5V is generated on board.

The filter has two neutral density filters mounted on a stepper motor assembly. There is an optosensor that indicates when the filters are in position. The Interface Board has a PIC microcontroller (PIC16F84) that has as inputs, the control line from the Microcontroller board (0 for filter out and 1 for filter in) and the optosensor (0 for filter out and 1 for filter in). There are four outputs that control the stepper motor through a darlington array. When the input signal is changed to 1, the stepper motor is rotated clockwise until the optosensor returns a 1 (the filter is in place and attenuates the data laser). When the input signal is changed to 0, the stepper is rotated 90 degrees counter clockwise (the filter is out of the way of the data laser).

The erase LED circuit is designed to ensure that when the LED's are off, there is no current going to them at all. The circuit is capable of controlling 4 LED's. The LED's are connected in sets of two LED's in series.

The Cuvette temperature is controlled by a PIC microcontroller (PIC16C71). The microcontroller has three inputs (set temperature, actual temperature and heater inhibit). The set temperature comes from the microcontroller board as a PWM signal. This signal is filtered and buffered before being sent to the PIC. The signal is 50 mV per degree. The temperature of the Cuvette is measured by a LM35DZ (10 mV per degree). The signal is amplified by a factor of 5 (50 mV per degree) then input into the PIC. The heater inhibit turns the heater off during read cycles to prevent noise in the signal. There is one output, a PWM signal (1 second frequency) that controls the heater.

The PIC has an onboard A to D converter. This converts the set temperature and the actual temperature. The difference between the set temperature and the actual temperature is used in a PI controller. The PI controller drives the PWM signal output. The PWM signal controls a Darlington Power Transistor that powers a Peltier Device. The Peltier Device heats the cuvette holder and cuvette and is mounted under the cuvette holder.



#### **6.6.6. Laser Modules**

The laser modules used are the LASIRIS DLS-500-635-15 (15 mW page laser) and the DLS-500-685S-50 (35 mW data laser). These lasers operate on 5V DC and are controlled by a TTL input (0 on and 1 off). The inputs for the lasers comes directly from the microcontroller board. The two lasers are aligned so that the beams intersect in the center of the cuvette. The distance from the laser to the center of the cuvette is the same for each laser. The data laser is focused on the photodiode. The page laser is focused for the same distance as the data laser. This way, where the beams intersect the laser beams are the same size.

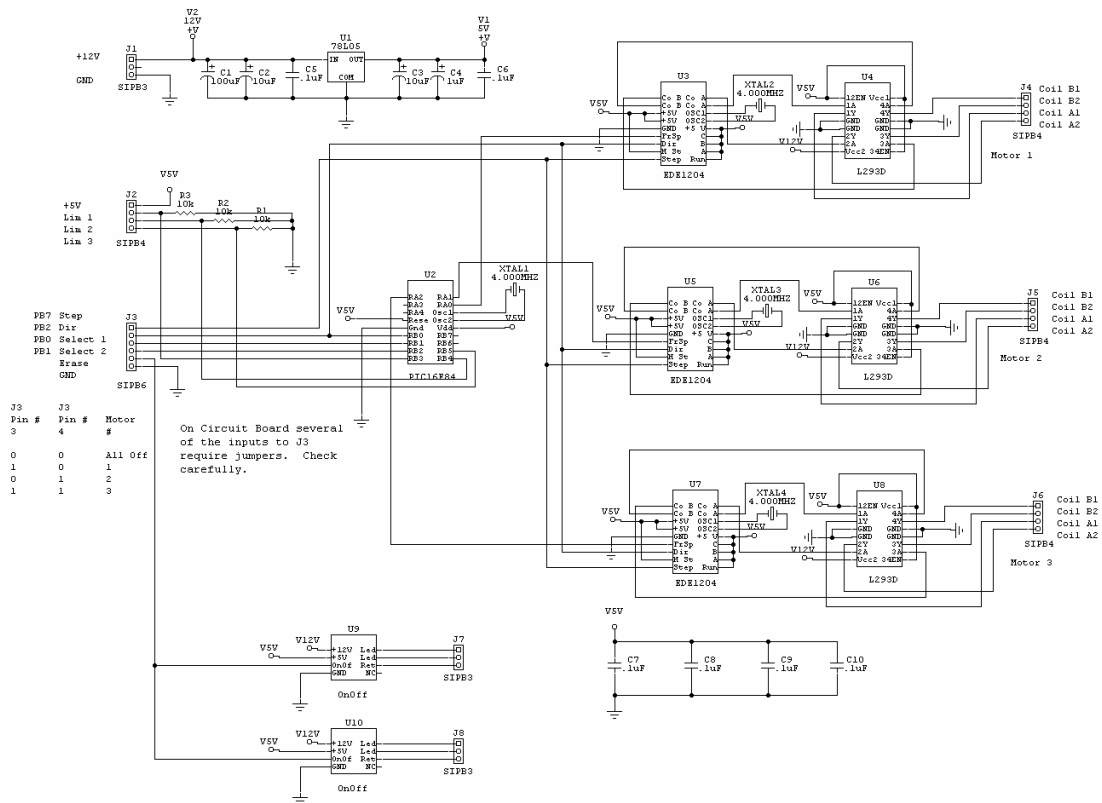
#### **6.6.7. 3-D Motion Interface Board (3-D Memory only)**

This board is used to control the 3 stepper motors used in the Cuvette 3-D Motion system. In addition, circuitry is provided to power 8 erase (blue) LED's. The board is supplied with 12V and generates 5V on the board.

The 3-D motion control system has inputs from the microcontroller board. These inputs select the stepper motor to be driven, the direction of travel and one pulse for each step to be taken. Limit switches are used to indicate when the Cuvette Holder is in the home position (the home limit switches are used only on the board, no information regarding the home position is returned to the microcontroller board). The board uses a microcontroller (PIC16F84) to direct the incoming step commands to the proper stepper motor controller. This controller also receives input from the limit switches and when a switch is activated motion is only allowed in the direction away from the switch. Each stepper motor is controlled by an EDE1204 (a PIC based commercial stepper motor controller) which operates an H-bridge power IC that runs the stepper motors. The stepper motors are powered by 12V and the control circuitry is 5V.

The erase LED's are powered by 2 copies of the circuit that is used on the Interface Board. Input for these LED's comes from the Microcontroller Board via the Interface Board. A total of 8 LED's can be powered by this board. Additional LED's are used in the 3-D Memory to ensure that all of the Cuvette is illuminated, rather than just the center point as in the screening device.

See next page.



c:\My Documents\WCT\3dmem\ed stepper select.ckt

This circuit is for use in 3d memory. It selects the stepper motor (X,Y or Z) that is used. Also included are two on off switches for Blue LEDs.

**Figure 6.12: 3-D Motion Interface Board Schematic**

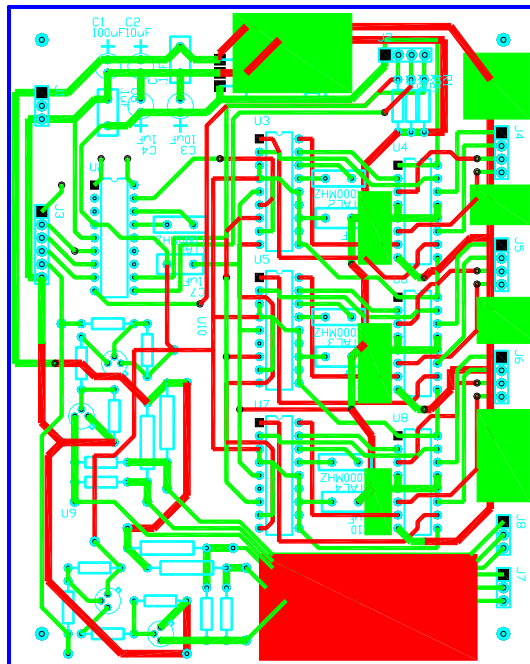


**Figure 6.12:** 3-D Motion Interface Board Circuit View

## 6.7. Communications Protocol for the Bacteriorhodopsin Three-Dimensional Memory

The following section describes the protocol for communicating to the three-dimensional memory from the host computer. There are fourteen commands that can be sent to the memory. The three-dimensional memory's embedded software interprets these commands and performs the appropriate action.

Communication takes place over a standard RS232 interface. The three-dimensional memory is set to 9600 baud and 8 data bits.

### Command 0: Store the Number of Writes

Stores the number of writes to be performed when a write command is given.

Format:        0, High byte, Middle byte, Low byte

Example:

```
NumWrites = 100,000
H = INT( NumWrites / 65536 )           ( H = 1 )
M = NumWrites - H * 65536              ( M = 34464 )
M = INT( M / 256 )                     ( M = 134 )
L = NumWrites - H * 65536 - M * 256     ( L = 160 )
PRINT #1, CHR$(0); CHR$(H); CHR$(M); CHR$(L);
```

### Command 2: Store an internal variable

Stores a two-byte variable into the 3D Screening Spectrometer's set-up area.

Format:        2, variable #, High byte, Low byte

Variable # Reference List:

0	-	Page Pulse Duration
2	-	Write Pulse Duration
4	-	Write Delay
6	-	Write Period
8	-	Read Pulse Duration
10	-	Sample Delay
12	-	Number of Reads

Example 1:

```

WrPlsDur = 2.3E-3 ( Set to 2ms )
WrPlsCount = INT( WrPlsDur / 4E-6 ) ( Each count is 4µs )
                                         ( WrPlsCount = 575 )
H = INT( WrPlsCount / 256 ) ( H = 2 )
L = WrPlsCount - H * 256 ( L = 63 )
PRINT #1, CHR$(2); CHR$(2); CHR$(H); CHR$(L);

```

Example 2:

```

NumReads = 500
H = INT( NumReads / 256 ) ( H = 1 )
L = NumReads - H * 256 ( L = 244 )
PRINT #1, CHR$(2); CHR$(12); CHR$(H); CHR$(L);

```

#### **Command 4: Select Analog Signal**

Chooses which signal is sent back to the computer when an Analog (Command 20) or Read (Command 22) is issued.

Format: 4, 0, Signal

Signal List:

0	-	Analog Signal
2	-	Temperature
4	-	Blanking Signal

Example:

```

PRINT #1, CHR$(4); CHR$(0); CHR$(2); ( Set up to read the temperature )

```

#### **Command 6: Set Temperature**

Set the cuvette temperature.

Format: 6, 1, TempNum

Temperature Scaling:

TempNum is a byte, which can take on the values ( 0 – 255 ). The number sent to the 3D Screening Spectrometer is the temperature in degrees C divided by 0.4275

Example:

```
Temperature = 40                                ( 40 degrees C )  
TempNum = INT( Temperature / 0.4275 )          ( TempNum = 93 )  
PRINT #1, CHR$(6); CHR$(1); CHR$(TempNum);
```

## Command 8: Write

Issue a write command to the 3D Screening Spectrometer.

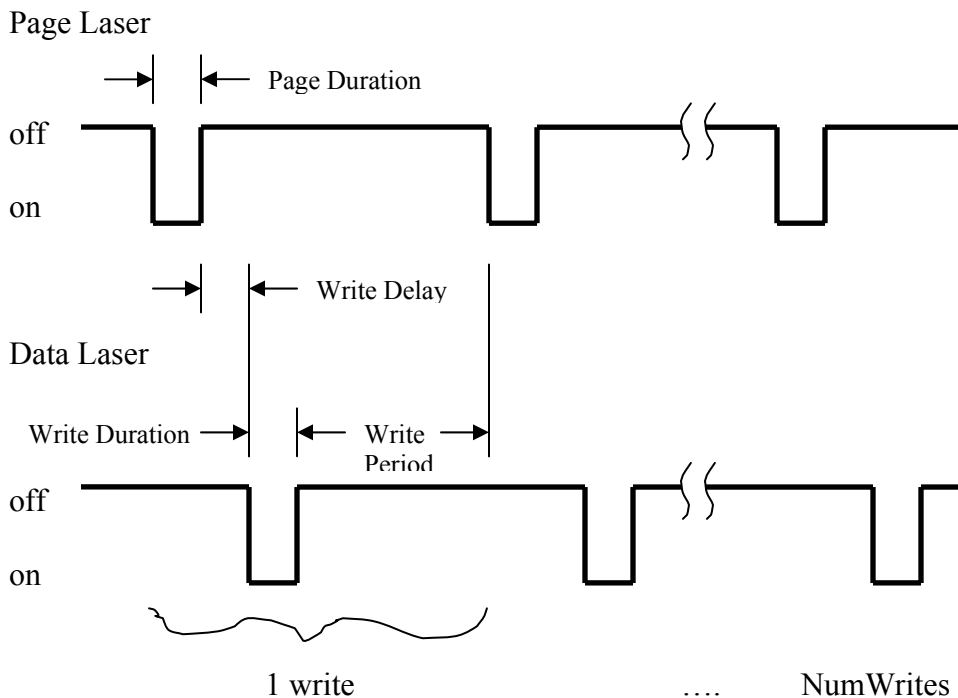
Format: 8, 1, 18

Return: W

Because the time for a write sequence to occur is programmable (from milliseconds to hours), timing is handled by a handshake protocol. Upon completion of the write command the 3D Screening Spectrometer will return a **W** (ASCII 87) to the host computer.

Timing:

The timing is generated by values contained in the internal variables list (Command 2). The variables of interest are Page Pulse Duration, Write Pulse Duration, Write Delay and Write Period. The diagram below summarizes the timing details.





Example:

```
PRINT #1, CHR$(8); CHR$(1); CHR$(18);      ( Start Write )
DO                                           ( Wait for W )
  AI$ = INPUT$(LOC(1), #1)
  IF AI$ = "W" THEN EXIT DO
LOOP
```

#### **6.7.1. Advanced Write Format:**

a more complex arrangement of laser pulses can be issued using the write command. The write command format is more completely specified as: 8, pulse1, pulse2. For a standard write operation pulse1 = 1 and pulse2 = 18. The details for the advanced meaning of pulse1 and pulse2 are given in the Pulse (Command 10) section below.

### **Advanced Command 8: Write**

Format:        8, pulse1, pulse2

Return        W

Issue a non-standard write command to the 3D Screening Spectrometer. Pulse1 and Pulse2 are described in the Pulse (Command 10) section below.

Example 1:

The first pulse is page laser for page duration and the second pulse is data laser for write duration. (A standard write.)

```
PRINT #1, CHR$(8); CHR$(1); CHR$(18);      ( Start Write )
DO                                           ( Wait for W )
  AI$ = INPUT$(LOC(1), #1)
  IF AI$ = "W" THEN EXIT DO
LOOP
```

Example 2:

The first pulse is both lasers for page duration and the second pulse is no lasers for write duration.

```
PRINT #1, CHR$(8); CHR$(3); CHR$(16);      ( Start Write )
DO                                           ( Wait for W )
  AI$ = INPUT$(LOC(1), #1)
  IF AI$ = "W" THEN EXIT DO
LOOP
```

By first issuing a write command as in example 1, erasing the bit produced by this process, and then issuing a write command as in example 2, the famous sequential flash versus simultaneous flash experiment is accomplished.

### **Command 10: Pulse Laser**

Pulses the Page laser and the Data laser.

Format:        10, pulse

Pulse instruction set:

- |    |   |                                |
|----|---|--------------------------------|
| 0  | - | No lasers for Page Duration    |
| 1  | - | Page laser for Page Duration   |
| 2  | - | Data laser for Page Duration   |
| 3  | - | Both lasers for Page Duration  |
| 16 | - | No lasers for Write Duration   |
| 17 | - | Page laser for Write Duration  |
| 18 | - | Data laser for Write Duration  |
| 19 | - | Both lasers for Write Duration |
| 32 | - | No lasers for Read Duration    |
| 33 | - | Page laser for Read Duration   |
| 34 | - | Data laser for Read Duration   |
| 35 | - | Both lasers for Read Duration  |

Example 1:

PRINT #1, CHR\$(10); CHR\$(1);    ( Pulse the Page laser for Page Pulse Duration )

Example 2:

PRINT #1, CHR\$(10); CHR\$(18);    ( Pulse the Data laser for Write Pulse Duration )

### **Command 12: Set Port A**

Sets output pins associated with port A to a high voltage level.

Format:        12, binary mask

Binary mask is a byte, which can take on the values ( 0 – 255 ). The byte is comprised of 8 bits. Each bit in the mask, which is a one, will set the corresponding output pin to a high voltage level. Each bit in the mask, which is a zero, will leave the corresponding output pin unaffected.

Bit 7	Bit 6	Bit 5	Bit 4	Bit 3	Bit 2	Bit 1	Bit 0
Erase LEDs Off	S/H Set to Sample	Filter In	Not Used	Heater Off	Not Used	Data Laser Off	Page Laser Off

Example 1:

Turn Heater Off, Put Filter In, and Turn Erase LEDs Off, leaving all other functions unaffected.

```
REM Binary mask = 10101000 = 27 + 25 + 23 = 168
PRINT #1, CHR$(12); CHR$(168);
```

Example 2:

Turn Page Laser Off, Turn Data Laser Off, and Set S/H to Sample, leaving all other functions unaffected.

```
REM Binary mask = 01000011 = 26 + 21 + 20 = 67
PRINT #1, CHR$(12); CHR$(67);
```

#### Command 14: Clear Port A

Clears output pins associated with port A to a low voltage level.

Format:        14, binary mask

Binary mask is a byte, which can take on the values ( 0 – 255 ). The byte is comprised of 8 bits. Each bit in the mask, which is a one, will clear the corresponding output pin to a low voltage level. Each bit in the mask, which is a zero, will leave the corresponding output pin unaffected.

Bit 7	Bit 6	Bit 5	Bit 4	Bit 3	Bit 2	Bit 1	Bit 0
Erase LEDs On	S/H Set to Hold	Filter Out	Not Used	Heater On	Not Used	Data Laser On	Page Laser On

Example 1:

Turn Heater On, Put Filter Out, and Turn Erase LEDs On, leaving all other functions unaffected.

```
REM Binary mask = 10101000 =  $2^7 + 2^5 + 2^3 = 168$ 
PRINT #1, CHR$(14); CHR$(168);
```

Example 2:

Turn Page Laser On, Turn Data Laser On, and Set S/H to Hold, leaving all other functions unaffected.

```
REM Binary mask = 01000011 =  $2^6 + 2^1 + 2^0 = 67$ 
PRINT #1, CHR$(14); CHR$(67);
```

## Command 16: Set Port B

Sets output pins associated with port B to a high voltage level.

Format:        16, binary mask

Binary mask is a byte, which can take on the values ( 0 – 255 ). The byte is comprised of 8 bits. Each bit in the mask, which is a one, will set the corresponding output pin to a high voltage level. Each bit in the mask, which is a zero, will leave the corresponding output pin unaffected.

Bit 7	Bit 6	Bit 5	Bit 4	Bit 3	Bit 2	Bit 1	Bit 0
Step Motor Clock	Gain Select 10	Gain Select 4.7	Gain Select 2.2	Gain Select 1	Motor Direction Left	Motor Select 1	Motor Select 0

Motor Select:	Bit 1	Bit 0	
	0	0	- All Motors Off
	0	1	- X axis motor turned on
	1	0	- Y axis motor turned on
	1	1	- Z axis motor turned on

**Motor Heating Warning:** If a motor is left on for a long time it gets quite warm to the touch. Permanent damage has not been observed due this heating, however it is probably good practice to turn off the motors when not in use.

Motor Direction:

Setting Bit 2 of port B sets the direction to “left”. The direction affects all three motors. “Left” is the direction that moves the motors toward their limit switch. The “Home” position is when all three motors are moved “left” until they trip their limit switch.

Gain Select:

The detector has a variable gain amplifier. Only one gain select bit should be set at a time. The relative gain based on which bit is set is given in the bit map above.

Step Motor Clock:

This is a clock signal that will step the motor that is turned on in the direction selected. Driver software should not change this bit as it is controlled internally when either the Fine Step (Command 24) or the Course Step (Command 26) is issued.

Example:

Select a Gain of 4.7, Set the motor direction to left, and turn on the Y axis motor.

```
REM Binary mask = 00100110 = 25 + 22 + 21 = 38
PRINT #1, CHR$(16); CHR$(38);
```

## Command 18: Clear Port B

Clears output pins associated with port B to a low voltage level.

Format: 18, binary mask

Binary mask is a byte, which can take on the values ( 0 – 255 ). The byte is comprised of 8 bits. Each bit in the mask, which is a one, will clear the corresponding output pin to a low voltage level. Each bit in the mask, which is a zero, will leave the corresponding output pin unaffected.

Bit 7	Bit 6	Bit 5	Bit 4	Bit 3	Bit 2	Bit 1	Bit 0
Step Motor Clock	Gain Select	Gain Select	Gain Select	Gain Select	Motor Direction	Motor Select	Motor Select
	10	4.7	2.2	1	Right	1	0

See (Command 16) for a description of bit assignments.

**Gain and Motor Select Clearing;** Prior to selecting a Gain or a Motor, the bits must first be cleared using Command 18. After issuing a Command 18 to clear the bits, Command 16 can be used to select the appropriate setting.

Example: Clear the Gain and Motor Select bits.

```
REM Binary mask = 01111011 = 26 + 25 + 24 + 23 + 21 + 20 = 123
PRINT #1, CHR$(18); CHR$(123);
```

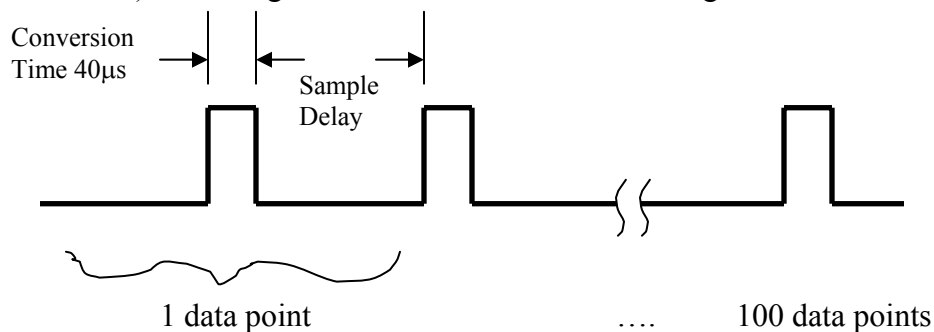
## Command 20: Analog Read

Read an analog signal from the 3D Screening Spectrometer. The signal to be read is chosen with Command 4.

Format: 20

Return: 100 data bytes

Timing: The timing is generated by, Sample Delay, contained in the internal variables list (Command 2). The diagram below summarizes the timing details.



Example: Read the Blanking Voltage

```
PRINT #1, CHR$(4); CHR$(0); CHR$(4);      ( Select Blanking Voltage )
                                           ( using Command 4 )
PRINT #1, CHR$(20);                        ( Start Analog Read )
In$ = ""                                    ( Read in 100 bytes )
DO
  AI$ = INPUT$(LOC(1), #1)
  In$ = In$ + AI$
  IF LEN(In$) >= 100 THEN EXIT DO
LOOP
FOR i = 1 TO 100                            ( Convert the bytes to numbers )
  a$ = MID$(In$, i, 1)
  a = ASC(a$)
  In(i) = a
NEXT i
sum = 0
                                           ( Average the 100 data points )
FOR i = 1 TO 100
```

```

sum = sum + In(i)
NEXT i
sum = sum / 100
voltage = 5 * sum / 255

```

( Compute Blanking Voltage )

## Command 22: Read

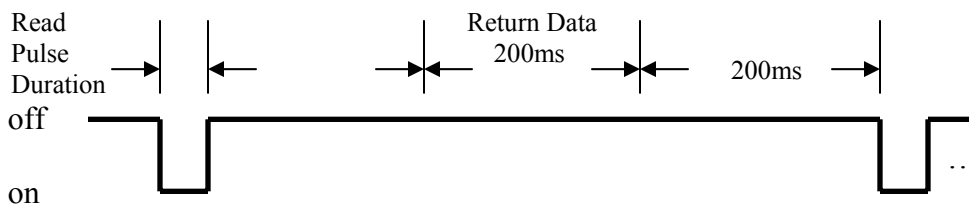
Read the O-State photocycle signal

Format:        22

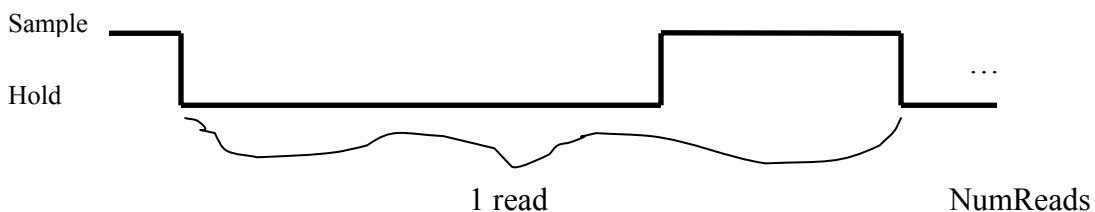
Return:        100 data bytes \* Number of Reads

Timing: The Read command performs the following sequence of events. First the Sample/Hold circuit is set to hold. After 100 $\mu$ s the Page laser is pulsed for Read Pulse Duration, followed by an Analog Read (Command 10). The Analog Read returns 100 bytes of data, which takes about 200ms. The Sample/Hold circuit is then returned to sample mode followed by another 200ms delay. This complete sequence is repeated Number of Read times. The diagram below summarizes the timing details.

### Page Laser



### Sample/Hold



**Important Note;** The Read command does **NOT** turn on the data laser beam (probe beam) and it does **NOT** position the filter in the way of the data laser beam. Also, the cuvette heater can interfere with the data and should be disabled. The host computer should perform these instructions prior to issuing a Read command.

Example: Read an O-state photocycle

```

PRINT #1, CHR$(4); CHR$(0); CHR$(0); (Set up to read the Analog signal)
PRINT #1, CHR$(12); CHR$(8);         (Disable Heater)

```

```

PRINT #1, CHR$(12); CHR$(32);          (Filter In)
PRINT #1, CHR$(14); CHR$(2);           (Turn on Data Laser)
REM A Delay can be inserted here to allow the laser light intensity to stabilize

FOR i = 1 to 100                        (Zero input variable to allow averaging)
  In(i) = 0
NEXT i
PRINT #1, CHR$(22);                    (Initiate Read)
FOR j = 1 TO NumRd                      (Repeat for Number of Reads)
  In$ = ""                              (Receive 100 bytes)
  DO
    AI$ = INPUT$(LOC(1), #1)
    In$ = In$ + AI$
    IF LEN(In$) >= 100 THEN EXIT DO
  LOOP
  FOR i = 1 TO 100                      (Add the value to the sum)
    a$ = MID$(In$, i, 1)
    a = ASC(a$)
    In(i) = In(i) + a
  NEXT i
NEXT j
FOR i = 1 to 100                        (Compute the average)
  In(i) = In(i) / NumRd
NEXT i

REM This data may now be plotted as an oscilloscope trace

PRINT #1, CHR$(12); CHR$(2);           (Turn off Data Laser)
PRINT #1, CHR$(14); CHR$(32);          (Filter Out)
PRINT #1, CHR$(14); CHR$(8);           (Enable Heater)

```

### **Command 24: Fine Step**

Steps the selected motor one step.

Format:        24

Example:

```
PRINT #1, CHR$(24);
```

### **Command 26: Course Step**

Steps the selected motor fifty fine steps.



Format:        26

Return:        M

The course step timing is handled by a handshake protocol. Upon completion of the course step command the 3D Screening Spectrometer will return an **M** (ASCII 77) to the host computer.

Example:

```
PRINT #1, CHR$(26);           ( Start Stepping )
DO                             ( Wait for M )
  AI$ = INPUT$(LOC(1), #1)
  IF AI$ = "M" THEN EXIT DO
LOOP
```

### **6.7.2. Motor Positioning issues:**

The motors cannot be accurately positioned unless they are brought to their home position prior to finding a specific location. For example, in order to move change position 525 to position 430, it must first be moved to the home location (Position 0), and then position 430 can be selected. On the other hand, movement away from the home position can be accomplished accurately without homing. For example to go from position 230 to 400, simply move the motor 170 steps away from the home position.

The home position is found by moving the motors to the “left” (see Command 16) until they hit a limit switch. The motors can move a total of 1200 steps. As a motor is moved toward home, motion stops once the limit switch is tripped. In this case the motor remains fully functional and will resume operation upon change in direction. Therefore to home a motor from an unknown location simply move 1200 steps toward home

If the motors are moved away from home for more than 1200 steps, the linkage will unscrew and motion will stop. Unfortunately, they may not properly re-thread upon motion in the other direction so care should be taken not to go past 1200 steps away from home.

## **6.8. Quick Reference Sheet for Communications Protocol to the Bacteriorhodopsin Three-Dimensional Memory**

### **Command 0: Store the Number of Writes**

Stores the number of writes to be performed when a write command is given.

Format:        0, High byte, Middle byte, Low byte

### **Command 2: Store an internal variable**

Stores a two-byte variable into the 3D Screening Spectrometer's set-up area.

Format:        2, variable #, High byte, Low byte

### **Command 4: Select Analog Signal**

Chooses which signal is sent back to the computer when an Analog (Command 20) or Read (Command 22) is issued.

Format:        4, 0, Signal

### **Command 6: Set Temperature**

Set the cuvette temperature.

Format:        6, 1, TempNum

### **Advanced Command 8: Write**

Issue a write command to the 3D Screening Spectrometer.

Format:        8, pulse1, pulse2

Return        W

### **Command 10: Pulse Laser**

Pulses the Page laser and the Data laser.

Format: 10, pulse

#### **Command 12: Set Port A**

Sets output pins associated with port A to a high voltage level.

Format: 12, binary mask

#### **Command 14: Clear Port A**

Clears output pins associated with port A to a low voltage level.

Format: 14, binary mask

#### **Command 16: Set Port B**

Sets output pins associated with port B to a high voltage level.

Format: 16, binary mask

#### **Command 18: Clear Port B**

Clears output pins associated with port B to a low voltage level.

Format: 18, binary mask

#### **Command 20: Analog Read**

Read an analog signal (Command 4) from the 3D Screening Spectrometer.

Format: 20

Return: 100 data bytes

#### **Command 22: Read**

Read the O-State photocycle signal

Format: 22

Return: 100 data bytes \* Number of Reads

**Command 24: Fine Step**

Steps the selected motor one step.

Format:        24

**Command 26: Course Step**

Steps the selected motor fifty fine steps.

Format:        26

Return:        M